| | |
|---|---|
| **Titre:** Title: | Synaptic Ion-Gated Transistors for Neuromorphic Computing Applications: Impact of Materials Properties and Ionic Media |
| **Auteur:** Author: | Ramin Karimi Azari |
| **Date:** | 2024 |
| **Type:** | Mémoire ou thèse / Dissertation or Thesis |
| **Référence:** Citation: | Karimi Azari, R. (2024). Synaptic Ion-Gated Transistors for Neuromorphic Computing Applications: Impact of Materials Properties and Ionic Media [Thèse de doctorat, Polytechnique Montréal]. PolyPublie. https://publications.polymtl.ca/61985/ |

**POLYTECHNIQUE MONTRÉAL**

affiliée à l'Université de Montréal

# Synaptic Ion-Gated Transistors for Neuromorphic Computing Applications: Impact of Materials Properties and Ionic Media

**RAMIN KARIMI AZARI**

Département de génie physique

Thèse présentée en vue de l'obtention du diplôme de *Philosophiæ Doctor*

Génie physique

Novembre 2024

**POLYTECHNIQUE MONTRÉAL**

affiliée à l'Université de Montréal

Cette thèse intitulée :

# Synaptic Ion-Gated Transistors for Neuromorphic Computing Applications: Impact of Materials Properties and Ionic Media

présentée par **Ramin KARIMI AZARI**

en vue de l'obtention du diplôme de *Philosophiæ Doctor*

a été dûment acceptée par le jury d'examen constitué de :

**Frédéric LEBLOND**, président
**Clara SANTATO**, membre et directrice de recherche
**Julian SELF**, membre
**Piero COSSEDDU**, membre externe

# DEDICATION

*To my parents, for their unconditional love, endless support, and unwavering belief in my dreams.*

*To my family and friends, who have been my pillars of strength and sources of encouragement throughout this journey.*

*To all those who have inspired and motivated me, thank you for being by my side.*

*And finally, to myself, to the quiet moments of reflection and the inner voice in the middle of the nights that whispered, "Keep going," reminding me that resilience is born from struggle and dreams take root in determination. This journey has been a testament to the spirit that guides me forward.*

# ACKNOWLEDGEMENTS

First and foremost, I would like to express my deepest gratitude to my supervisor, Professor Clara Santato, for her unwavering support, guidance, and encouragement throughout my Ph.D. journey. Her expertise, patience, and constructive feedback have been invaluable, and I am truly grateful for the opportunity to learn under her mentorship.

I would also like to extend my heartfelt thanks to my co-authors and collaborators: Wan-Yu Tsai, Liam Collins, Martin Schwellberger Barbosa, Lariel Chagas da Silva Neres, Luan Pereira Camargo, Tian Lan, José Ramón Herrera Garza, Patrick Dang, Zhaojing Gao, and Alexandre Carrière. Your contributions, insights, and dedication have been integral to the success of this work. I am especially thankful for your time and efforts in providing feedback and sharing your expertise.

To my jury members, Prof. Frédéric Leblond, Prof. Ettore Merlo, Prof. Julian Self. Thank you for taking the time to review my dissertation and for your thoughtful comments and suggestions, which have helped shape the final version of this work.

I am also deeply appreciative of the support provided by my family and friends throughout this long and challenging process. Your constant encouragement, understanding, and belief in me have given me the strength to persevere.

Finally, a special thanks to my colleagues at Polytechnique Montréal and Oak Ridge National Laboratory for fostering an inspiring and collaborative research environment.

This dissertation would not have been possible without the help and support of all those mentioned, and I will always be grateful for your contributions to this important chapter of my life.

# RÉSUMÉ

Cette thèse explore le comportement synaptique des transistors à grille ionique (IGT) en utilisant le polymère conducteur poly(3-hexylthiophène) (P3HT) et le trioxyde de tungstène ($WO_3$) comme matériaux de canal, en mettant l'accent sur le temps de réponse et le comportement synaptique pour les applications informatiques neuromorphiques. Les IGT sont essentiels pour imiter les synapses biologiques en raison de leur capacité à reproduire à la fois la plasticité synaptique à court terme (STP) et à long terme (LTP) et leur faible consommation de puissance. Les paramètres que nous avons sélectionnés pour l'étude sont le poids moléculaire et l'épaisseur de la couche mince de P3HT, ainsi que la présence d'ions de lithium ($Li^+$) dans le milieu ionique de la grille d'un IGT à base de $WO_3$: leur effet a été observé sur le temps de réponse et la fonctionnalité synaptique de transistors.

La première partie de l'étude montre comment contrôler le temps de réponse des IGT, qui est un aspect important de la modulation de la plasticité synaptique dans ces-derniers. La méthodologie conçue pour ce projet de doctorat inclut, entre autres, les effets de l'amplitude, de la durée, de la fréquence et du nombre d'impulsions appliquées au voltage $V_{gs}$ (voltage grille-source).

La deuxième partie montre que le P3HT de poids moléculaire plus élevé améliore la plasticité du dispositif et le comportement synaptique, facilitant la transition du STP au LTP. De plus, les couches plus minces de P3HT entraînent des temps de réponse plus rapides en raison de chemins de diffusion ionique plus courts, tandis que les couches plus épaisses facilitent le LTP. Les comportements synaptiques tels que la facilitation des impulsions appariées (PPF) et la plasticité dépendante du nombre de pics (SNDP) sont modulés en ajustant $V_{gs}$ et $V_{ds}$ (voltage drain-source), révélant l'influence significative de la morphologie de la couche mince de P3HT sur la dynamique des ions et la conductivité des canaux de transistors.

Dans la troisième partie, les IGT à base de $WO_3$ sont examinés, avec une emphase particulière sur l'impact de l'intercalation des ions $Li^+$. Grâce à la voltammétrie cyclique (CV) et au profilage force-distance (FD) par microscopie à force atomique (AFM), nous montrons que l'inclusion de $Li^+$ améliore la pénétration des ions, ce qui conduit à un comportement synaptique LTP amélioré. Des fonctionnalités synaptiques clés telles que la plasticité dépendante de l'amplitude des pics (SADP), la plasticité dépendante de la durée des pics (SDDP) et la plasticité dépendante de la fréquence

(FDP) sont explorées, soulignant le potentiel des IGT $WO_3$ dans les systèmes neuromorphiques qui permettent l'apprentissage adaptatif et le traitement des données en temps réel.

Dans leur ensemble, ces résultats soulignent l'importance du milieu ionique et des propriétés des matériaux dans l'optimisation des performances des transistors synaptiques, ouvrant la voie au développement de matériels neuromorphiques adaptés aux applications d'intelligence artificielle (IA).

# ABSTRACT

This dissertation explores the synaptic behavior of ion-gated transistors (IGTs) using the organic conducting polymer poly(3-hexylthiophene) (P3HT) and the tungsten trioxide ($WO_3$) as channel materials, with a focus on response time and synaptic behavior for neuromorphic computing applications. IGTs are key for mimicking biological synapses due to their ability to replicate both short-term (STP) and long-term synaptic plasticity (LTP) and low power consumption. The parameters we selected for the investigation are the molecular weight and film thickness of P3HT, as well as the presence of lithium-ion ($Li^+$) in the gating medium of $WO_3$-based IGTs: their effect was observed on response time and synaptic functionality.

The first part of the study demonstrates how to control the IGT response time, which is an important aspect of synaptic plasticity modulation in IGTs. The methodology conceived for this PhD project includes, among other factors, the effects of pulse amplitude, duration, frequency, and the number of applied $V_{gs}$ pulses.

The second part shows that higher molecular weight P3HT improves the device plasticity and synaptic behavior, facilitating the transition from STP to LTP. Additionally, thinner P3HT films result in faster response times due to shorter ion diffusion pathways, while thicker films facilitate LTP. Synaptic behaviors such as paired-pulse facilitation (PPF) and spike number-dependent plasticity (SNDP) are modulated by adjusting the $V_{gs}$ and $V_{ds}$, revealing the significant influence of P3HT film morphology on ion dynamics and channel conductivity.

In the third part, $WO_3$-based IGTs are examined, with a particular focus on the impact of $Li^+$ intercalation. Through cyclic voltammetry (CV) and atomic force microscopy (AFM) force-distance (FD) profiling, we show that the inclusion of $Li^+$ enhances ion penetration, leading to improved LTP synaptic behavior. Key synaptic functionalities such as spike amplitude-dependent plasticity (SADP), spike duration-dependent plasticity (SDDP), and frequency-dependent plasticity (FDP) are explored, emphasizing the potential of $WO_3$ IGTs in neuromorphic systems that enable adaptive learning and real-time data processing.

Together, these findings underscore the importance of both the ionic medium and material properties in optimizing the performance of synaptic transistors, paving the way for the development of neuromorphic hardware tailored for artificial intelligence (AI) applications.

# TABLE OF CONTENTS

# LIST OF TABLES

# LIST OF FIGURES

# LISTE OF SYMBOLS AND ABBREVIATIONS

| | |
|---|---|
| AFM | Atomic force microscopy |
| AFM FD | Atomic Force Microscopy Force-Distance |
| AI | Artificial intelligence |
| ANN | Artificial neural network |
| Au | Gold |
| BET | Brunauer–Emmett–Teller |
| BJT | Bipolar junction transistor |
| CMOS | Complementary MOS metal oxide semiconductor |
| CV | Cyclic Voltammetry |
| D | Drain electrode |
| d | Thickness of dielectric |
| EDL | Electric double layer |
| [EMIM][TFSI] | 1-ethyl-3-methylimidazolium bis(trifluoromethylsulfonyl)imide |
| EPSC | Excitatory postsynaptic current |
| EPSP | Excitatory postsynaptic potential |
| FDP | Frequency-dependent plasticity |
| FET | Field-effect transistor |
| G | Gate electrode |
| IGT | Ion-gated transistor |
| IL | Ionic liquid |
| IoT | Internet of Things |
| IPSC | Inhibitory postsynaptic current |
| IPSP | Inhibitory postsynaptic potential |

| | |
|---|---|
| JFET | Junction field-effect transistor |
| L | Channel length |
| LCD | Liquid-crystal display |
| LiTFSI | Lithium bis(trifluoro-methane-sulfonyl)imide |
| LTP | Long term plasticity |
| MO | Metal oxide |
| MOSFET | Metal oxide semiconductor field effect transistor |
| MW | Molecular weight |
| OECTs | Organic electrochemical transistors |
| P3HT | Poly(3-hexylthiophene) |
| PPF | Paired-pulse facilitation |
| PSP | Postsynaptic potential |
| RMS | Root mean square surface |
| S | Source electrode |
| SEM | Scanning electron microscopy |
| $SiO_2$ | Silicon dioxide |
| SNDP | Spike number dependent plasticity |
| STP | Short term plasticity |
| TFT | Thin film transistor |
| Ti | Titanium |
| $V_{ds}$ | Drain-source voltage |
| $V_{gs}$ | Gate-source voltage |
| $V_{th}$ | Threshold voltage |
| $WO_3$ | Tungsten trioxide |

| | |
|---|---|
| XRD | X-ray diffraction |
| ε | Vacuum permittivity |
| μ | Charge carrier mobility |
| τ | Response time |

# LIST OF APPENDICES

# CHAPTER 1 INTRODUCTION

## 1.1 Background

The demand for new computing systems has increased due to advancements in artificial intelligence (AI), big data analytics, and the Internet of Things (IoT), requiring greater efficiency, adaptability, and low power consumption.[1, 2] Based on the von Neumann model, conventional computing architectures face inherent power efficiency and processing speed limitations due to the physical separation of memory and processing units. This bottleneck results in significant delays and increased power consumption, which are critical concerns as we move towards more complex and autonomous systems. [3]

Neuromorphic computing provides a revolutionary solution to these challenges by emulating the architecture and functionality of the human brain. In biological systems, neurons and synapses are closely connected, enabling real-time processing and memory storage within the same network. This brain-like structure supports parallel processing, adaptive learning, and efficient power use—key features needed for future computing technologies. [4] The 2024 Nobel Prize in Physics was awarded to Hopfield and Hinton for their groundbreaking contributions to artificial neural networks, which have revolutionized machine learning and AI. [5, 6] These pioneering works are closely related to the field of neuromorphic computing, which aims to emulate the brain's architecture and functionality.

One of the most significant advancements in neuromorphic computing is the development of artificial synaptic devices. These devices emulate the synaptic connections between neurons, enabling them to store and process information simultaneously, in the same hardware. [7] Among various types of artificial synapses, ion-gated transistors (IGTs) have emerged as a promising candidate due to their ability to modulate channel conductance through ionic and electronic interactions. [8]

IGTs are three-terminal devices that control the flow of ions and electrons in the semiconducting channel. They closely mimic the behavior of biological synapses, where ions trigger neurotransmitter release to adjust synaptic strength. In an IGT, applying an electrical bias to the gate electrode in contact with an ion-gating medium, such as an ionic liquid (IL), causes a change

in charge carrier density in the semiconducting channel, leading to a change in channel conductance. This process is similar to synaptic potentiation and depression in biological systems. The strength of the synaptic connection is altered based on the frequency and duration of neuronal signals. [9]

IGTs are particularly well-suited for neuromorphic applications due to their low operating voltage, high capacitance, and ability to integrate multiple types of plasticity. By modulating the gate-source voltage ($V_{gs}$) and the drain-source voltage ($V_{ds}$), IGTs can achieve a wide range of synaptic behaviors, such as paired-pulse facilitation (PPF), spike-number-dependent plasticity (SNDP), and short and long-term potentiation (STP and LTP). These behaviors are critical for developing adaptive and efficient neural networks that can process and learn from real-time data. [10, 11]

The choice of materials for the semiconducting channel and the ionic gating medium plays a crucial role in determining the performance of IGTs. In recent years, there has been a growing interest in using organic semiconductors and metal oxides (MO) as channel materials due to their unique electronic and ionic properties. These materials allow precise control over ion intercalation and doping mechanisms, which are crucial for adjusting the response time and plasticity of IGTs. [12-15]

In this dissertation, two key materials have been explored as channel materials for IGTs: Poly(3-hexylthiophene) (P3HT) and tungsten trioxide ($WO_3$). [16-18] The materials' ionic conductivity, response time, and synaptic plasticity make them excellent candidates for neuromorphic applications. [19]

P3HT is a well-studied organic semiconductor with a charge carrier mobility of 0.1 $cm^2\ V^{-1}\ s^{-1}$ which is relatively high compared to other organic materials. It has an optical band gap of approximately 1.9 eV and the ability to undergo electrochemical doping via ion intercalation. Its flexibility in film form and ease of fabrication make it suitable for large-scale device integration, particularly in applications such as flexible electronics and bioelectronics. In the context of IGTs, P3HT channels exhibit a combination of electrostatic and electrochemical doping, which allows for the modulation of short-term and long-term synaptic plasticity. The response time of P3HT-based IGTs can be finely tuned by controlling $V_{gs}$ pulse frequency, and pulse duration, enabling the emulation of complex neural behaviors. Unique properties of P3HT such as tunable molecular

weight, flexibility in thin film form, and favorable interface with ionic liquids, make it a promising material for use in various types of transistor devices, especially those aimed at flexible and printable electronics. [20, 21]

$WO_3$, on the other hand, is a transition metal oxide with a bandgap of approximately 2.5 eV. It is widely used in electrochromic devices, sensors, and photoelectrochemical applications due to its high surface area and ion intercalation capabilities. $WO_3$-based IGTs offer a unique advantage in neuromorphic computing by enabling both two-dimensional electrostatic and three-dimensional electrochemical doping mechanisms. This dual-doping behavior, combined with the use of ILs such as [EMIM][TFSI] with/without $Li^+$, allows for precise control over synaptic plasticity and response time. The introduction of lithium ions into the $WO_3$ channel makes possible ion intercalation, leading to increased conductivity and slower response times, which are essential for long-term memory storage in neuromorphic systems. [22, 23]

## 1.2 Research Motivation

The motivation behind this research arises from the growing demand for power-efficient, adaptive, and scalable neuromorphic systems capable of emulating the dynamic functions of the human brain. Neuromorphic computing holds great promise for addressing challenges related to power consumption, real-time data processing, and learning. However, the successful realization of such systems depends on the development of artificial synaptic devices that can mimic the intricate behaviors of biological synapses.

Organic materials like P3HT and metal oxides like $WO_3$ are promising for synaptic transistors, with potential applications in wearable electronics, sensors, and neuromorphic computers. Ion gating, which employs ionic liquids (ILs), ion gels, or saline solutions, enables low-voltage operation due to the high capacitance of the electrical double layer (EDL) at the interface between the semiconductor and the ion-gating medium. However, understanding the modulation of response times and synaptic behavior in these devices through their materials science and electrical properties remains a complex challenge.

This dissertation focuses on addressing these challenges by exploring the synaptic behavior of IGTs based on P3HT and $WO_3$ channels. By studying the working mechanism of the transistors,

considering the morphology of the channel semiconducting materials and the physicochemical properties of different ion gating media, such as [EMIM][TFSI] with/without $Li^+$, on the response time and plasticity of these devices, this work aims to contribute to the development of neuromorphic systems that can perform real-time processing and learning, while maintaining low power consumption

## 1.3 Objectives

The primary objective of this research is to explore, optimize, and *develop new interdisciplinary knowledge* in IGTs based on advanced materials for neuromorphic computing applications. To accomplish the main objectives, the following specific objectives have been fulfilled:

1- Fabrication of organic and MO IGTs using P3HT and $WO_3$ channel films and exploration of the doping mechanism.

a) We fabricated P3HT and WO3-based IGTs and characterized their morphological, structural, and electrical properties, revealing that ion gating allows for lower potential operation through the formation of EDLs and/or electrochemical doping at the semiconductor/ion-gating media interface. Electrical characterizations demonstrated that transistor performance is influenced by the morphology of the channel semiconducting films, as well as the nature of the mobile ions in the gating media, both of which impact the transistors' working mechanism.

b) By employing ILs with different ions, we can clarify the role of ILs in doping p-type P3HT and n-type $WO_3$ films. The molecular structure, size, and polarizability of the ions are expected to significantly influence the doping process.

2. Investigate the factors affecting response time and synaptic behavior of IGTs

a- Exploring the effect of input stimulus on response time and synaptic behavior of IGTs

The first article investigates the response time and synaptic behavior of IGTs, focusing on how input pulses’ amplitude, frequency, and duration influence IGT response time and synaptic plasticity. This study provides insights into the tuning of response times for both short-term and long-term plasticity in IGTs. Different doping mechanisms in IGTs affect their use as neuromorphic devices. The permeability of the semiconducting channel to ions determines whether

IGTs experience volumetric (three-dimensional) or electrostatic (field-effect, two-dimensional) doping, resulting in a wide range of response times. The correlation between applied bias, transistor response time and synaptic behavior, and the advancement of the degree of doping in a synaptic transistor are like biological action spikes in neurons and can feature the processing rate of the human brain, for artificial intelligence and neuromorphic computing applications.

b- Demonstrate the potential of IGTs in neuromorphic systems by fine-tuning the synaptic plasticity and response time using different channel materials and gating media, highlighting the importance of materials' selection in developing efficient artificial synapses.

We started this study by exploring the effect of different P3HT molecular weights (MW, low (24 kDa), intermediate (42 kDa), and high (92 kDa)) as a channel material of IGT on morphology, transistor device characteristics, response time, and synaptic behavior. Low MW P3HT films, exhibiting a higher degree of order, are expected to have lower ion permeability compared to intermediate and high MW P3HT films. Moreover, the MW of P3HT has an impact on the structure and the charge carrier transport properties of the thin films.

We continued the study using $WO_3$ metal oxide IGT channel material and investigated the morphological properties of this channel material and its effect on the response time and synaptic behavior of IGT. We examined the role of ion intercalation and doping mechanisms in modulating synaptic behavior. By introducing $Li^+$ ions into [EMIM][TFSI] as the gating medium, this work demonstrates how ion size and io mobility affect the transition from short-term to long-term plasticity, a critical feature for neuromorphic applications. Electrochemical processes at the ionic liquid/channel material interface were investigated by using different sizes of ions and their effect on response time and synaptic behavior of IGTs investigated. The study highlights the importance of ion-gating medium selection in optimizing synaptic plasticity and response time for neuromorphic systems.

Research on the relationship between channel and gating medium material is expected to improve our understanding of how ion-gating affects the performance of a synaptic device and reveal how different materials affect the response time and synaptic behavior of IGTs.

c- Provide insights into the role of device architecture in contributing to the design of synaptic devices.

The investigation into the dependence of response time and synaptic behavior on channel film thickness in P3HT-based IGTs indicated that films deposited at lower spin coating speeds, resulting in thicker films, significantly increased the response time of the IGTs. Additionally, greater film thickness led to an improvement in synaptic behavior, facilitating the transition from short-term plasticity (STP) to long-term plasticity (LTP).

3. Development of new interdisciplinary knowledge by integrating synaptic IGTs with materials science for neuromorphic applications

Investigate the intersection of materials science and neuromorphic computing by evaluating how the rational use of materials like P3HT, $WO_3$ and ILs enhances the performance of synaptic devices. Here, we emphasize the development of a deeper understanding of the relationship between material properties (such as ion intercalation, doping mechanisms, electric double layer structure, and surface morphology) and the performance of neuromorphic devices through ex-situ, in situ and in operando tests.

a- Ex situ material characterization for understanding synaptic behavior in IGTs

The integration of synaptic ion-gated transistors (IGTs) with materials science for neuromorphic applications was realized by employing several key ex situ characterization techniques -namely X-ray Diffraction (XRD), Atomic Force Microscopy (AFM), and Scanning Electron Microscopy (SEM)- to analyze the structural and morphological properties of the materials used in IGTs. XRD was used to identify the crystallographic structure and phase purity of the P3HT and $WO_3$ employed in the IGTs channel, providing critical insights into how the crystallographic phases influence ionic conductivity and synaptic behavior. AFM enabled us to study the surface roughness and topography of the thin films, revealing how surface morphology impacts ion intercalation and, consequently, the response time and synaptic plasticity. SEM provided detailed imaging of the microstructure, offering a view into the particles' size and distribution, which affect the conductivity and overall synaptic performance of the device. Brunauer–Emmett–Teller (BET)

analysis was used to measure the porosity and surface area of materials, critical for understanding how much surface is available for reactions or interactions, such as ion intercalation in IGTs.

These ex-situ techniques allowed us to directly link material properties to synaptic behaviors observed in IGTs. For instance, the particles' structure and crystallinity identified through SEM and XRD were correlated with the performance of synaptic functions, such as STP and LTP. BET analysis was conducted to measure the surface area and porosity of the films, providing a quantitative assessment of how accessible the surface is to ions during gating. A higher surface area generally allows for more efficient ion intercalation, which directly impacts the device's ability to emulate synaptic functions.

b- Employing in operando advanced characterization techniques for synaptic IGTs

To further understand the dynamic relationship between materials' properties and synaptic behaviors in IGTs, we employed cyclic voltammetry (CV) and in operando techniques such as Atomic Force Microscopy Force-Distance (AFM FD) profiling. AFM FD profiling was used to analyze the EDL structure at the interface between the IL and the semiconducting channel during IGT operation. This real-time observation allowed us to track the arrangement and movement of ions in the channel, providing critical insights into how surface morphology and materials' structure influence ion intercalation, which is directly tied to the synaptic plasticity of the device.

CV was instrumental in revealing the redox behavior and electrochemical doping mechanisms of the $WO_3$ and P3HT films with different morphologies. By applying different voltage sweeps, we were able to study the current response of the material in real time, helping us understand how the materials' ion storage capacity and charge transfer efficiency impact synaptic behaviors like STP and LTP.

These tests allowed us to observe the active interplay between material properties -such as surface area, ion mobility, and crystallinity- and the synaptic behavior of the IGTs. By integrating these characterization techniques, we established how key material factors influence neuromorphic performance, further justifying the importance of materials science in optimizing synaptic devices for neuromorphic computing.

## 1.4 Organization of the study

This PhD thesis contains 8 chapters. Chapter 1 is the introduction and discusses the background, motivation, and objectives of this PhD work. Chapter 2 is dedicated to the literature review on neuromorphic computing, a brief history of transistors, including field-effect transistors, their working principles and characteristics, as well as ion-gated transistors, detailing their materials, structures, working principles, time-resolved characteristics, and synaptic behaviors. Chapter 3 discusses the methodology used in this PhD thesis. Chapters 4, 5, and 6 are about the three articles where I am the first author.

Article 1: Ramin Karimi Azari, Tian Lan, and Clara Santato. "On the factors affecting the response time of synaptic ion-gated transistors." Journal of Materials Chemistry C 11.24 (2023): 8293-8299.
Article 2: Ramin Karimi Azari, Zhaojing Gao, Alexandre Carrière, and Clara Santato. "Exploring response time and synaptic plasticity in P3HT ion-gated transistors for neuromorphic computing: impact of P3HT MW and film thickness." RSC Applied Interfaces 1, no. 3 (2024): 564-572.

Article 3: Ramin Karimi Azari, Luan Pereira Camargo, José Ramón Herrera Garza, Liam F Collins, Wan-Yu Tsai, Lariel Chagas da Silva Neres, Patrick Dang, Martin Schwellberger Barbosa, Clara Santato, "Emulation of Synaptic Plasticity in a $WO_3$-Based Ion-Gated Synaptic Transistor for Neuromorphic Computing", 2024 (Manuscript ID: aisy.202400883, currently under review in the journal *Advanced Intelligent Systems*). Chapter 7 is a general discussion of all the work that I did during my PhD. Chapter 8 discusses the conclusions from all the work and perspectives for future work.

.

# CHAPTER 2 LITERATURE REVIEW

## 2.1 Overview of neuromorphic computing and its significance

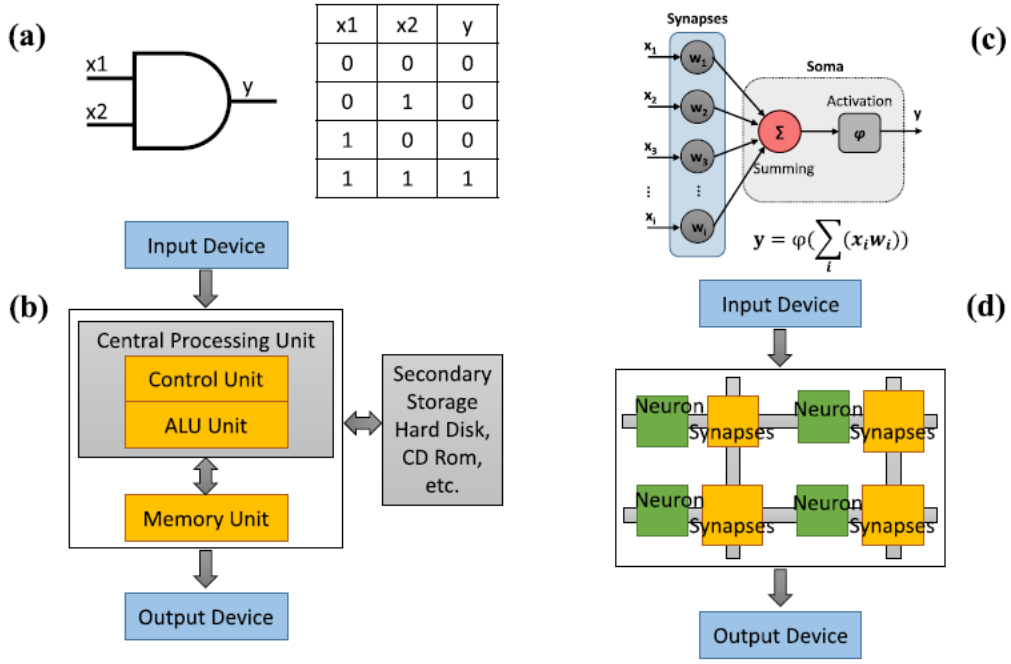


Figure 2.1 a) Truth Table of Boolean AND Gate, b) Von Neumann architecture algorithm, c) Schematic of the artificial neuron operation, d) The neuromorphic computing architecture. [24]

Most modern computers are based on Alan Turing's concept of universal computation through serial instructions. This design, known as the von Neumann architecture, separates information storage from information processing at a macro level (Figure 2.1a and b). However, these systems, which depend on transistors operating in a saturation regime with deterministic behavior, are power-intensive, primarily execute tasks serially, function in a coordinated manner, are susceptible to physical damage, and require explicit programming for each specific task. [25]

In contrast, biological systems operate through nondeterministic processes, utilizing the large-scale parallelism of simple processing units, neurons, as illustrated in Figure 2.1c and d. Unlike the static von Neumann architecture, which is grounded in Boolean logic, neuromorphic systems are built

on neurons and their dynamically evolving synapses. The term "neuromorphic" was first introduced by Mead in 1990. [26]

Neuromorphic systems are engineered to replicate the neuron-synapse interactions found in human neural networks, to optimize performance in deep learning and artificial intelligence (AI) systems that fed by big data. [27, 28] To achieve this, these systems emphasize critical features of biological neural networks, such as large-scale parallel processing and extremely low power consumption. In recent decades, significant research has been dedicated to developing artificial neural network (ANN) algorithms, which simulate biological neural networks by mathematical *perceptron*. [29]

Neuromorphic systems achieve powerful and efficient neural computations through the hardware implementation of ANNs. [30] The fundamental idea of hardware-based neural networks utilizing synaptic devices is illustrated in Figure 2.1c. This approach enables the two primary phases of the ANN algorithm to be executed through read and adjust processes. The ANN model is built around three key components: an input vector (x), a weight matrix (w), and an output vector f(w·x). [31]

Incorporating synaptic devices into large-scale neuromorphic systems requires addressing several key performance metrics that correspond to industrial standards. [32] These include: (1) non-volatile memory, crucial for reliably storing weight values and sustaining network functionality; (2) high integration density, which allows for the accommodation of extensive neural networks within a confined space; (3) high operating speed, essential for rapid inference (read) and training (write) processes in hardware-based ANNs; and (4) low power consumption, which is necessary for energy-efficient neural network operations, covering both inference and training phases. [33]

Neuromorphic computing replicates the architecture of the brain, which is an efficient, massively parallel information-processing system. The mammalian brain contains approximately $10^{11}$ neurons, forming around $10^{15}$ synaptic connections, integrating both processing and memory. This unique structure enables the brain to perform complex tasks in a highly distributed manner, using only about 20 watts of power. [34, 35] The brain of a fruit fly, another example, with its ability to perform real-time tasks such as flight control and path planning, consumes only microwatts of power, demonstrating the extraordinary energy efficiency of biological systems. [36, 37] In contrast, conventional supercomputers consume megawatts of power and require extended time to execute complex calculations. [38, 39]

To implement neuromorphic functionalities in hardware, devices have been developed that can be broadly classified into two types: conductance-based and capacitance-based, both capable of mimicking synaptic behaviors. Conductance-based devices, such as memristors, are two-terminal systems that adjust their resistance based on the applied voltage history. Memristors are highly compact, power-efficient, and ideal for high-density memory arrays, though they often lack precise control over switching dynamics due to limited input variables. In contrast, three-terminal devices like synaptic transistors feature an additional gate terminal that allows fine modulation of channel conductivity. This extra terminal provides greater control and flexibility, enabling more complex and tunable synaptic functions, making them suitable for more sophisticated neuromorphic applications. [40] These devices are designed to emulate the behavior of biological synapses through gradual conductance changes. [41, 42]

Synaptic array architectures, composed of synaptic device cells, can differ depending on the operational mechanism and structural design of the devices. Neuromorphic systems are often impacted by the intrinsic non-ideal properties of synaptic devices. These devices may show limitations related to materials and fabrication processes, leading to issues such as non-linear and asymmetric conductance modulation, limited on/off ratios, low precision in device states, poor reliability, and variations between devices or across different cycles. Such challenges complicate the realization of reliable and accurate analog computing operations, in comparison to the accuracy typically achieved in conventional digital computing systems. [43, 44]

To address this issue, along with other challenges such as developing scalable, energy-efficient devices that can be integrated into larger neuromorphic architectures, various studies have been undertaken to explore solutions for mitigating hardware non-idealities to mimic key neural behaviors like learning, memory retention, and adaptive responses to stimuli.

## 2.2 Introduction to synaptic transistors and their role in neuromorphic systems

Synaptic transistors, often realized as ion-gated transistors (IGTs), are an essential component in neuromorphic systems due to their ability to mimic synaptic plasticity at the hardware level. These transistors modulate ion flow to adjust conductance, like how synaptic connections in the brain are

strengthened or weakened through neural activity. To understand this part, we need to learn more about the transistors.

### 2.2.1 History of transistors

The history of transistors traces back to the late 1940s, [45] with the invention of the transistor that laid the foundation for modern electronics. In 1947, John Bardeen, William Shockley, and Walter Brattain at Bell Laboratories successfully developed the first transistor. [46] This groundbreaking achievement, recognized with a Nobel Prize in Physics in 1956, spurred a flurry of innovations aimed at improving the efficiency of transistors and miniaturizing them. [47] Early progress saw the introduction of bipolar junction transistors (BJTs), which were later refined into more efficient silicon-based transistors, further advancing electronic technologies.

A pivotal moment in transistor history occurred in 1947 when Bardeen and Brattain developed the point-contact transistor at Bell Labs, followed shortly by Shockley's invention of the bipolar junction transistor (BJT). Although Julius Lilienfeld first theorized the junction field-effect transistor (JFET) in the 1920s, it was not successfully built until the 1950s, with contributions from engineers such as Nishizawa and Watanabe. Shockley's efforts to commercialize transistor technology played a crucial role in establishing California's Silicon Valley as a global hub for electronics innovation. The JFET, offering higher input impedance and lower noise compared to the BJT, became a practical and versatile device that laid the foundation for future advancements in transistor technology. [48]

In 1959, a significant advancement occurred when Mohamed Atalla and Dawon Kahng at Bell Labs invented the metal-oxide-semiconductor field-effect transistor (MOSFET). This innovation marked a major turning point in electronics, as MOSFETs quickly became the dominant transistor type used in digital circuits. [49] One of the breakthroughs was the development of two complementary configurations: n-channel and p-channel MOSFETs. When used together in circuits, they formed complementary MOS (CMOS) technology, which became the basis for nearly all modern electronic devices, from memory chips to microprocessors and CPUs. The versatile CMOS architecture has enabled the mass production of integrated circuits that power everything from computers and smartphones to cameras. [50]

The drive for miniaturization and mass production of transistors led to the development of thin-film transistors (TFTs), which became critical for the production of liquid-crystal displays (LCDs). These advancements in transistor technology revolutionized the electronics industry, allowing the creation of smaller, faster, and more energy-efficient devices, such as laptops, mobile phones, and televisions. In recent decades, transistor development has exploded in new directions, moving beyond traditional rigid designs to more advanced, lightweight, flexible, and stretchable electronics. This evolution is paving the way for the next generation of wearable technology, textile-integrated systems, flexible and rollable displays, and even biocompatible electronics, including medical implants and artificial skin. MOSFET-based technologies remain at the forefront of these innovations, shaping the future of electronics and enabling increasingly sophisticated applications in healthcare, computing, and communication. [51]

From the early transistor pioneers to today's cutting-edge developments in flexible electronics, transistors have undergone a remarkable transformation, becoming the backbone of modern technology. Each stage of their evolution has unlocked new possibilities for designing more complex, efficient, and versatile electronic systems, pushing the boundaries of what is possible in science and technology.

### 2.2.2 Thin film transistors (TFTs)

TFTs were developed based on the work on MOSFETs by Paul K. Weimer at RCA in 1962. The terminals in the TFTs are on a significantly thin conducting layer of semiconductor (channel). A dielectric layer is in between the gate electrode and the semiconductor channel. The potential applied between the drain and source ($V_{ds}$) induces the drain-source current ($I_{ds}$).

The flow of electrons (or holes) from the source to drain is controlled by affecting the size and shape of a "conductive channel" created and influenced by voltage (or absence of voltage) applied across the gate and source (grounded) terminals, $V_{gs}$. [52, 53]

### 2.2.3 Field-effect transistor (FETs)

FETs are fundamental components of modern electronics, utilized for their ability to amplify or switch electronic signals. They operate based on the electric field effect, where an applied voltage at the gate terminal modulates the conductivity of a semiconductor channel between the source and

drain terminals. FETs can be broadly categorized into two main types: MOSFETs and TFTs, both of which share fundamental operating principles with distinct structural variations. [54]

FETs is also known as a unipolar transistor since it only uses the majority carriers in the semiconductor to conduct electricity. [55]

A FET and a TFT share the same basic structure (Figure 2.2). In both, thin films of an active semiconductor, a dielectric layer, and metallic contacts are applied to a non-conductive substrate. [56]

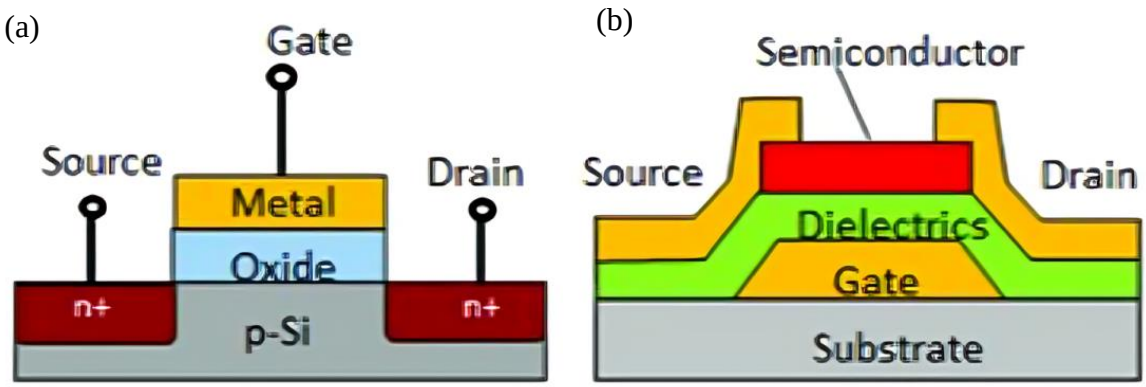


Figure 2.2 Schematic cross-sections of a) n-type MOSFET, b) TFT structures. [57]

These three terminals can be described as follows:

Source (S), through which the carriers enter the channel. The current entering the channel at S is indicated by $I_S$. Drain (D), through which the carriers leave the channel. $I_d$ is the current entering the channel at D. Gate (G), the terminal that modulates the channel conductivity by applying a voltage to the gate. The gate is placed in very close proximity to the channel so that its electric charge is able to affect the channel. [58] The channel can be made of various semiconductor materials such as silicon, metal oxides, or organic semiconductors. The source and drain geometry in terms of width (W, transistor's extension in the perpendicular direction to the cross-section) and length (L, distance between source and drain) is required to define a channel (Figure 2.2). Typically, the width of the channel is much larger than the width of the gate.

The gate in a FET regulates the current of charge carriers (electrons or holes) between the source and drain by adjusting the width of the conductive channel. The semiconductor channel can either be p-type or n-type, leading to the classification of FETs into two types: p-channel and n-channel (Figure 2.2). [57]

Additionally, FETs can be classified into two more categories based on how the gate voltage affects the charge carriers in the channel. Increasing the gate voltage can either reduce (deplete) or increase (enhance) the number of available carriers, resulting in two types: depletion-mode FETs and enhancement-mode FETs.

### 2.2.4 Basic Structure and Function of FETs

In FETs, the insulator layer is typically composed of silicon dioxide ($SiO_2$), which separates the gate from the semiconductor (commonly silicon). The applied gate voltage modifies the electric field across the dielectric, altering the concentration of charge carriers in the channel and enabling or preventing current flow between the source and drain.

In MOSFETs, channel formation occurs through inversion, where a positive gate voltage depletes the p-type substrate of holes and eventually attracts electrons to form an inversion layer. In contrast, TFTs form the channel through direct operation method, where the gate voltage directly attracts charge carriers to the interface without requiring depletion or inversion.

FETs operate in either enhancement or depletion modes, based on their threshold voltage ($V_{th}$) and the applied $V_{gs}$. In enhancement mode, the transistor is normally “off” when $V_{gs}$ is zero because there is no conductive channel present. A positive $V_{gs}$ (for an n-channel device) or negative $V_{gs}$ (for a p-channel device) must be applied to induce charge carriers at the semiconductor-dielectric interface, forming a conductive channel and turning the transistor on. In depletion mode, the transistor is normally “on” when $V_{gs}$ is zero, as a conductive channel already exists. Applying the appropriate $V_{gs}$ reduces the carrier density in the channel, thereby turning the transistor off or reducing its conductivity. The difference between n-type and p-type devices in FETs is attributed to the type of charge carriers responsible for channel current. The charge carriers in n-type FET (n-channel FET) are electrons. When a positive $V_{gs}$ is applied to the transistor, electrons are attracted to the channel which allows the current to flow between the source and the drain ($I_{ds}$). The

conductivity of the channel and $I_{ds}$ increases as more electrons accumulate. Typically, n-type FETs are faster and more efficient than p-type devices due to the higher mobility of electrons compared to holes.

In p-type FETs (p-channel FET) the charge carriers are holes. To induce $I_{ds}$ current flow, a negative $V_{gs}$ is applied, attracting holes into the channel. P-type transistors typically have lower carrier mobility than n-type transistors, meaning they operate at slower speeds, but they are still essential in complementary circuits (such as CMOS) to provide optimal performance.

## 2.3 Metrics of FETs

### 2.3.1 Modes of Operation

FETs typically operate in three distinct regions:

**Cut-off region**: In this region, $V_{gs}$ is less than $V_{th}$, and no conducting channel is formed between the source and drain. As a result, only a minimal current flows through the transistor.

**Linear or Ohmic Region**: When $V_{gs} > V_{th}$ and the $V_{ds}$ is relatively small ($V_{ds} < V_{gs} - V_{th}$), a conducting channel forms, and current flows between the source and drain. The current increases linearly with the applied $V_{ds}$, like a resistor. When this condition is not satisfied, the transistor may enter a non-linear region where it does not exhibit purely linear behavior and has not yet reached the saturation regime, resulting in a transitional operating state.

**Saturation region**: As the $V_{ds}$ increase further, the channel near the drain becomes pinched off, limiting the current despite further increases in $V_{ds}$. In this regime, the transistor behaves like a constant current source.

The current flowing through the transistor in the linear and saturation regions can be described by the following equations:

Linear region:

$$I_{ds} = C_0 \mu_n \frac{W}{L} \left[ \left( V_{gs} - V_{th} \right) - \frac{V_{ds}}{2} \right] V_{ds} \tag{2.1}$$

Where $C_0$ is the dielectric specific capacitance or capacitance per unit area, $\mu_n$ is the charge carrier mobility, $V_{th}$ is threshold voltage, W and L is the channel width and length.

Saturation region:

$$I_{ds} = \mu_n C_0 \frac{W}{2L}\left(V_{gs} - V_{th}\right)^2 \tag{2.2}$$

### 2.3.2 The transfer characteristics

The transfer curve describes the relationship between $I_{ds}$ and $V_{gs}$, while $V_{ds}$ stays constant. The transfer characteristics of a FET provide critical insight into its switching behavior and current modulation as a function of $V_{gs}$.

These characteristics are divided into different operating regions based on the value of $V_{gs}$. When $V_{gs} < V_{th}$, the FET operates in the cut-off region. In this region, the channel does not form, and as a result, the $I_{ds}$ is extremely small, often considered negligible, meaning the transistor is effectively off.

When $V_{gs} > V_{th}$, the FET enters the linear (ohmic) or saturation region depending on $V_{ds}$. In this case, the $V_{gs}$ is sufficient to invert the channel. As $V_{gs}$ increases, $I_{ds}$ increases.

### 2.3.3 Charge Carrier Mobility, Transconductance, ON/OFF ratio

The performance of a FET is highly dependent on the mobility of the charge carriers within the channel. Mobility represents the velocity at which charge carriers move under an applied electric field. In the linear region, the mobility can be expressed as:

$$\mu_{lin} = \frac{L}{WC_0V_{ds}} \frac{dI_{ds}}{dV_{gs}} \tag{2.3}$$

In the saturation region, it is given by:

$$\mu_{sat} = \frac{2L}{WC_0} \left(\frac{d\sqrt{I_{ds,sat}}}{dV_{gs}}\right)^2 \tag{2.4}$$

Another key parameter, the transconductance ($g_m$), is the rate at which the $I_{ds}$ with respect to the $V_{gs}$, highlighting the sensitivity of the current flowing through the transistor's channel to variations in the input voltage, reflecting the device’s amplification capability. It is defined as:

$$gm = \left.\frac{\partial y}{\partial x}\right|_{V_{ds}=const} \tag{2.5}$$

In the linear regime, $g_m$ is given by:

$$g_m = \mu_n C_0 \frac{W}{L} V_{ds} \tag{2.6}$$

While in the saturation regime, it is expressed as:

$$g_m = C_0 \mu_n \frac{W}{L} \left(V_{gs} - V_{th}\right) \tag{2.7}$$

In a MOSFET, the saturation current ($I_{dsat}$), which is the current when the transistor is in its fully conducting state (on-state), is referred to as $I_{on}$. On the other hand, the off current, which occurs when the MOSFET is below $V_{th}$ (off-state), is called $I_{off}$. The ratio between these two currents, $I_{on}$ / $I_{off}$, defines the ON/OFF ratio of the transistor.

A high ON/OFF ratio is a key indicator of good switching properties, making MOSFET suitable for digital circuit applications. A higher $I_{on}$ ensures strong current conduction during the on-state, while a lower $I_{off}$ minimizes unwanted current during the off-state, reducing power dissipation.

In practical devices, minimizing $I_{off}$ is essential to ensure low leakage currents. A low off-state current reduces unnecessary power consumption when the device is idle, resulting in low standby power requirements. This feature is particularly important in modern electronics, where energy efficiency and power savings are crucial.

## 2.4 Ion-Gated Transistors

Due to low gate dielectric specific capacitance (5-10 nF $cm^{-2}$,), traditional TFTs need a high operating voltage (up to tens of volts for 100-200 nm $SiO_2$ thickness).

Employing a high permittivity dielectric material or reducing the gate dielectric thickness are common and effective methods to lower the operating voltage in TFTs to integrate them in wearable, printable, and low-power consumption electronics. However, disadvantages, including decreased charge carrier mobility or high leakage current, occur with the former or latter choice. [59] In addition to traditional FETs, ion-gated transistors (IGTs) have emerged as an alternative, particularly for applications requiring low-voltage operation.

Ion-gated transistor (IGT) contains an ionic medium as a gating material. In IGTs ionic medium is used as the gate dielectric, which forms an EDL at the semiconductor/gating medium interface. Ion-gating is an alternative to conventional dielectrics for obtaining high capacitance (1-10 $\mu F/cm^2$), because of formation of a thin EDL (a few nanometer-thick) and facilitates novel applications to a broad range of neuromorphic computing, sensors, and bioelectronic devices. An ionic medium contains at least one species of mobile ions. A simple example of an ionic medium is an electrolyte that is a solution of salt in water. Ion-gated transistors can have large charge carrier densities ($\sim 10^{15}$ $cm^{-2}$) in the channel due to their high capacitance, which can be achieved at low voltages (as low as 2 V).

The ability to store information is another application of IGTs that is a prerequisite for many applications in organic electronic devices. The physical property of IGTs to undergo hysteresis in response to an applied electric field is the way to store information. Non-volatile and rewritable memory devices are the goals of this technology, providing reliable memory performance suitable for a wide range of synaptic applications. These novel memories are commonly known as "memristors". Compared with two-terminal memristive devices such as RRAM and PCM, three-terminal IGTs provide decoupled write/read operations due to their reverse ion characteristics. [60-62]

### 2.4.1 Doping Mechanism in IGTs

The doping mechanism in IGTs is distinct from traditional FETs due to the use of an ionic gating media instead of a conventional dielectric. This doping process utilizes the formation of an EDL at the gating media/semiconductor interface, which allows for efficient control of charge carrier density at low voltages, enabling IGTs to be suitable for low power applications. The EDL acts as a highly capacitive layer, modulating the density of charge carriers in the semiconductor channel through the movement of ions in the electrolyte.

Electrostatic and electrochemical doping are two types of doping mechanisms in IGTs (Figure 2.3a).

**Electrostatic vs. Electrochemical Doping**

In IGTs, the doping mechanism can occur through two main processes: electrostatic doping and electrochemical doping. The difference between these two processes depends on the permeability of the semiconductor channel and how ions interact with it.

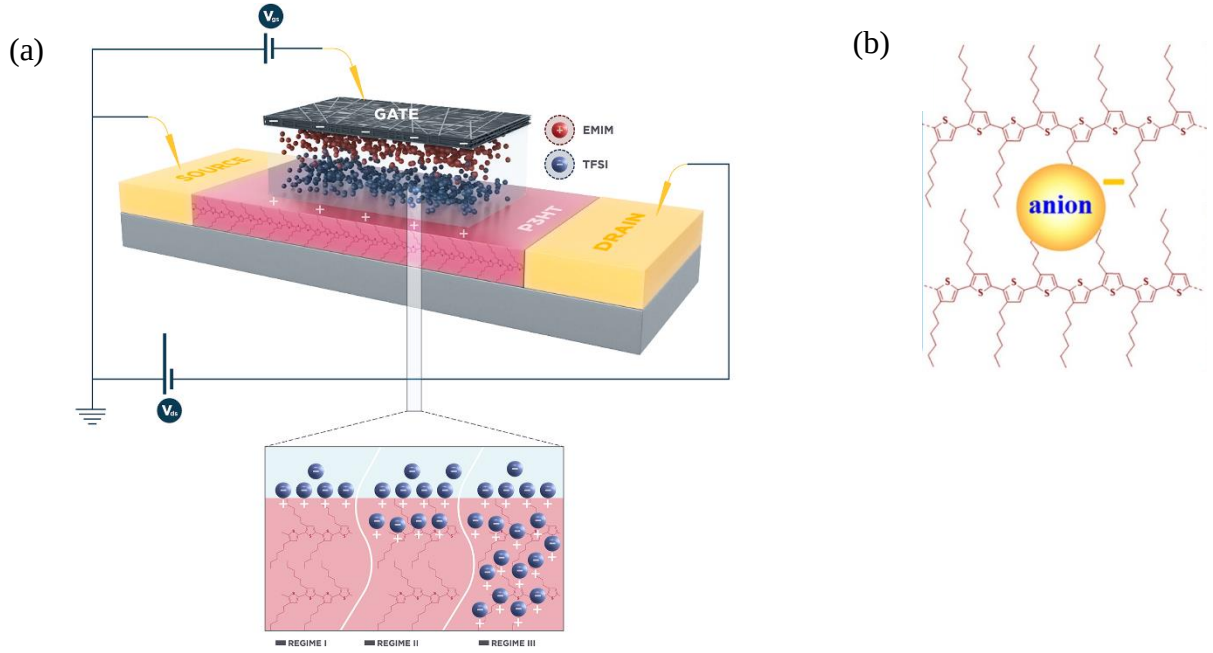


Figure 2.3 a) Different types of doping mechanisms in IGTs, b) Chemical structures of P3HT polymer [63]

**Electrostatic doping**: This occurs when the semiconductor material is impermeable to ions from the gating media. When a $V_{gs}$ is applied, ions in the ionic media accumulate at the gating medium/semiconductor interface, forming an EDL. This layer induces mobile charge carriers (either electrons in n-type or holes in p-type semiconductors) in the channel without the ions penetrating the semiconductor. As seen in the first regime of Figure 2.3a, this mechanism is purely electrostatic, similar to conventional FETs, and results in carrier accumulation or depletion without any chemical change in the channel material.

**Electrochemical doping**: If the semiconductor is ion-permeable, ions can penetrate the semiconductor under the influence of the applied $V_{gs}$ (second and third regimes of Figure 2.3a). This leads to an actual chemical modification of the transistor channel. In this case, the doping

process becomes electrochemical. Electrochemical doping plays a significant role in modulating the conductivity of channel semiconductors and enables longer-term effects in the IGT channel.

Doping in IGTs is not purely electrostatic or purely electrochemical. Instead, both mechanisms often coexist, with each contributing to varying degrees depending on factors such as the applied $V_{gs}$, the permeability of the semiconductor, and the gating media.

## 2.5 Materials and Structures for Ion-Gated Synaptic Transistors

### 2.5.1 Channel materials used in the fabrication of IGTs

The choice of channel material plays a critical role in determining the performance of IGTs. These materials not only influence the electrical properties, such as charge carrier mobility and threshold voltage, but also determine the device's compatibility with various applications, such as bioelectronics, neuromorphic computing, and flexible electronics.

**Organic Semiconductors**

Organic semiconductors are widely used as channel materials in IGTs due to their compatibility with flexible substrates, solution processing, and potential for low-cost, large-area fabrication.

Some of the most studied organic semiconductors include pentacene, poly(3-hexylthiophene) (P3HT), and poly[2-methoxy-5-(2-ethylhexyloxy)-1,4-phenylenevinylene] (MEH-PPV). These materials are known for their ability to undergo electrostatic doping when interfaced with ionic gating media, providing efficient modulation of charge carrier density at low operating voltages. For instance, P3HT has been extensively used in IGTs for its semiconducting properties and ability to form a high-capacitance EDL at the interface with ionic liquids.

Organic semiconductors used in IGTs are primarily divided into two categories: conjugated small molecules, such as PCBM, and conjugated polymers, such as PCDTBT and P3HT).

The semiconducting behavior of conjugated molecules and polymers arises from the unique electronic structure of their carbon-based backbone, characterized by sp2 hybridization. This structure forms a series of alternating single and double bonds, creating π-bonding and antibonding states that generate the highest occupied molecular orbital (HOMO) and the lowest unoccupied molecular orbital (LUMO). The energy gap between the HOMO and LUMO is known as the band

gap ($E_g$). Short-conjugated chains, like ethylene, possess a wide band gap (~7.6 eV), which makes them insulators. However, as the length of the conjugated polymer increases, the density of π and π* states grow, narrowing the band gap to a semiconductor range (typically below 4 eV).

At the very long conjugated polymer chains, a small energy gap (band gap) remains, which is due to a phenomenon called the Peierls distortion. This distortion occurs when carbon atoms in the polymer chain form pairs (dimerize), causing the system to become more stable. As a result of this pairing, the energy of HOMO decreases, and the energy of LUMO increases, maintaining a small energy gap that preserves the semiconducting properties of the polymer. For effective charge transport and conductivity, these polymers need to be doped to generate mobile charge carriers. This can be done through either p-type (oxidation) or n-type (reduction) doping. In p-type doping, the polymer loses electrons (oxidation), while in n-type doping, it gains electrons (reduction). Both processes result in the formation of charge carriers such as polarons—which are quasiparticles consisting of a charge and its associated lattice distortion—or bipolarons, which involve two charges coupled with lattice deformation. These charge carriers facilitate electrical conductivity through the polymer.

In terms of electronic transport, conjugated polymers exhibit complex mechanisms due to their inherent disorder and soft material characteristics. Transport within these materials is often hindered by structural defects and the need for charge hopping across localized states. In semicrystalline polymers, charge mobility is enhanced by extended conjugation lengths and stronger intermolecular coupling within ordered regions, whereas in amorphous regions, higher activation energies are needed to enable charge transport.

In this thesis, we used the organic polymer, polymer poly (3-hexylthiophene) (P3HT) with different MWs. Figure 2.3b shows the chemical structure of this organic semiconductor.

Table 2.1 Four well-studied organic channel materials

| | **P3HT [64, 65]** | **PEDOT:PSS [66]** | **Polypyrrole (PPy) [67]** | **Benzimidazole-based polymers (BBL) [68]** |
|---|---|---|---|---|
| **Charge Carrier Mobility ($cm^2/Vs$)** | ~ 0.1 | 0.1 to 10 | $10^{-3}$ to $10^{-2}$ | 0.1 to 0.5 |
| **ON/OFF ratio** | $10^3$ to $10^4$ | ~ $10^2$ | $10^2$ to $10^3$ | $10^4$ to $10^5$ |

**Poly(3-hexylthiophene) (P3HT)**

Among the organic semiconductors, poly(3-hexylthiophene) (P3HT), a conjugated polymer, has been extensively studied for use in IGTs due to its favorable properties, including solution processability, good charge carrier mobility, and mechanical flexibility.

P3HT-based IGTs typically operate at low voltages due to the formation of EDLs at the interface between the ionic gating medium and the semiconductor channel. This characteristic allows for the high accumulation of charge carriers, leading to effective transistor operation even under mechanical stress, making it ideal for flexible applications. P3HT transistors have demonstrated stability under bending conditions, with high MW P3HT films exhibiting stable mobility after several bending cycles, confirming their potential for use in stretchable and wearable electronics.

Frisbie et al. developed a P3HT transistor gated with an ion-gel based on [BMIM][PF6]. This transistor features a hole mobility of 0.6 $cm^2/V{\cdot}s$ and an ON/OFF ratio of $10^5$. Additionally, it has a gate capacitance of 40 $\mu F/cm^2$ and a response time of 1 ms at 10 Hz. The mobility of IGT reported on [EMIM][FAP]-gated P3DTV, P3HT, MEH-PPV and F8BT transistors is of 0.27, 0.86, 0.08 and 0.07 $cm^2V^{-1}s^{-1}$. [69]

Figure 2.4 illustrates the charge transport pathways both within and between polymer chains in semicrystalline conjugated polymers like P3HT and PBTTT, which often feature edge-on packing structures. The key directions for charge transport are primarily along the polymer backbone and through the $\pi$-stacks by the alternating single and double bonds in its backbone, which allows for

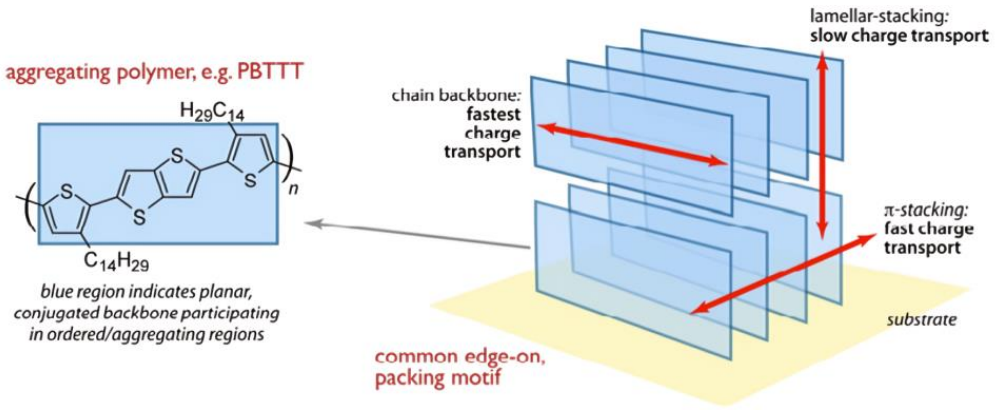


Figure 2.4 The three main directions for charge carrier transport in a semicrystalline polymer [70]

electron delocalization. Transport is less efficient when it occurs via hopping across lamellar stacks. Since hopping transport is significantly slower than delocalized transport, it serves as a limiting factor for the overall macroscopic conductivity of semiconducting polymers.

**Influence of MW of P3HT on IGT transistor parameters**

The MW of P3HT is a key factor in its solid-state structure and, consequently, the functional properties of organic electronic devices, such as IGTs. The relationship between MW and the performance of P3HT-based transistors has been extensively studied, revealing significant impacts on carrier mobility, crystallinity, and overall device efficiency.

The crystallinity of P3HT varies with MW. Ballantyne et al. showed that films made from low MW polymers exhibited relatively large crystalline nanorods, which generated a sharp XRD peak, indicative of the well-established lamellar π-stacking structure in crystalline P3HT. On the other hand, higher MW P3HT films displayed broader XRD peaks, suggesting a more disordered structure with smaller crystalline domains. [71] This enhanced crystallinity is beneficial for the performance of IGT transistors, as it reduces the resistance to charge flow and improves the device's electrical characteristics. Charge carrier mobility in P3HT is highly dependent on its MW. Shaheen et al. demonstrated that at higher MWs, the entanglement density increases, resulting in a larger proportion of amorphous regions. These disordered molecular domains exhibit reduced interchain and intrachain transport, along with higher trap densities, which hinder inter-lamellar transport and

decrease mobility. [65, 72] This transition is crucial for improving the performance of IGTs, as higher mobility facilitates faster switching speeds and overall device performance. [73, 74]

The efficiency of P3HT-based IGTs is directly influenced by the MW of the polymer. Studies have shown that devices fabricated with higher MW P3HT (e.g., 60 kDa and above) exhibit superior performance, largely due to an improved ON/OFF ratio associated with higher MWs. [73] Additionally, the increased MW leads to better film formation and stability, which are essential for the long-term reliability of the transistors. [75]

As MW increases, the viscosity of the semiconducting solution also rises, influencing both the thickness and morphology of the resulting thin films. Park et al. by using time-controlled spin-coating methods and AFM) revealed that the root mean square surface (RMS) roughness of the three MWs P3HT films (36 kDa, 69 kDa, and 90 kDa) increased as the MW decreased. However, with the increase of the MW, the thickness of the films increased (Figure 2.5a,b). [76]

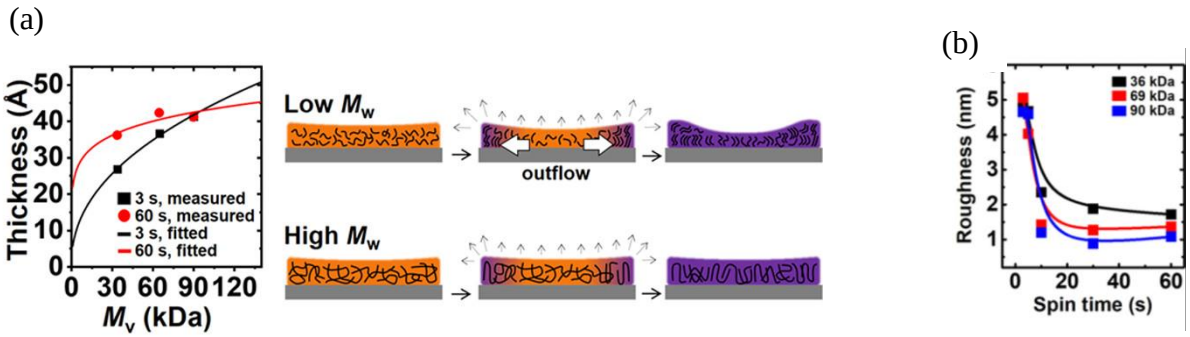


Figure 2.5 a) P3HT film thickness as a function of MW b) The RMS roughness of the P3HT film varies depending on MW and spin-coating duration. [76]

Higher MWs lead to more entangled polymer chains, which can increase the amorphous content of the material and affect its morphology. These structural variations influence the ion permeability and consequently, the doping efficiency when interfaced with an IL in IGTs. [16, 65, 71, 72]

**Metal oxide (MO) semiconductors**

Differently from organic semiconductors, metal oxides typically require quite high temperatures of thermal treatment. [77] Despite this processing challenge, metal oxides are highly valued in transistor technology for use as electrodes, semiconductors, and insulators. The semiconductor material in the transistor channel plays a crucial role in determining the overall performance of the device. Metal oxides, especially amorphous ones with post-transition metal cations, exhibit degenerate band conduction and high mobility (>10 $cm^2/Vs$), making them excellent candidates for flexible and transparent thin-film IGTs. [78] Their combined electrical and optical properties, along with their impressive reliability, make them particularly well-suited for such applications. Moreover, amorphous metal oxides offer superior mechanical properties, performance and durability compared to their polycrystalline counterparts, thanks to their uniformity and lower processing temperatures. [79]

**Tungsten Trioxide $WO_3$**

$WO_3$ exhibits a temperature-dependent crystal structure, transitioning through various phases as the temperature changes. This unique characteristic makes $WO_3$ a subject of considerable interest in materials science and various technological applications. At temperatures above 740 °C, it adopts a tetragonal structure, while between 330 and 740 °C, it becomes orthorhombic. From 17 to 330 °C, the structure is monoclinic, shifting to triclinic between −50 and 17 °C, and reverting to monoclinic below −50 °C.

The most common form of $WO_3$ is monoclinic. [80] This phase is particularly important because it is the most stable at room temperature, making it the most relevant for practical applications. One of the remarkable properties of tungsten trioxide is its electrical behavior. The pure compound is an electrical insulator, which means it does not conduct electricity under normal conditions. However, when $WO_3$ is oxygen-deficient, it can conduct electricity. Oxygen vacancies in the crystal lattice create free electrons, which enhance the material's conductivity. Figure 2.6 shows X-ray diffraction pattern of $WO_3$ thin film (after treatment at 500 °C).

$WO_3$ has a band gap of around 2.6–2.8 eV. [81] Gillet et al. studied how $WO_3$ conductivity changes with temperature under varying oxygen pressures. Additionally, factors such as dopants, microstructure

(including grain size, grain boundaries, and crystalline phase), and film thickness significantly impact conductivity. The electrical properties of $WO_3$ are highly influenced by the synthesis techniques and growth conditions. [82] The structure and size of nanocrystalline $WO_3$ films affect their electrical properties. $WO_3$ films at room temperature are amorphous and have lower conductivity. As the substrate temperature increases, the films become more crystalline leading to an improvement in conductivity. [83]

$WO_3$ is widely studied for its electrochemical properties, particularly its ability to undergo reversible redox reactions. When $WO_3$ is exposed to a potential in an IGT, it can intercalate ions such as $H^+$, $Li^+$, or $Na^+$, depending on the gating material used. This intercalation process results in the formation of

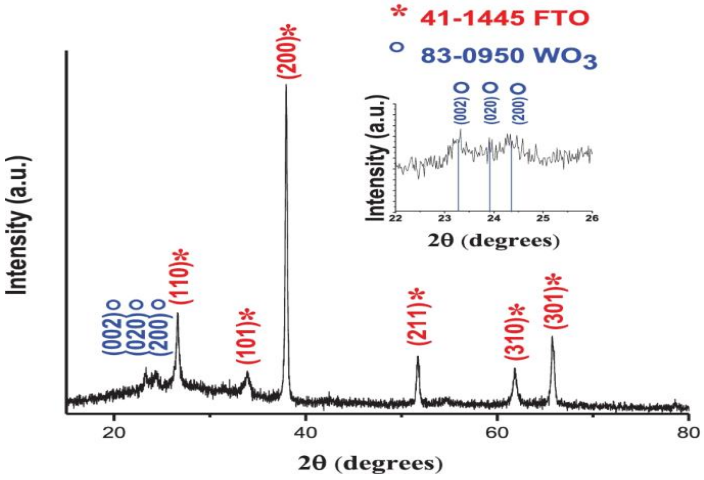


Figure 2.6 WO3 thin film XRD diffraction pattern after treatment at 500 °C [84]

tungsten bronzes ($H_xWO_3$, $Li_xWO_3$), which exhibit distinct colors and differences in electrical properties. The electrochemical intercalation of protons into $WO_3$ has been extensively explored in applications like electrochromic windows, where a reversible color change occurs due to changes in the tungsten oxidation state. The process can be described by the reaction:

$$WO_3 + xM^+ + xe^- \rightarrow M_xWO_3 \tag{2.8}$$

This reaction demonstrates how $WO_3$ can act as host material for ions (M), with the extent of proton intercalation affecting both the optical and electrical properties of the material. The intercalation

of ions is relevant in the context of transistors and energy storage devices such as batteries and supercapacitors.

The cyclic voltammetry (CV) technique is commonly employed to investigate the electrochemical behavior of $WO_3$. The CV profile of $WO_3$ typically shows distinct redox peaks corresponding to the injection/extraction of electrons (intercalation/deintercalation of cations). The shape of the peaks are usually indicate the reversible nature of the redox process. [84] In this thesis we synthesize our $WO_3$ film to have nanostructure and mesoporous properties

Nanostructured $WO_3$ exhibits unique properties, absent in bulk $WO_3$. When crystal size is below approximately 3 nm (e.g. nanostructures are quantum dots), the increased surface-to-volume ratio is paralleled by effects on electronic band structure, optical properties, and charge transport. [85] Furthermore, mesoporous $WO_3$ films possess a pore structure with diameters ranging from 2 to 50 nm [86] that facilitates the accessibility of the gating media ions in IGTs.

In the context of IGTs, $WO_3$ serves as channel material: when a positive $V_{gs}$ is applied, ions such as $H^+$ or $Li^+$ enter the $WO_3$ channel, increasing the charge carrier density and thus enhancing the channel conductivity. This effect is reversible, as removing the gate voltage leads to the deintercalation of ions and a corresponding decrease in conductivity. This dynamic doping mechanism allows $WO_3$-based IGTs to function as effective switches or modulators in low-power electronic applications. Morphological features, such as porosity and grain size, affect the conductivity and ion diffusion in $WO_3$ films in contact with gating media. Mesoporous $WO_3$ films, for instance, provide increased surface area for ion intercalation, enhancing the material's electrochemical response. [87]

## 2.6 The gating media in ion-gated transistors

The performance of IGTs is largely shaped by the physical and chemical properties of the ion-gating medium, which in turn determines the most appropriate applications for these devices. For example, IGTs used in chemical and biological sensing typically require a liquid gating medium, either aqueous electrolytes or ILs. However, polymer-based electrolytes offer different properties, such as a broader electrochemical potential window, adjustable viscosity, and ease of printability. Inorganic oxide electrolytes stand out for their superior thermal stability and wide potential stability

window, making them ideal for high-temperature applications. In this section, we provide an overview of the various ion-gating media used in IGTs, highlighting their key features and suitability for different uses. [88] Table 2.2 summarizes the properties of the ion-gating media utilized in IGTs, offering a comparison of their advantages across different application contexts. In this thesis, we employ the ILs for fabricating our IGTs.

Table 2.2 Ion-gating medium for the IGTs [88]

| **Gating medium** | **Capacitance (μF cm−2)** | **Thickness (μm)** | **Electrochemical window (V)** | **Working temperature (°C)** |
|---|---|---|---|---|
| **Ionic liquids** | 2–2000 | NA | ~3 | <400 |
| **Ion gels** | 1–200 | 0.05–400 | ~3 | <300 |
| **Aqueous electrolytes** | 1–10000 | NA | ~1 | <100 |
| **Polymer electrolytes** | 1–100 | 0.1–500 | ~3 | <300 |
| **Polyelectrolytes** | 0.2–3000 | 0.05–100 | ~3 | <300 |
| **Oxide electrolytes** | 0.5–1.6 | 0.02–1 | Can be > 5 V | <700 |

### 2.6.1 Ionic liquids

A salt in liquid form at ambient temperature is known as an ionic liquid (IL). Ordinary liquids like water and gasoline are mostly made up of electrically neutral molecules, whereas ionic liquids are

made up of ions. [89] ILs are composed of mobile ions such as asymmetric bulky organic cations and inorganic or organic anions. They are often referred to as environmentally friendly because of their non-volatility. As a result, they can be used as an alternative to traditional organic solvents. [90] The value of conductivity of ionic liquids at room temperature and ambient conditions is ca 0.1 S $cm^{-1}$. ILs have specific advantages for using as gating medium in IGTs. Wide electrochemical stability window (~ 3 V), high boiling point (> 400 ˚C) and low melting point (< 20 ˚C) are specific advantages. [91] ILs form high-capacitance EDLs, allowing for efficient charge doping of channel materials. As a result, ILs bring about low threshold voltages (Vth) and fast switching in IGTs. are Some of the disadvantages of using ILs in IGTs are sensitivity to moisture, which leads to reactions that reduce the electrochemical stability window, and incompatibility with some solution-processed organic semiconductors as a channel material, since ILs can act as solvents for semiconducting polymers.

Figure 2.7 shows an example of IL that has been used to gate IGTs in this thesis, [EMIM][TFSI], 1-ethyl-3-methylimidazolium-bis (trifluoro methyl-sulfonyl) imide. [59]

## 2.7 Models to describe the electrical characteristics of IGTs

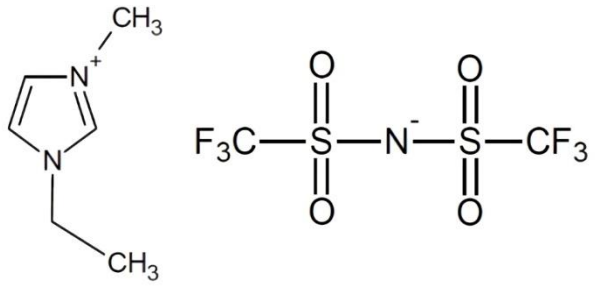


Figure 2.7 Chemical structure of 1-ethyl-3-methylimidazolium-bis(trifluoromethyl-sulfonyl) imide, [EMIM][TFSI].

In recent years, a growing number of semiconductors have been incorporated into IGTs. Despite this increasing diversity, the most widely recognized models explaining IGT device physics still predominantly focuses on depletion mode operation with p-type materials. These models can also be adapted to describe accumulation mode devices and n-type channel materials, allowing for the

extraction of key material-specific parameters. One of the most notable models, the Bernards-Malliaras model (Figure 2.8), explains the behavior of depletion mode OECTs. This model conceptualizes the OECT as consisting of two circuits: an electronic circuit that accounts for hole transport in the channel and describes steady-state characteristics, and an ionic circuit that represents ion transport, where ions move in the ion-gating medium and within the transistor channel material, influencing the transient characteristics This dual-circuit approach provides a comprehensive framework for understanding the complex interactions between ions and charge carriers in these devices. The model allows us to predict the device's dynamic behavior, providing insights into how quickly it can respond to applied voltages. [92]

### 2.7.1 Steady-state characteristics

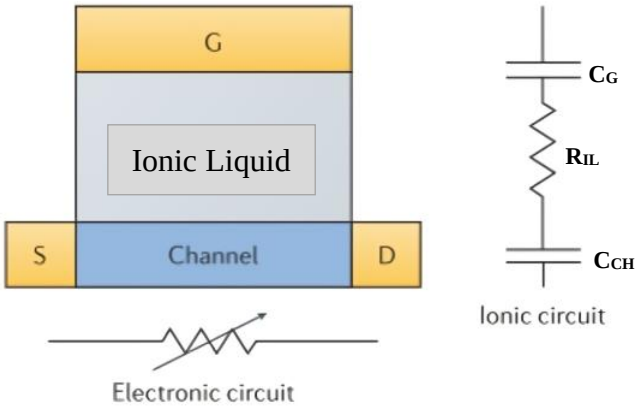


Figure 2.8 Scheme of ionic and electronic circuits of IGTs. The electronic circuit, depicted below the device, is represented as a resistor of the transistor channel whose resistance changes upon gating. The ionic circuit, shown on the right, consists of capacitors representing the channel (CCH) and gate (CG), along with a resistor representing the ionic medium (RIL). [93]

In the steady state, the characteristics of an IGT are typically described when the $I_{ds}$ reaches saturation. In this saturation region, the $I_{ds}$ is constant and independent of the $V_{ds}$. This happens after $V_{th}$ is exceeded and the channel in the transistor is fully turned on. $I_{ds}$ saturates because the electric field within the channel is strong enough to deplete or accumulate charge carriers, depending on whether the device operates in depletion or accumulation mode. The steady-state characteristics in IGTs can be modeled similarly to conventional transistors but with consideration

of ion-electronic interactions. The behavior of the electronic component in this regime in IGTs can be characterized using Ohm's law, while the ionic component is modeled as an ideal polarizable electrode, behaving similarly to a charging capacitor. The mathematical description of $I_{ds}$ in the saturation region is similar to a FET except that the transistor channel is described as a volumetric capacitor. This approach provides an accurate representation of the charge carrier dynamics within the IGT channel, where ionic penetration affects the entire volume of the material, rather than being limited to the surface.

### 2.7.2 Transient characteristics

Transient characteristics or response time ($I_{ds}$ versus time) are described as the time it takes for an applied change to a control system from an external source to reach a steady state.

The dynamic behavior of $I_{ds}$ in IGTs upon applying/removing of a constant $V_{gs}$ arises from two key processes within the device. First is the charging of the ionic circuit, reflected in the $I_{gs}$, and second is the injection or extraction of charge carriers (holes or electrons) in the channel, which modulates its electronic conductivity. In IGTs, especially those based on conjugated polymer channel materials, ionic conductivity through the ionic circuit is often more dominant than electronic conductivity in determining the dynamic behavior, particularly the response time. The transient $I_{ds}$ response can be described by Equation 2-9, following the Bernards model. [92] This equation captures the dynamic interplay between ionic motion and channel conductance, which governs the device's time-dependent behavior.

$$I_{ds}(t) = I_{ss}(V_{gs}) + \Delta I_{ss}\left[1 - f\frac{\tau_e}{\tau_i}\right]e^{-\frac{t}{\tau_i}} \qquad (2-9)$$

where $I_{SS}$ is the steady state $I_{ds}$ at saturation regime, $\Delta I_{SS}$ is the total change in the $I_{ds}$ after changing $V_{gs}$ from zero to a certain bias, $f$ is a weighting factor, $\tau_e$ is the electronic transit time, and $\tau_i$ is the

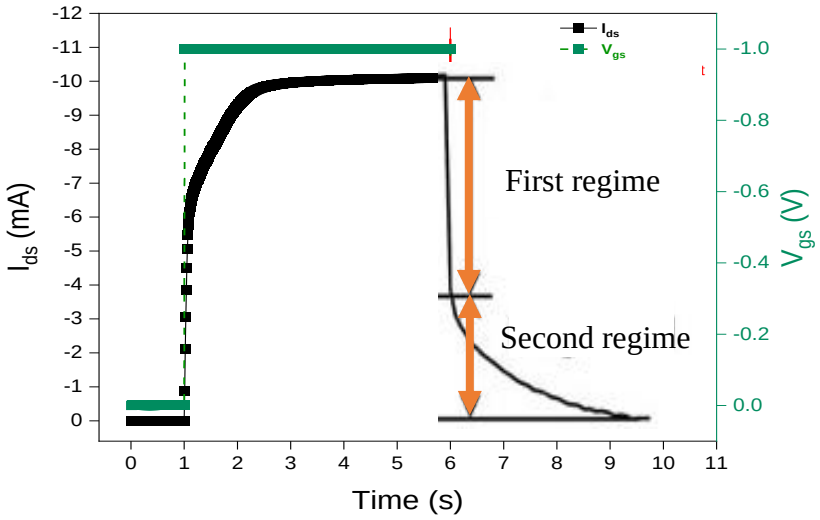


Figure 2.9 Two current decaying regimes in measuring response time of IGTs.

time constant, related to the electrostatic and electrochemical channel doping leading to the $I_{ds}(t)$ decay rate (which means the transistor response time).

Related to the transient response time, there are two types of current decaying regimes after removing constant $V_{gs}$. (Figure 2.9). The first, fast response reflects two distinct ionic mobility pathways: (i) ions move quickly over short distances at the interfaces, removing the EDL, and (ii) ions penetrate the semiconductor interface and redistribute rapidly. For the slower response, two possibilities exist: (i) the diffusion of ions over longer distances within the bulk of the channel material, leading to slower redistribution, and (ii) electrochemical doping of the semiconductor, where ions enter the channel layer to compensate for the charge carriers in that region, with electrochemical de-doping taking more time (Figure 2.9). [94] Fully turning off the transistor using this method would require the diffusion of anions out of the channel and into the gel or liquid, which may be a slow process.

## 2.8 Synaptic behaviors of a transistor

In biological neural networks, communication between two neurons occurs at synapses, which facilitate the transfer of chemical signals. The synaptic system consists of presynaptic and postsynaptic terminals, along with the synaptic cleft. Information transmission is regulated by the

release of neurotransmitters from the presynaptic terminal into the synaptic cleft, which are then received by receptors on the postsynaptic terminal of the next neuron. This process generates a postsynaptic potential (PSP), which can be excitatory (EPSP) or inhibitory (IPSP), and plays a crucial role in information processing, learning, and memory in the brain (Figure 2.10a). [95]

Recently, many synaptic devices have been developed that can emulate key synaptic functions, such as excitatory postsynaptic current (EPSC) and inhibitory postsynaptic current (IPSC), which are analogous to EPSP and IPSP, respectively. Another crucial synaptic function is synaptic plasticity, which involves the modulation of signal transmission strength or efficacy between neurons at the synapse. [96] Significant efforts have been made in the design and fabrication of synaptic devices aimed at emulating the plasticity of biological synapses. However, achieving the dynamic behavior of these artificial devices remains a challenge, and this is crucial for replicating

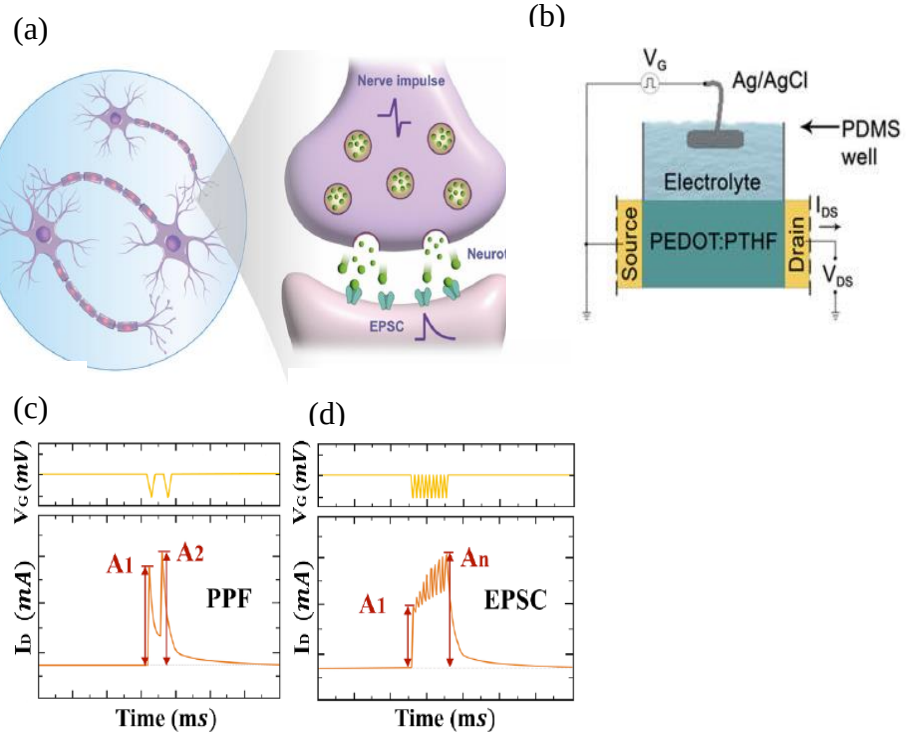


Figure 2.10 a) Schematic view of the biological synapse, b) Liquid electrolyte-based PEDOT:PSS OECT, c) PPF index of an IGT ($A_1$ and $A_2$ are the amplitudes of the first and second consecutive Ids pulses), d) SNDP index of an IGT. [95]

the complex neuromorphic functions observed in living organisms. Due to limitations in current

technology, and the low plasticity and adaptability of existing systems, artificial neural networks are still behind biological ones in terms of scale and complexity in processing information.

The basic concept involves applying an electrical signal to the gate electrode of artificial neurons, such as IGTs, which changes the current in the synaptic material through mechanisms like charge injection or ion movement. To replicate the functionality of biological neural circuits, artificial synapses need to exhibit neural functions such as STP and LTP. In IGTs, electrochemical doping occurs upon the application of $V_{gs}$. If ion movement modulates the conductivity of the channel for a short time, it is referred to as STP. If the modulation lasts for a longer period, it is known as LTP. [97, 98] As highlighted in the introduction, IGTs, such as OECTs and metal oxide-based IGTs, are among the best devices for emulating ion-dynamics-based biological synapses with low power consumption. These transistors, with their ion-induced capacitive behavior due to EDL formation, are widely studied for mimicking human synaptic functions. IGTs employing an electrostatic doping mechanism, specifically EDLTs, were among the first to be employed in emulating artificial synapses. Zhu et al. developed a laterally coupled IGT featuring a co-planar structure, incorporating a proton-conducting solid electrolyte and an indium zinc oxide channel.[99] The rapid reversibility of EDLTs to their (de)doped state enables effective replication of short-term plasticity in synapses, facilitating dynamic filtering and information processing. In addition to the electrostatic doping mechanism, the electrochemical doping mechanism such as OECT has garnered significant interest for its nonvolatile characteristics, making it suitable for emulating long-term plasticity. Malliaras et al. developed an OECT-based synaptic transistor using a liquid electrolyte and a PEDOT:PSS channel (Fig. 6a), which successfully exhibited synaptic behaviors like short-term plasticity STP and LTP (Figure 2.10b). [100]

It is essential for achieving both short-term and long-term potentiation within the same synaptic device for neuromorphic application. The capability of an IGT to exhibit STP or LTP relies on both the efficiency of ion transport and the time required for the device to reach a new equilibrium state after an electrical stimulus. The response time of a transistor is an important factor in plasticity measurement. Fast response times facilitate quicker changes in conductivity, allowing for dynamic adaptations in STP. Conversely, for LTP, sustained ion motion and retention of states over longer periods is required, which can be influenced by the overall response time of the device.

Artificial synaptic devices are also designed to mimic biological synapses by incorporating functions such as PPF, a common form of STP, as well as input voltages amplitude and duration dependent plasticity, SNDP, and frequency-dependent plasticity (FDP).

PPF occurs when two identical $V_{gs}$ pulses are applied at the gate in short intervals. This results in two consecutive peaks in the postsynaptic current, as illustrated in Figure 2.10c**Error! Reference s ource not found.**. [101] The facilitation effect is quantified by the ratio $(A_2 - A_1) / A_1$, where $A_1$ and $A_2$ represent the magnitudes of the first and second current peaks, respectively. This ratio characterizes the level of PPF observed in the device. [11]

When a series of pulsed $V_{gs}$ signals is applied at the gate, the excitatory EPSC shows an oscillating increase in $I_{ds}$ (as shown in Figure 2.10). This gradual adjustment in electrical conductance or synaptic weight due to the cumulative effect of repeated stimuli is referred to as SNDP. The SNDP index for IGTs is defined by the equation $(A_n - A_1)/A_1 \times 100\%$, where $n > 1$ represents the number of $V_{gs}$ pulses. SNDP is essential for simulating the learning and memory processes in artificial neural networks. [102, 103]

FDP is a form of synaptic plasticity where the changes in synaptic strength are influenced by the frequency of action potentials ($V_{gs}$). This type of plasticity is distinct from spike-timing-dependent plasticity (STDP), which relies on the exact timing of spikes. [104]

FDP can play a crucial role in neural coding and information processing by modulating synaptic strength based on the rate at which neurons fire. This mechanism allows neurons to adapt to different patterns of activity and can be important for various neural processes, including learning and memory. [105]. Plasticity can depend on the amplitude and duration of the input voltage. This type of plasticity involves changes in synaptic strength based on the amplitude and duration of the input $V_{gs}$ applied to the synapse. [106] In this thesis, we will employ these synaptic behaviors to achieve the transition between STP to LTP realizing both processing and memory functions in the single device which is one of the main requirements of neuromorphic applications.

# CHAPTER 3 METHODOLOGY

This chapter discusses several methods, including substrate preparation, gold patterning on substrates through microfabrication, fabrication of transistor channel materials using solution processing, the preparation of the ion-gating medium, the fabrication of the gate electrode, and the overall IGT device fabrication. Additionally, it covers the characterization of the device through ex situ and in operando methods.

## 3.1 The transistor fabrication

### 3.1.1 Substrate preparation

The substrate serves as the base for our top-gate, bottom-contact IGTs. We used a rigid $SiO_2$/Si substrate (WaferPro, USA), which consists of a wet thermal oxide layer (~200 nm) grown on the front side of polished single-crystal B-doped silicon (with a crystal orientation of <100>). This heavily doped p-type silicon has a thickness of approximately 500 μm and an electrical conductivity of about 650 S/cm. We selected this substrate for its smoothness, uniformity, and high-temperature tolerance.

Before deposition, we thoroughly cleaned the substrates using deionized (DI) water, isopropanol, acetone, and isopropanol, in that order, for 10 minutes each in an ultrasonic bath. After cleaning, we treated the substrate surfaces with UV-Ozone for 20 minutes to remove organic contaminants and improve the adhesion of the channel material films. The UV-Ozone cleaner (Jelight, Model 30) utilizes a low-pressure mercury vapor lamp with an intensity of approximately 30 mW/cm$^2$ and emits a wavelength of around 254 nm. To further enhance the surface properties and mitigate the potential negative effects of these trap states, an additional modification such as the application of a self-assembled monolayer (SAM) is recommended. Passivating the SiO2 surface with a SAM can neutralize reactive sites, reduce trap density, and improve the interface's electrical characteristics. This next-level modification not only stabilizes the surface but also provides a tailored chemical environment that enhances the overall performance and longevity of the transistor.

In our work, we ensured that the substrate of the IGTs was properly grounded during all measurements to avoid any unintended effects from the back gate (the conductive substrate beneath

the channel that can influence its electrostatic potential). This step was taken to stabilize the silicon potential and eliminate its influence on the transistor's output, ensuring that the performance was solely governed by the ion-gating mechanism. By grounding the back gate, we successfully mitigated potential drifts or instabilities in the transistor's behavior over time.

### 3.1.2 Microfabrication Process

We begin the transistor fabrication by patterning the golden source and drain electrodes via photolithography on $SiO_2$/Si substrates in the Microfabrication Laboratory (LMF) at Polytechnique Montreal. Photolithography is a process used to transfer geometric patterns onto a substrate from a photomask. It involves applying a positive photoresist, AZ 900 MIR, a photosensitive material, to the substrate. The photomask contains the desired pattern, which is exposed to UV light (365 nm). When the light passes through the mask, it alters the chemical structure of the photoresist in the exposed areas. This enables selective etching or deposition processes to create intricate patterns and structures on the substrate.

To form the metal contacts, the substrate with the patterned photoresist is covered with 5 nm of Ti to promote Au adhesion, followed by 40 nm of Au, which is deposited using e-beam evaporation at a rate of 0.5 Å/s. After the metal contact deposition, the excess metal is removed using a lift-off process, leaving the Ti/Au adhered to the silicon substrate in the desired geometry.

The electrodes consist of 40 nm-thick Au and typically feature an interelectrode distance (L) of 10 μm and an electrode width (W) of 4 mm.

### 3.1.3 Channel material preparation

To deposit highly uniform thin films (a few nanometers to several micrometers thick) at low cost, solution processing is the ideal method. In this PhD work, we used spin-coating as a common solution processing technique.

To prepare the solutions of the semiconducting materials, we identified optimized experimental parameters from the literature.

For P3HT solutions, we magnetically stirred 10 mg regioregular P3HT (RIEKE Metals) with different MWs, low (24 kDa), intermediate (50-70 and 42 kDa), and high (92 kDa), in 1 ml

chloroform overnight in an $N_2$ glove box ($O_2$ < 5 ppm, $H_2O$ < 5 ppm). Different MW can influence on morphology, solubility, and charge carrier mobility of semiconductor film. P3HT films were deposited by 30 seconds spin coating at 1000 rpm on the $SiO_2$/Si substrates. To control the thickness of the films, P3HT with MW 50–70 kDa were spin coated for 30 sec at various rotation speeds: 500, 1000, 2000, and 4000 rpm. The films were thermally treated with a hot plate at 100 °C for 2 h, always in the $N_2$ glove box. [107, 108]

The $WO_3$ precursor solution was synthesized using an aqueous sol-gel method. [131 Xiang]. Tungstic acid ($H_2WO_4$) was prepared by passing 20 mL of a 0.5 mol $L^{-1}$, $Na_2WO_4$ aqueous solution through a proton-exchange resin (Dowex 50WX2, 100-200 mesh), all sourced from Sigma Aldrich. The reaction in this step is as follows: $Na_2WO_4 + 2H^+ \rightarrow H_2WO_4 + 2Na^+$. Prior to use, the resin was preconditioned in 50 mL of 1 mol $L^{-1}$ $H_2SO_4$ for 30 minutes and thoroughly rinsed with deionized water (DIW) until the pH reached 7.0.

The eluted solution was then collected in 16 mL of ethanol under continuous magnetic stirring to slow down the condensation process. To concentrate the solution, it was reduced under low pressure and heating to reach a concentration of approximately 0.5 mol $dm^{-3}$. As an organic stabilizer, 4 mL of PEG-300 (sourced from Fluka Analytical) was added to the freshly evaporated solution, maintaining a $WO_3$/PEG-300 ratio of approximately 0.5 w/w. The resulting viscous, pale yellow precursor solution was kept under continuous stirring and stored in dark conditions. It was used to fabricate $WO_3$ films within three days to prevent precipitation. For film deposition, the precursor was spin-coated onto the device surface. This involved drop-casting 40 µL of the solution and spinning it at 4000 RPM for 40 seconds. The deposited layer was first dried at room temperature for 10 minutes, followed by annealing in a tubular furnace at 550 °C for 30 minutes under flowing oxygen. [14, 18, 109]

### 3.1.4 Ionic liquids purification

When used as gating materials for IGTs, ILs are highly susceptible to contamination by water, which is the main impurity affecting their performance. [110] For this reason, it is crucial to purify ILs before use. In this study, we used [EMIM][TFSI] IL, obtained from IoLiTec with a purity

greater than 99%. To ensure removal of impurities, the ILs were subjected to vacuum purification (approximately $10^{-5}$ Torr) at 80°C overnight before application. [111]

The [EMIM][TFSI] ILs have a melting point of -3 °C, a density of 1.52 g/cm³ (at 20°C), an ionic conductivity of 6.63 mS/cm (at 20°C), and a viscosity of 39.4 mPa·s (at 20 °C). Their electrochemical stability window, defined by anodic and cathodic limits, ranges from 2.6 to -2.1 V. [87, 111, 112] The molecular structures of [EMIM][TFSI] are illustrated Figure 2.7.

We drop-cast the IL onto a 4 mm × 9 mm polyvinylidene fluoride (PVDF) membrane (125 μm thick) with a pore size of 220 nm, then placed it on top of the device. The hydrophobic nature of the PVDF membrane ensures that, upon immersion in the IL, it becomes fully permeated by the IL itself. [113, 114]

### 3.1.5 Gate electrode preparation

Carbon paper pieces (6 mm × 3 mm, Spectracarb 2050A) were coated with 6 μL of high surface area carbon ink. The ink was prepared by mixing activated carbon powder (PICACTIF SUPERCAP BP10, Pica, 28 mg/mL) with a polyvinylidene fluoride (PVDF, KYNAR HSV900, 1.4 mg/mL) binder in N-methyl pyrrolidone (NMP, Fluka, > 99.0%) solvent. After coating, the carbon paper was dried under vacuum at 60 °C for 5 hours and subsequently stored in a $N_2$ glovebox ($H_2O$ and $O_2 \leq 5$ ppm). [115]

## 3.2 IGT materials characterization

### 3.2.1 Ex situ characterizations

**Atomic force microscopy (AFM)**

AFM is a powerful technique used to analyze the surface topography of films at the nanoscale. It operates by scanning a flexible cantilever across the surface in three dimensions, with the cantilever deflecting upon encountering surface features. The size of these features alters the reflection of a laser beam onto detectors, which measures the change in laser position relative to the height of the cantilever. AFM can be performed in three modes: (i) contact mode, (ii) non-contact mode, and (iii) tapping mode. In contact mode, the cantilever is repelled by the sample surface, while in non-contact mode, it is attracted to the surface. In tapping mode, the cantilever oscillates near or at its

resonance frequency as it interacts with the surface. This technique provides valuable information about surface characteristics such as roughness, cracks, and grain boundaries. In this PhD research, tapping mode AFM was used to examine the topographical features of P3HT and $WO_3$ metal oxide films under ambient conditions. The AFM images were taken using a Digital Instruments Dimension 3100 system with aluminum-coated silicon cantilevers.

**X-ray diffraction (XRD)**

XRD is a powerful technique used to characterize the structural properties of thin films, providing insights into crystallinity, crystal orientation, phases, composition, internal lattice strain, and particle size of crystalline materials. The principle of XRD is based on Bragg's law ($n\lambda = 2d\sin\theta$), which states that diffraction occurs when specific conditions are met as X-rays impinge on the planes of a crystal. In this PhD research, the crystal structure of the P3HT films and $WO_3$ metal oxide films were analyzed using Bruker D8 diffractometer with Cu Kα radiation ($\lambda = 1.54$ Å).

**Stylus Profilometry**

The thickness of thin films is measured using a stylus profilometer. In this method, the tip of the stylus is brought into contact with the sample's surface. As the stylus traverses the surface, it deflects according to the sample's height, and this deflection is detected by sensors. The average surface height, which is the difference between the thin-film side and the substrate side, is recorded in relation to the sample's lateral position. In this PhD research, we utilized the Dektak 150 stylus profilometer (Veeco, USA), equipped with a tip radius of 12.5 μm and applying a force of 10 mg, to accurately measure the thickness of the metal oxide films.

**Scanning Electron Microscopy (SEM)**

SEM is a widely used technique for investigating the morphology of samples by scanning their surfaces with a focused electron beam. This method produces different signals depending on the interaction points between the electron beam and the atoms in the sample. Secondary electrons, which are emitted from the sample's surface, provide detailed information about the sample's morphology, while backscattered electrons, originating from deeper within the sample, reveal the distribution of various elements. Additionally, characteristic X-rays are emitted when the electron beam displaces an inner shell electron from the sample, enabling quantitative analysis of its

chemical composition. In this study, SEM images were acquired using a Hitachi SU-8230 Cold Field Emission Scanning Electron Microscope (CFE-SEM), which features a 5 nm electron source size, and an energy spread of 0.2-0.3 eV.

### 3.2.2 In operando characterization

**Cyclic Voltammetry**

Cyclic voltammetry (CV) is a highly versatile technique used to extract various types of information, including analytical data (e.g., concentration), thermodynamic properties (e.g., redox potentials, equilibrium constants), kinetic parameters (e.g., reaction rate constants for electrogenerated species), and mechanistic insights into electrochemical reactions. [116, 117] In a typical CV experiment, a three-electrode setup is employed, consisting of a working electrode (WE), a reference electrode (RE), and a counter electrode (CE). During the experiment, the potential is scanned linearly in a triangular waveform while measuring the current between the WE and CE. This process can be repeated in single or multiple cycles at a fixed scan rate. [118]

For the CV characterization in this PhD thesis, we used in operando a two-electrode configuration. The channel layer situated between the source and drain electrodes served as the WE, while activated carbon paper functioned as both the CE and a quasi-reference electrode, short circuited. The electrolyte in these experiments was IL. The electrochemical measurements were carried out using a VersaSTAT4 multichannel potentiostat at three different scan rates: 10, 50, and 100 mV $s^{-1}$.

In cyclic voltammetry, a reference electrode, such as Ag/AgCl, is critical for providing a stable and well-defined potential against which the working electrode's potential is measured. However, in a two-electrode configuration, the reference and counter electrodes are combined into a single electrode, often referred to as a "pseudo-reference" electrode. This setup simplifies the electrochemical cell but results in a pseudo-reference electrode whose potential may not be as stable or well-defined as a true reference electrode.

To mitigate this limitation, activated carbon can be employed as a reference electrode in the two-electrode IGT configuration. Activated carbon offers several advantages, including a broad potential window, good conductivity, and chemical stability. While it may not provide the same

level of potential stability as conventional reference electrodes, it is a practical choice for certain applications such as IGTs configuration. [119, 120]

**Atomic Force Microscopy Force-Distance (AFM FD)**

AFM FD profiling is a technique used to study the mechanical properties and surface characteristics and interactions at the surface of a sample at the nanoscale. AFM FD profiling is widely used to investigate soft materials, thin films, and biological samples. In AFM FD measurements, the cantilever tip of the AFM approaches and retracts from the surface in a controlled manner, while the force exerted on the tip is measured as a function of the distance between the tip and the sample. Unlike typical AFM measurements that scan horizontally across the sample surface, FD profiling focuses on the vertical movement of the probe. As the tip approaches the surface, attractive or repulsive forces cause deflection of the cantilever, which is recorded to generate a force-distance curve. These curves provide insights into various surface properties, including adhesion forces, stiffness, elasticity, and surface energy. [18]

In this dissertation, AFM-FD profiling was employed to investigate the structure of the EDL in $WO_3$-based IGTs using either [EMIM][TFSI] or a solution of 0.1 mol $L^{-1}$ LiTFSI in [EMIM][TFSI]. Force-distance profiles were acquired with a Cypher AFM (Asylum Research, Oxford Instruments, UK) and an SP-300 two-channel potentiostat (Biologic) at Oak Ridge National Laboratory (ORNL), USA. This technique allowed us to study the ionic organization at the interface between the IL and MO films in operando conditions during transistor operation. By analyzing the force-distance profiles, we could observe the ionic layering at various points on the channel surface and examine the patterns formed in the force-distance diagrams based on the vertical movements of the AFM probe tip.

## 3.3 Electrical characteristics

By connecting an Agilent B1500A semiconductor parameter analyzer to a house-made micromanipulated electrical probe station located in the $N_2$ glove box or vacuum ($10^{-4}$ Torr), we carried out the characterization of the IGTs. There are two primary sets of current-voltage curves

to be acquired for the electric characterization of transistors: transfer curves that show $I_{ds}$ versus $V_{gs}$ at constant $V_{ds}$ and output curves that show $I_{ds}$ versus $V_{ds}$ with a constant $V_{gs}$. We used the same semiconductor parameter analyze using the EasyEXPERT software to record pulse base parameters like response time synaptic behaviors.

# CHAPTER 4 ARTICLE 1: ON THE FACTORS AFFECTING THE RESPONSE TIME OF SYNAPTIC ION-GATED TRANSISTORS

## 4.1 Authors

Ramin Karimi Azari*[a], Tian Lan[a] and Clara Santato*[a]

[a]Engineering Physics, Polytechnique Montreal, 2500 Ch. Polytechnique, H3T 1J4, Montreal, QC, Canada.

*Corresponding Authors: Ramin Karimi Azari, Clara Santato

Name of journal: Journal of Materials Chemistry C

Date of publication: May 10, 2023

## 4.2 Abstract

Ion-Gated Transistors (IGTs) feature the processing rate of the human brain for neuromorphic computing. Further, they require low power for training and deployment of neural network algorithms. Neuromorphic computing requires both long-term and short-term potentiation, within the same device. The nature of the doping mechanism in IGTs affects their time-resolved properties, key for their use as neuromorphic devices. Depending on the permeability of the semiconducting channel to ions, IGTs undergo electrochemical (three-dimensional) or electrostatic (field-effect, two-dimensional) doping, which leads to a wide range of IGT response times. Here, we propose a methodology to control the response time of IGTs made up of films of poly(3-hexylthiophene (P3HT) as the semiconducting channel and the ionic liquid 1-Ethyl-3-methylimidazolium Bis(trifluoromethanesulfonyl)imide [EMIM][TFSI] as the gating medium. The methodology includes the effect of the pulse frequency of the applied gate-source voltage ($V_{gs}$), the number of applied $V_{gs}$ pulses, and the $V_{gs}$ pulse duration. It also considers the effect of the values of the applied $V_{gs}$ and drain-source ($V_{ds}$) voltages. Last but not least, the methodology includes the effect of the $V_{gs}$ sampling time. Our results contribute to understand how to achieve plasticity in IGTs.

## 4.3 Introduction

Ion-Gated Transistors (IGTs) make use of ionic compounds as the gating media. IGTs play a crucial role in the development of neuromorphic computing devices, due to their low operating voltages (sub-1 V), viable functionalization of the semiconducting channel for chemo and biosensing purposes, and possible fabrication into large device arrays. [121, 122] Due to combined electronic and ionic transport, [123-125] IGTs are relevant for future computation, bioelectronics, and electrochemical energy storage. [7, 92, 126-129]

Since the electrical double layer (EDL) at the interface between the semiconducting transistor channel and the ion gating medium is thin (3-4 nm), the specific capacitance observed in IGTs can be as high as 10 $\mu Fcm^{-2}$, bringing about a large density of charge carriers (about $3\times10^{15}$ $cm^{-2}$), at low $V_{gs}$ biases. [130-132]

Several working mechanisms are possible for IGTs based on organic semiconducting channel materials, depending on the degree of permeability of the channel to ions. Ion-impermeable channels are electrostatically doped (as in conventional field-effect transistors, where the doping is *bidimensional*) whereas ion-permeable channels can be electrochemically doped (in this case the doping is three-dimensional). [133]

Certainly, IGTs can feature a combination of these two working mechanisms, where the weight of each contribution depends on the specific semiconductor and gating medium, the quality of their interface, and the electrical biasing conditions. For instance, in organic single crystal channels poorly permeable to ions, upon application of a gate-source voltage ($V_{gs}$), ions accumulate at the ionic medium-organic semiconductor interface, bringing about electrostatic doping. [132, 134-137]

The nature of the ionic medium (e.g., solid, gel, or liquid) influences the movement of the ions in the gating media of IGTs, in turn affecting the transistor performance and response time. [92, 138-142]

Room-temperature ionic liquids (ILs) are ideal gating media for IGTs since they feature high conductivity (0.1-20 mS $cm^{-1}$), a wide range of viscosity (10-1000 mPa s), and minimal volatility. [143, 144] Further, their electrochemical stability window can be as high as 5 V. [134, 145, 146]

We can establish a correspondence between the working principle of IGTs and fundamental processes taking place in the brain (Figure 4.1a). In the human brain, a neuronal network of around $10^{11}$ neurons is linked by approximately $10^{15}$ synapses. Synapses are a passageway for conveying action potentials from presynaptic to postsynaptic neurons. They carry out parallel information computing (processing and memorizing information) by adjusting the synaptic weight, i.e. the strength of a synaptic connection [147] (with the term synaptic strength referring to the amount of current generated in the postsynaptic neuron as a result of an action potential in the presynaptic neuron).

The rate of enhancement in the current amplitude after the second of two repetitive excitatory postsynaptic potentials (EPSPs) with an interval $\Delta t$ is an index of the increase of the synaptic strength in a synaptic transistor, measured as paired pulse facilitation (PPF), defined as $(A_2-A_1)/A_1\times 100\%$ (Figure 4.1c). [148]

The three-terminal IGT closely resembles the biological synapse (Figure 4.1a-b) since the gate electrode acts as a neuron that applies the presynaptic spike ($V_{gs}$) and generates a postsynaptic current (PSC) spike in the semiconducting channel (acting as a postsynaptic neuron), between source and drain electrodes (drain-source current, $I_{ds}$).

In an IGT artificial synapse, the synaptic plasticity can be described as the alteration of the synaptic weight, the IGT channel conductivity. [7] The synaptic weight is modulated independently via the gate terminal, in an IGT. [60] Short-term plasticity (STP) and long-term plasticity (LTP) are two categories of synaptic plasticity. A persistent modification of synaptic weight, LTP, supports memory and learning and lasts longer than a transient modification, STP. STP is necessary for data processing, encoding and filtering. [149, 150]

An important aspect of synaptic plasticity modulation in IGTs is its response time, e.g., the time it takes for the PSC of a transistor to reach a steady state after removal of the $V_{gs}$ bias.

Response time can vary depending on the specific device structure, materials, and operating conditions.

We can consider two contributions to the $I_{ds}$ decay in IGTs. The former is a fast current decay due to the removal of electrical double layers and/or ions located within a thin depth in the channel.

The latter is a slow current decay related to the removal of the ions located deep in the channel and/or trapped. [92, 142, 151, 152]

According to Bernards[92], in IGTs, the response time of $I_{ds}$ with respect to a change in $V_{gs}$ can be fit by exponential functions. $I_{ds}(t)$ for the case of a square $V_{gs}$ step follows a time dependence given by:

$$I_{ds}(t) = I_{ss}(V_{gs}) + \Delta I_{ss}\left[1 - f\frac{\tau_e}{\tau_i}\right]e^{-\frac{t}{\tau_i}} \tag{4.1}$$

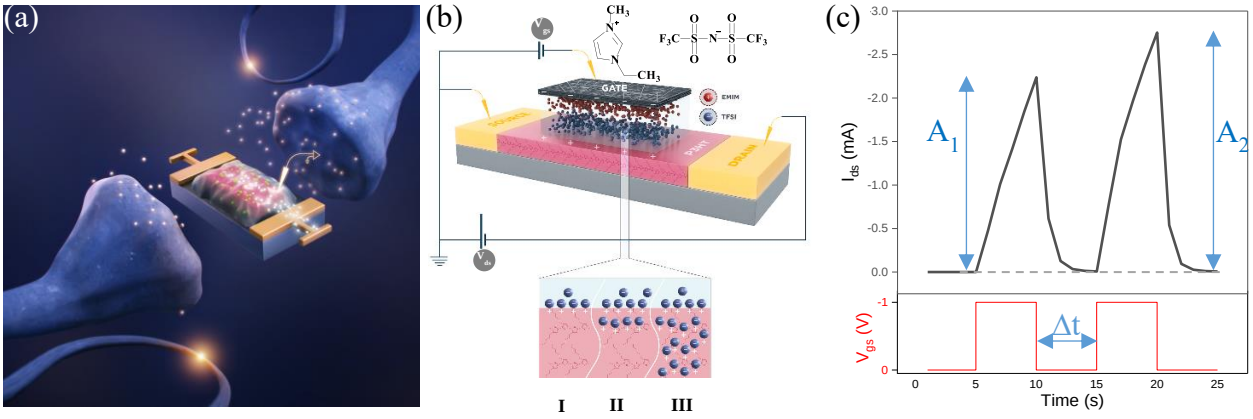


Figure 4.1 a) Bio-inspired synaptic IGT transistor. b) Device scheme and possible doping regimes (I to III) upon application of a negative $V_{gs}$ to a P3HT-based IGT; molecular structures of the ions constituting the ionic liquid employed as gating medium in this study. c) A pair of successive $V_{gs}$ inputs (-1 V) for 5 s with a pulse interval $\Delta t = 5$ s applied to an IGT. $A_1$ and $A_2$ are the amplitudes of the drain-source current ($I_{ds}$).

where $I_{ds}(t)$ is $I_{ds}$ at time t, $I_{ss}(V_{gs})$ is drain current at $V_{gs}$, $\Delta I_{ss}$ is the difference between the initial and final (steady state) drain currents, f is a weighting factor, $\tau_e$ is the electronic transit time along the channel, and $\tau_i$ is the time constant related to the $I_{ds}(t)$ decay rate, i.e. the transistor response time.

The majority of organic synaptic devices can only partially mimic synaptic plasticity, either LTP or STP, depending on the doping mechanism. One of the most significant challenges in IGTs is to transition plasticity from STP to LTP and vice versa in a single device and control the response

time for various applications. [153-155] To tackle this challenge, aspects pertaining to the chemical nature and structure of the channel material and ionic medium, device structure and electrical bias input stimuli, should be all considered. [147]

In this study, we control the synaptic plasticity and response time of IGTs by controlling input $V_{gs}$ and $V_{ds}$ stimuli to modulate STP and LTP. We employed Poly(3-hexylthiophene) (P3HT) as the organic transistor channel material, gated with the ionic liquid (1-Ethyl-3-methylimidazolium Bis(trifluoromethanesulfonyl)imide) ([EMIM][TFSI]) (Figure 4.1b). We studied various aspects of bio-inspired synaptic transmission in [EMIM][TFSI]-gated P3HT transistors, such as spike frequency-dependent plasticity (SFDP) (defined as $(A_5-A_1)/A_1\times100\%$ for different frequencies of $V_{gs}$ for a train of five pulses) and spike number-dependent plasticity (SNDP) (defined as $(A_n-A_1)/A_1\times100\%$ where n>1 is the number of $V_{gs}$ pulse). Furthermore, we investigated the influence of the sampling time of applied $V_{gs}$ on the measured response time.

## 4.4 Results and discussion

### 4.4.1 Film morphology

AFM images show that the spin-coated P3TH films are continuous, with a root mean square (rms) roughness of ca. 3.77 ± 1.04 nm in a 10 μm × 10 μm-sized area (Figures A1a-c). The XRD patterns of the P3HT films show a peak related to the lamellar structure located at $2\theta=5.1°$ (Figure A1d). [156]

### 4.4.2 Transfer and output characteristics of [EMIM][TFSI]-gated P3HT transistors

The IGT transfer and output characteristics show a typical p-type behavior of transistors working in accumulation mode. We observed that the hysteresis decreases with the $V_{gs.}$ scan rate from 100 to 5 $mVs^{-1}$ due to the increased time available to accommodate ion movement (Figures 42a and A2a-c). We deduced a threshold voltage of ca. -0.4 V, ON/OFF of ca. $10^2$, mobility of 0.1 $cm^2V^{-1}s^{-1}$, and charge carrier density of $3.0\times10^{15}$ $cm^{-2}$, at 100 $mVs^{-1}$ (values obtained at 50, 25, and 5 $mVs^{-1}$ are reported in Table A1).

### 4.4.3 Influence of the value of $V_{gs}$ on the response time

We performed a typical $I_{ds}$ transient response characterization (Figure 4.2b, c) using a 200 ms-long square $V_{gs}$ pulse with amplitudes -0.5 and -1 V, at $V_{ds}$ = -0.2, -0.6, -0.8, and -1 V. Low amplitude $V_{gs}$ (pre-synaptic spike) pulses are expected to induce the formation of electrical double layers and

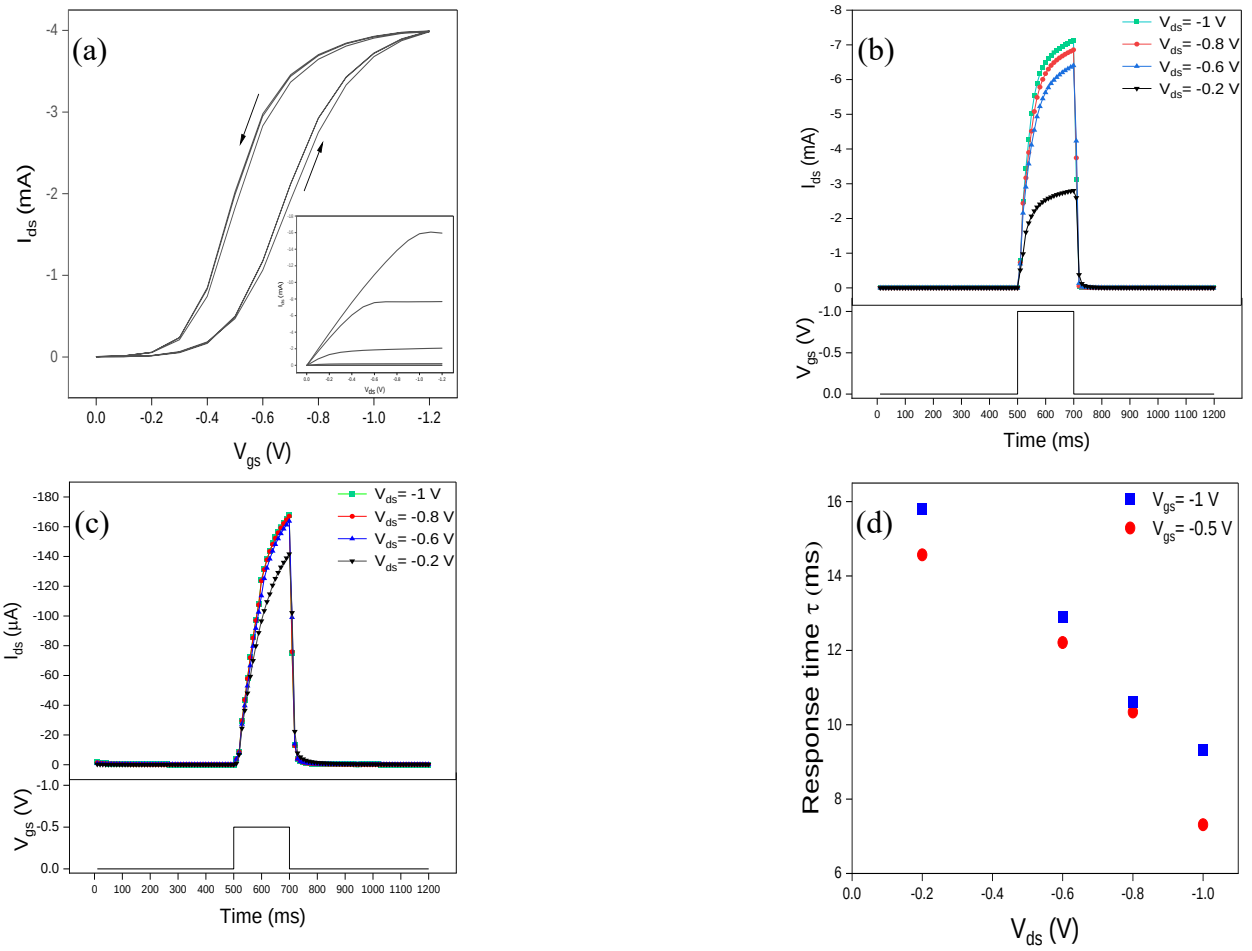


Figure 4.2 Characteristics of [EMIM][TFSI]-gated P3HT transistors. a) Transfer characteristics in the linear regime ($V_{ds}$ = -0.2 V, (3 cycles)) at $V_{gs}$ 100 $mVs^{-1}$ scan rate (inset: output characteristic with $V_{gs}$= 0, -0.2, -0.4, -0.6, -0.8, -1 V and $V_{ds}$ 100 $mVs^{-1}$ scan rate). $I_{ds}$ response to b) $V_{gs}$= -1 V, c) $V_{gs}$= -0.5 V, at different $V_{ds}$. The duration time of the $V_{gs}$ bias is 200 ms. d) Transient response of an [EMIM][TFSI]-gated P3HT transistor versus Vds in different values of $V_{gs}$ square step.

dope regions in P3HT close to the interface and/or amorphous. These regions can rapidly de-dope and PSC rapidly decays; this response is analogous to STP. We observed that the response time increased with the increase of $V_{gs}$. For instance, increasing $V_{gs}$ from -0.5 V to -1 V ($V_{ds}$ = -1 V)

increases the response time from 7.31 to 9.33 ms, i.e. by 27%. Higher values of $V_{gs}$ induce a deeper anion penetration in the film, possibly including crystalline regions. This implies longer times for ions removal prior reaching the steady state, after the removal of $V_{gs}$ (Figure 4.2d).

### 4.4.4 Influence of the value of $V_{ds}$ on the response time

We observed that the response time halves in a quasi-linear trend, in the region of $V_{gs.}$ Included between -0.5 V and -1 V (Figure 4.2d). According to Bernards' model (Equation 1), the ratio $\tau_e/\tau_i$ is determined by $\tau_e/\tau_i \sim dL^2/\mu V_{ds}$ where d is the ionic gating medium thickness, L is the channel length and other symbols have been already introduced. In agreement with the model, the increase of $V_{ds}$ is expected to cause the decrease in the response time; this is actually what we observed.

### 4.4.5 Effect of the number of $V_{gs}$ pulses on the response time

To explore the synaptic properties of [EMIM][TFSI]-gated P3HT transistors, we applied an increasing number of $V_{gs}$ pulses (5, 10, and 25). As the number of pulses increased, so did the response time. Upon application of a $V_{gs}$ pulse, ions move towards/into the channel materials (Figure 4.3). With increasing the number of pulses, the time needed for the anions to redistribute in the p-type P3HT increases, since they penetrate deeper into the film, which can include ion traps. This result can be exploited to drive the device transition from STP to LTP. In other words, the repetition of the stimuli leads to a learning process, in our synaptic IGTs.

We observed that $SNDP_{1\text{-}5}$ (where $SNDP_{1\text{-}n}=(A_n-A_1)/A_1\times100\%$) is 13%, $SNDP_{1\text{-}10}$ is 15%, and $SNDP_{1\text{-}25}$ is 17%. These values quantitatively describe the evolution of the SNDP index for our synaptic IGTs.

### 4.4.6 Impact of the pulse duration time on response time

Increasing the pulse duration time brings about more time for the ions to penetrate the channel. This leads to an increase in the de-doping time and, in turn, an increase in the response time upon removal of the $V_{gs}$ bias. According to Figures 4.4a and 4.4b, increasing the pre-synaptic spike pulse duration time from 10 ms to 9 s, at $V_{gs}$ = -1 V, induces an increase of the amplitude of the excitatory postsynaptic drain-source current (EPSC), suggesting a more important synaptic weight change. Literature on IL-gated P3HT transistors reports response times depending on the specific device

pulses. The duration and interval of each $V_{gs}$ pulse is 200 ms; exponential fits used to estimate the response time are in red. structure and operating conditions. [12, 147, 157] Frisbie et al., observed

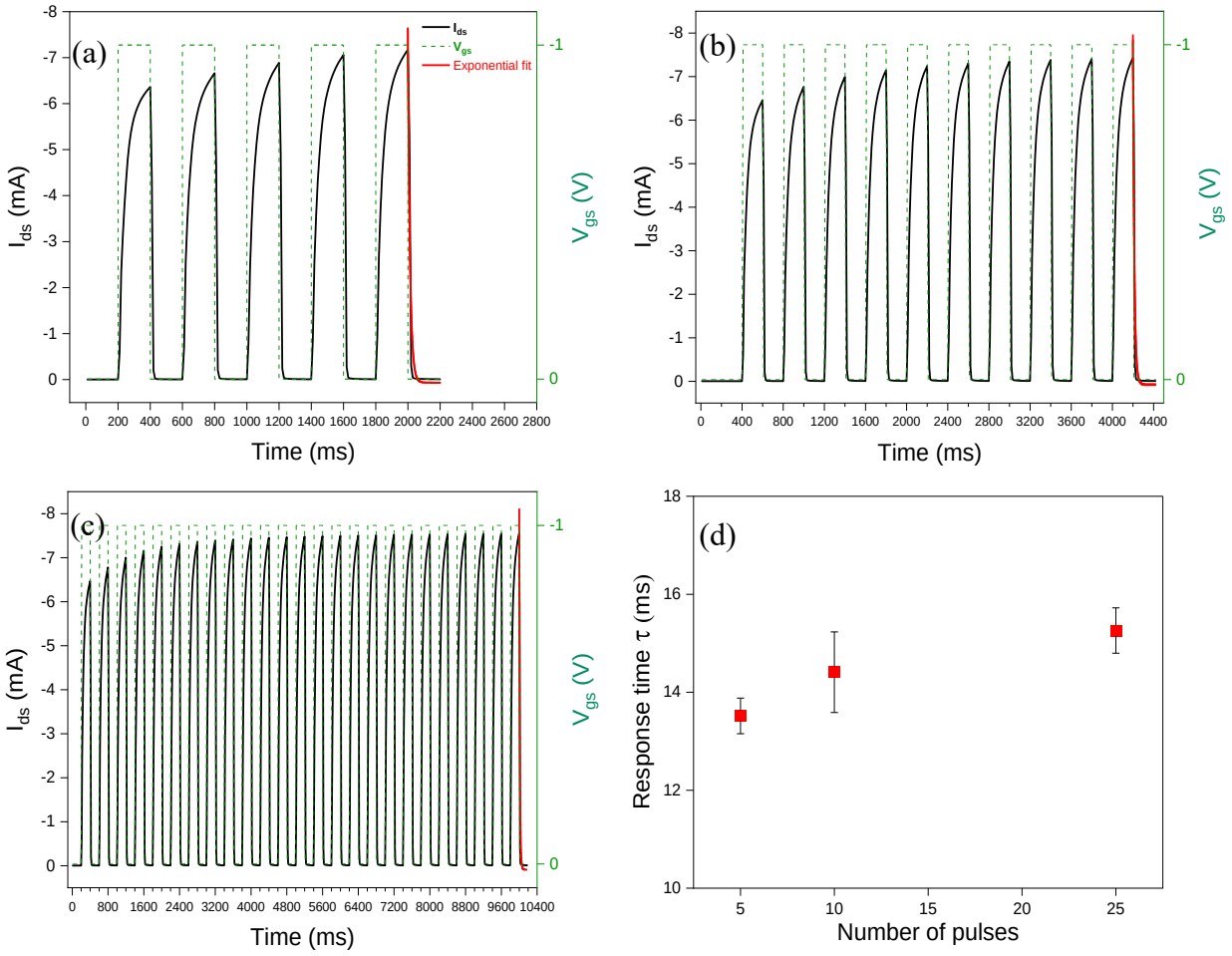


Figure 4.3 Transient $I_{ds}$ response of [EMIM][TFSI]-gated P3HT transistors in response to different numbers of $V_{gs}$ square step train pulses. $V_{gs}$ = -1 V at $V_{ds}$= -0.6 V a) 5 pulses, b) 10 pulses, c) 25

a response time of about 1 ms for ion-gel-gated P3HT transistors with $V_{gs}$ = -3 V and pulse duration of 0.5 ms. [147]

### 4.4.7 Impact of the frequency of the $V_{gs}$ pulses on the response time

Given the inverse relationship between frequency and pulse duration time, response time is expected to decrease as the frequency of the $V_{gs}$ increases (Figures 4.4c-f). This observation is

explained by considering that the decrease in the duration time of the $V_{gs}$ pulses brings about a shorter time for ion penetration in the channel (and therefore a shorter depth of penetration of the

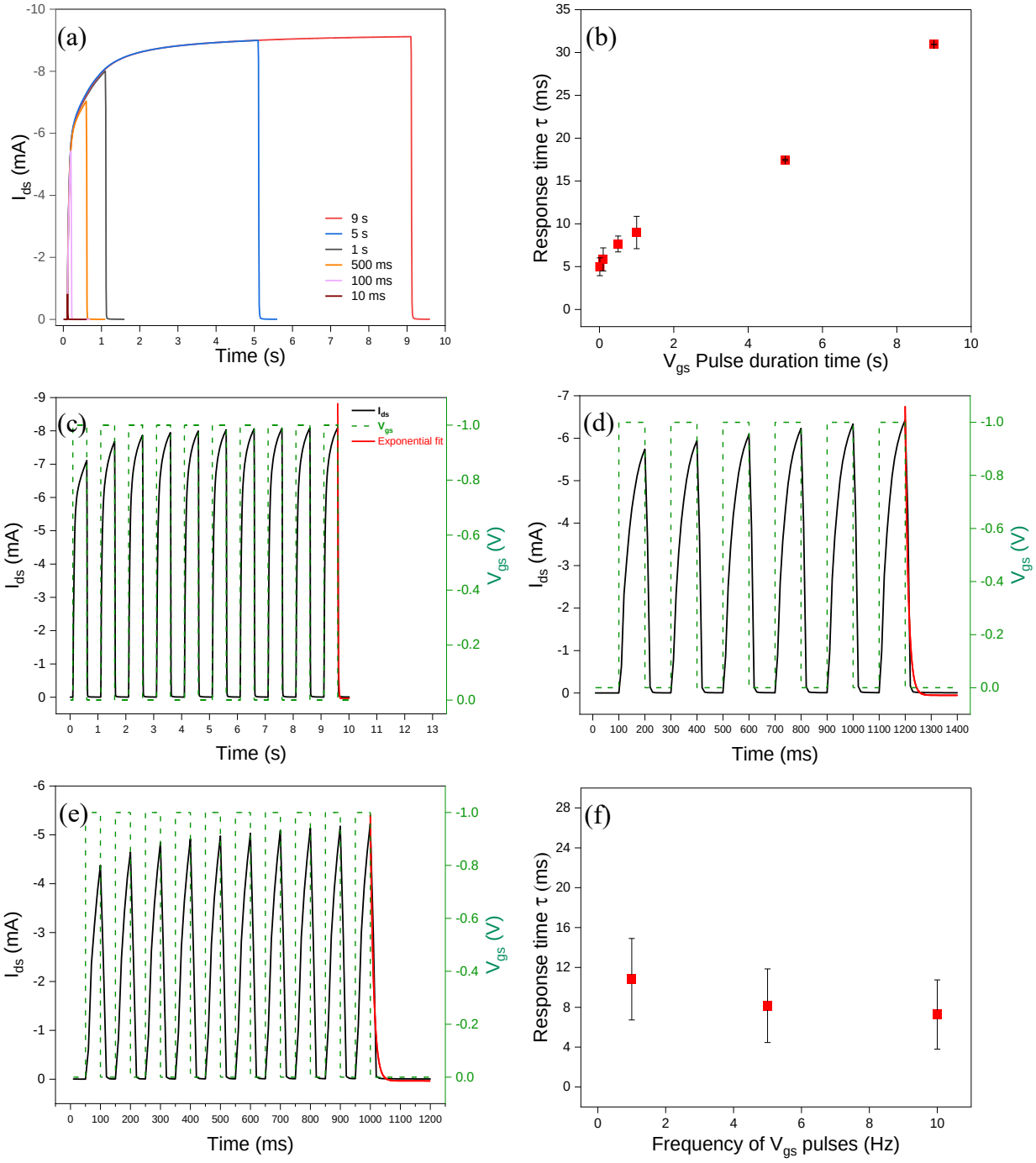


Figure 4.4 a, b) Transient $I_{ds}$ characteristics response of an [EMIM][TFSI]-gated P3HT transistor versus different duration times. Transient response of transistor in response to $V_{gs}$ pulses with a

different frequency c) 1 Hz, d) 5 Hz, e) 10 Hz. f) response time versus frequency of $V_{gs}$ pulses. ($V_{gs}$ = -1 V, at $V_{ds}$ = -0.6 V).

ions in the P3HT film). This finding reminds of the spike frequency-dependent plasticity (SFDP) of the biological synapses. The SFDP index after six consecutive spikes at frequencies included between 1 Hz and 25 Hz increased from 12% to 15%.

### 4.4.8 Importance of the $V_{gs}$ sampling time on the measurement of the response time

We investigated the impact of the sampling time of square $V_{gs}$ pulses (with a constant duration time) on the response time. The sampling time is the time difference between two $V_{gs}$ readings taken at two consecutive instants, during the measurement; it permits to convert a continuous-time signal into a discrete-time one. By decreasing the sampling time during transient responses, it is possible to obtain more accurate $I_{ds}$ measurements and, in turn, more accurate evaluation of the time response (Figure 4.5 and Figure A3).

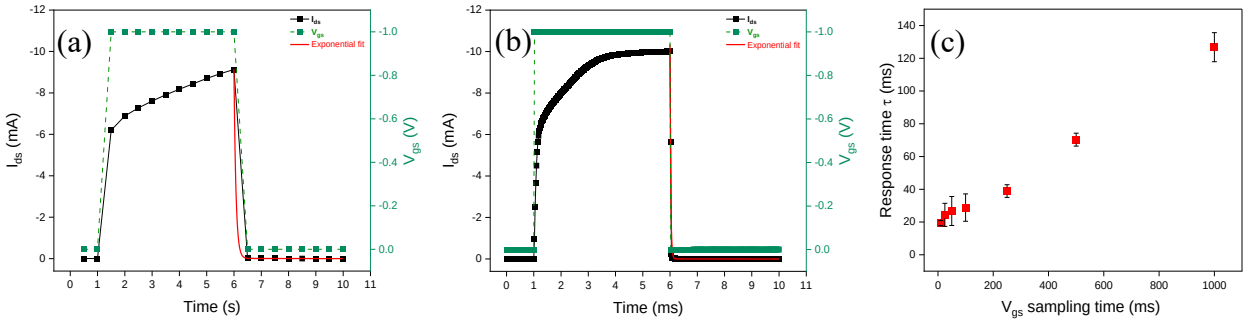


Figure 4.5 Transient response of an [EMIM][TFSI]-gated P3HT transistor at different $V_{gs}$ pulse sampling times: a) 500 ms, b) 25 ms; the duration of $V_{gs}$ pulse is 5 s. c) Response time versus different $V_{gs}$ sampling times (10, 25, 50, 100, 200, 500, 1000 ms) at $V_{ds}$= -0.8 V.

## 4.5 Experimental

Films of P3HT with regioregular intermediate molecular weight (50-70 kDa, RIEKE metals), deposited on bare $SiO_2$/Si substrates, were employed as channel materials of our [EMIM][TFSI]-

gated IGTs. $SiO_2$/Si substrates were photolithographically patterned with source and drain electrodes (40 nm-thick Au on 5 nm-thick Ti adhesion layer) with interelectrode distance, L, of 10 μm and width, W, of 4 mm. Prior to the deposition of the P3HT films, the substrates were cleaned with sequential steps of 10 min in isopropyl alcohol, 10 min in acetone and 10 min in isopropyl mg P3HT in 1 ml chlorobenzene were stirred overnight in an $N_2$ glove box (<5 ppm $O_2$, $H_2O$).

P3HT films were deposited by spin-coating on the pre-patterned $SiO_2$/Si substrate and placed on a hot plate at 140 °C for 2 hours in the $N_2$ glove box. [EMIM][TFSI] (IoLiTec, >99%)) was purified under vacuum conditions (ca $10^{-5}$ Torr) for 24 hours at 60 °C before use. The ionic liquid was dropped on a DuraporeR membrane (typically 4 mm × 9 mm-sized and 125 μm-thick) located in correspondence of the transistor channel. The gate electrode was a high surface area of carbon paper (Spectracarb 2050), 6 mm×3 mm-sized, 170 μm-thick, coated with an ink made of activated carbon (PICACTIF SUPERCAP BP10, Pica, 28 mg ml-1) and polyvinylidene fluoride (PVDF, KYNAR HSV900, 1.4 mg ml-1) binder in N-methyl pyrrolidone (NMP, Fluka).

### 4.5.1 Characterization of the films

Atomic Force Microscopy (AFM) images were taken in the air, at room temperature, on a Digital Instruments Dimension 3100, in tapping mode, with Al-coated silicon cantilevers. X-ray diffraction (XRD) spectra of the P3HT films were taken using a Bruker D8 diffractometer with a wavelength (CuKa) of 1.54 Å. 1100 nm).

### 4.5.2 Electrical characterization of the devices

Transistor characteristics were obtained using an Agilent B1500A semiconductor parameter analyzer connected to a house-made micromanipulated electrical probe station located in the $N_2$ glove box.

## 4.6 Conclusions

We studied P3HT-based Ion-Gated Transistors (IGTs) as bio-inspired synapses for applications in neuromorphic systems. We investigated the response time and synaptic plasticity of P3HT IGTs

by engineering input stimuli such as values of $V_{gs}$ and $V_{ds}$, number of pulses of $V_{gs}$, $V_{gs}$ pulse duration time and frequency.

Response time and plasticity increased with the value of the applied $V_{gs}$ and $V_{gs}$ pulse duration. We were also able to emulate synaptic functions such as short-term plasticity (STP) and long-term plasticity (LTP), and the transition between the two.

We achieved an increased response time via repeated $V_{gs}$ presynaptic stimuli (spike number-dependent plasticity (SNDP)) and by decreasing pulse frequency (spike frequency-dependent plasticity (SFDP)), all at low driving voltages (about 1 V).

The relevance of our study is that we demonstrate that IGTs can be employed as neuromorphic devices integrating memory (LTP) and processing functions (STP) in the same device, as a function of the electrical biasing conditions.

Work is in progress to address the effect of the structure of the transistor channel material on the correlation between applied bias conditions and response time, by extending our study to films of P3HT at different molecular weights, other organic semiconductors, and printable metal oxides.

## 4.7 Author Contributions

R.K.A. and C.S. designed the experiments. R.K.A. and T.L. performed the experiments. R.K.A. and C.S. wrote the manuscript. All authors commented on the manuscript.

## 4.8 Conflicts of interest

No conflicts to declare.

## 4.9 Acknowledgements

C.S. acknowledges NSERC (Discovery Grant) for financial support.

# CHAPTER 5 ARTICLE 2: EXPLORING RESPONSE TIME AND SYNAPTIC PLASTICITY IN P3HT ION-GATED TRANSISTORS FOR NEUROMORPHIC COMPUTING: IMPACT OF P3HT MOLECULAR WEIGHT AND FILM THICKNESS

## 5.1 Authors

Ramin Karimi Azari,*[a] Zhaojing Gao [a], Alexandre Carrière[a] and Clara Santato *[a]

Engineering Physics, Polytechnique Montreal, 2500 Ch. Polytechnique, Montréal, QC, H3T 1J4, Canada.

*Corresponding authors: ramin.karimi@polymtl.ca, clara.santato@polymtl.ca.

Name of journal: Journal of RSC Applied Interfaces

Date of publication: February 29, 2024

## 5.2 Abstract

Neuromorphic computers, inspired by the brain's neural networks, hold promise for efficient computation. Ion-gated transistors (IGTs), which employ ionic gating media, are particularly attractive for use in neuromorphic computing with remarkably low power consumption. This study focuses on IGTs utilizing organic polymer films of poly (3-hexylthiophene) (P3HT) as synaptic elements. The impact of P3HT molecular weight (MW, i.e. 24 kDa, 42 kDa, 92 kDa) and P3HT film thickness on IGT response time and synaptic behavior is investigated. Various synaptic behaviors are emulated, including paired-pulse facilitation (PPF) and spike number-dependent plasticity (SNDP). Additionally, the transition from short-term plasticity (STP) to long-term plasticity (LTP) is achieved by tuning MW, channel thickness, and gate-source voltage ($V_{gs}$) pulse parameters. These findings pave the way for P3HT-based IGTs as advanced artificial synaptic elements for neuromorphic computing.

## 5.3 Introduction

Transistors serve as fundamental components in von Neumann computers, acting as versatile electronic building blocks. Transistors primarily operate as switches, while also possessing the amplification capability for electric currents. This functionality enables them to either facilitate or impede the flow of current, thereby establishing a binary state for each transistor-akin to the representation of 1 or 0. In our brain, electrical signals exhibit more complexity than a simple binary code since synaptic connections embody various "weights" or strengths. [158, 159] Several synaptic devices have been built to imitate this, which has spurred the emergence of neuromorphic computers. These computers employ chip architectures that combine memory and processing within a single unit. This solution addresses the von Neumann architecture bottleneck and enables these systems to execute computations efficiently while consuming minimal power. Neuromorphic computers pave the way for novel approaches to computation that align with the parallel and distributed nature of biological neural networks. [160, 161]

Synaptic elements in neuromorphic structures have not yet fully harnessed the extensive functionality and dynamic nature observed in biological synapses. [162-164] This functionality, known as "synaptic plasticity", plays a critical role in neurons transmitting signals, memory, filtering, learning, and various other brain functions.[165-167] Therefore, it is crucial to create and produce biorealistic synaptic components that demonstrate strong functionality and display complex temporal and spatial dynamics. [168] The quest for a biorealistic artificial synapse that possesses excellent linearity, symmetry, collocated processing and memory capabilities, and low power requirements remains unresolved. [98]

To replicate these functions within a neuromorphic computer, extensive efforts have been directed toward the development of various devices. Among these devices, synaptic transistors based on organic films stand out as transistors functional for this purpose. [101, 169, 170] The structural properties of the organic films significantly influence its conductance and consequently, the output signal. [171]

By applying a voltage across the transistor, the organic film undergoes modifications that give rise to either depression or potentiation of the electric signal. This phenomenon closely resembles the activity spikes observed in the brain. Consequently, these changes can trigger a form of plasticity, wherein numerical information becomes encoded within the spikes. Parameters such as spike

frequency, timing, magnitude, and shape contribute to this encoding process. The conversion between binary values and spikes, and vice versa, remains an ongoing and dynamic field of research, with active investigations aimed at refining the precise methodologies involved in this conversion process. [172]

Synaptic Ion-Gated Transistors (IGTs) use ionic media to induce high carrier concentrations in the channel material, at low voltages. IGTs can emulate short-term and long-term plasticity, with low power consumption.

The ion gating effect is due to the redistribution of ions in the proximity of/within the channel. When a gate-source voltage ($V_{gs}$) is applied, initially ions from the ionic medium accumulate at the surface of the semiconducting channel, resulting in electrostatic doping (two-dimensional, 2D, doping). [93, 134-136] The possibility of ion penetration in the semiconducting channel material of IGTs is key to three-dimensional (3D) electrochemical doping. When ions can easily diffuse back into the ionic medium upon removal of $V_{gs}$, short-term plasticity (STP) occurs. Conversely, when ions are deeply intercalated within the channel material, they are not easily released after removing $V_{gs}$, leading to the emergence of long-term plasticity (LTP). In other words, the time scale of the synaptic activity is determined by the quality of ion incorporation, two or three-dimensional.[173, 174]

By changing the input $V_{gs}$ pulse parameters, such as duration, number, amplitude, and frequency, in addition to the structure and thickness of the transistor channel material, it is possible to modulate several synaptic functions through a two-step ion gating process and subsequent ion diffusive dynamics.

Synaptic IGTs exhibit advanced functionalities such as paired-pulse facilitation (PPF), spiking rate-dependent plasticity (SRDP), and dynamic filtering. These functionalities have highlighted the synaptic transistors' potential for the development of neuromorphic systems. [175]

In IGTs, the application of a $V_{gs}$ pulse leads to an initial increase in $I_{ds}$ (drain-source current), which then gradually returns to its original state. This decay time, known as the response time ($\tau$), is an important factor in the modulation of synaptic plasticity in IGTs. Indeed, $\tau$ shares similarities with the decay of the excitatory postsynaptic current (EPSC) observed in biological synapses. [176, 177]

The value of τ can be determined by calculating the time constant of the fitted exponential to the decay of $I_{ds}$ with time, following the removal of the $V_{gs}$ pulse. [178]

Regioregular Poly-3-hexylthiophene (RR P3HT) is a well-studied semiconducting polymer in organic electronics due to its high charge carrier mobility ranging from $10^{-5}$ to $10^{-1}$ $cm^2/Vs$ and commercial availability. [179-185]

The molecular weight (MW) of P3HT affects the morphology and structure of corresponding films. Atomic Force Microscopy (AFM) and X-Ray Diffraction (XRD) have been employed to shed light on such effect. AFM images show that films of P3HT with very low MW (ca. 5 kDa) have a rod-like structure whereas films of P3HT with intermediate MW (ca. 50 kDa) feature less ordered, isotropic nodule structure.[185] Complex chain entanglement in high MW P3HT leads to extended amorphous regions in corresponding films. [70, 72, 186, 187] This notion has been further validated by XRD measurements.[185, 188] Researchers have also explored structural and orientational changes in P3HT films along the film thickness using high-resolution Grazing Incidence X-ray Scattering (GIXS).

For P3HT films grown on $SiO_2$ substrates, small crystallite size and less oriented crystallites were observed at the P3HT/$SiO_2$ interface, with the overall degree of crystallinity found to increase with the increase of the film thickness (i.e. distance from the substrate surface). [189-192]

A detailed study of P3HT films with different MWs and thicknesses is crucial to establish structure/response relationships for their application in neuromorphic computing. Different MWs and thicknesses are expected to modify the molecular packing, orientation of the thiophene rings, degree of order, and nanoscale morphology of P3HT thin film. These factors are intimately tied to the ion permeability and charge carrier transport properties, thereby modulating the P3HT-based IGTs response time and synaptic behaviors.

Previous research on IGTs has reported τ ranging from microseconds to a few tens of milliseconds, depending on the specific device structure and operating conditions. [12, 147, 157] In this work, we report on the response time and synaptic behavior of IGTs based on spin-coated P3HT films as channel material with different MWs, i.e. low (24 kDa), intermediate (42 kDa), and high (92 kDa), and thickness (obtained by changing the spin coating speed from 500 rpm to 4000 rpm). The ionic

medium was the ionic liquid 1-ethyl-3-methylimidazolium bis(trifluoromethylsulfonyl) imide, [EMIM][TFSI] (Figure 5.1a). After conducting transistor electrical characterizations, we studied various synaptic behaviors of bio-inspired synaptic [EMIM][TFSI]-gated P3HT transistors, such

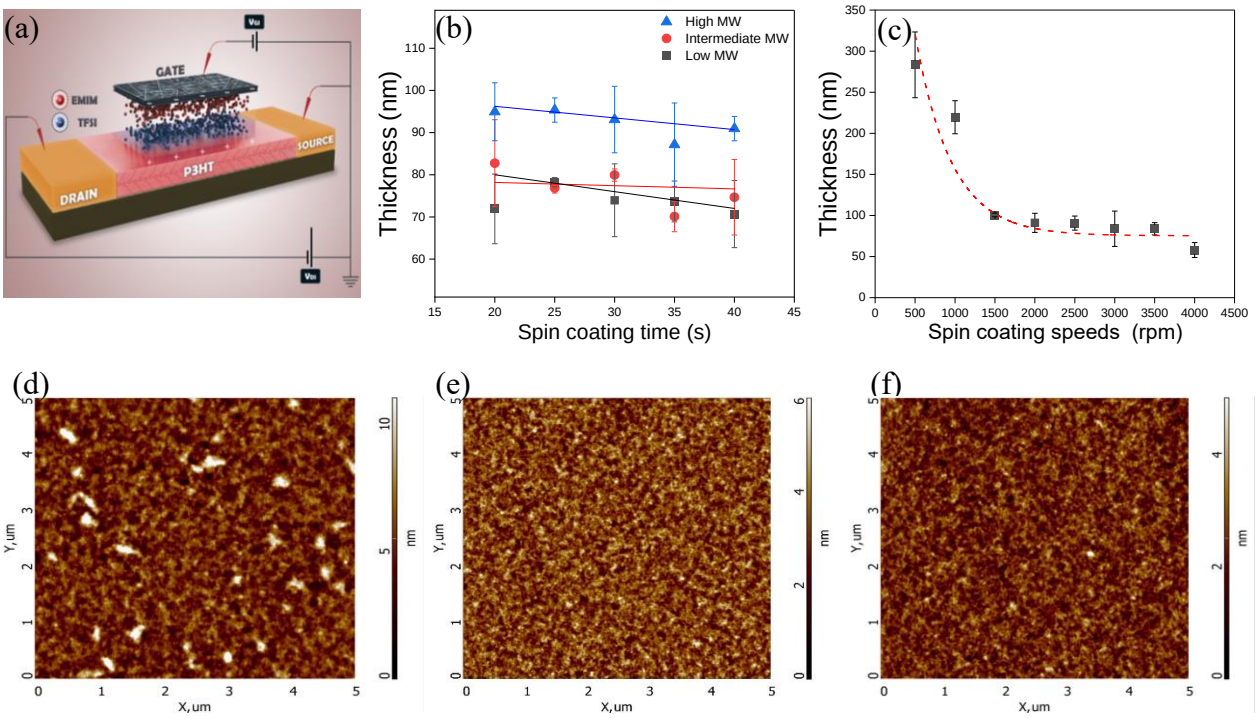


Figure 5.1 P3HT-based IGT device structure. Thickness of P3HT films deposited with: b) different MWs at five spin coating times (20, 25, 30, 35, and 40 s, at 1000 rpm), c) different spin coating speeds (lines are fittings) at 30 s and with MW 50-70 kDa. AFM images of P3HT films, spin coated during 30 s on $SiO_2$/Si, at 1000 rpm, d) low MW e) intermediate MW f) high MW. Image size is 5 μm×5 μm.

as response time, STP-to-LTP transition, spike number-dependent plasticity (SNDP) and pair-pulse facilitation (PPF) as a function of the MW, thickness, $V_{gs}$ pulses parameters, and drain-source voltage ($V_{ds}$).

## 5.4 Results and discussion

To study the effect of MW and thickness of P3HT thin films on the response time and synaptic behavior of IGTs, we spin coated P3HT films on $SiO_2$/Si using different P3HT MWs (namely low

(24 kDa), intermediate (42 kDa), and high (92 kDa)), different spin coating times from 20 to 40 s and different rotation speeds (500 rpm, 1000 rpm, 2000 rpm, 4000 rpm). We observe a difference in thickness among various MWs P3HT films and spin coating times (Figure 5.1b).

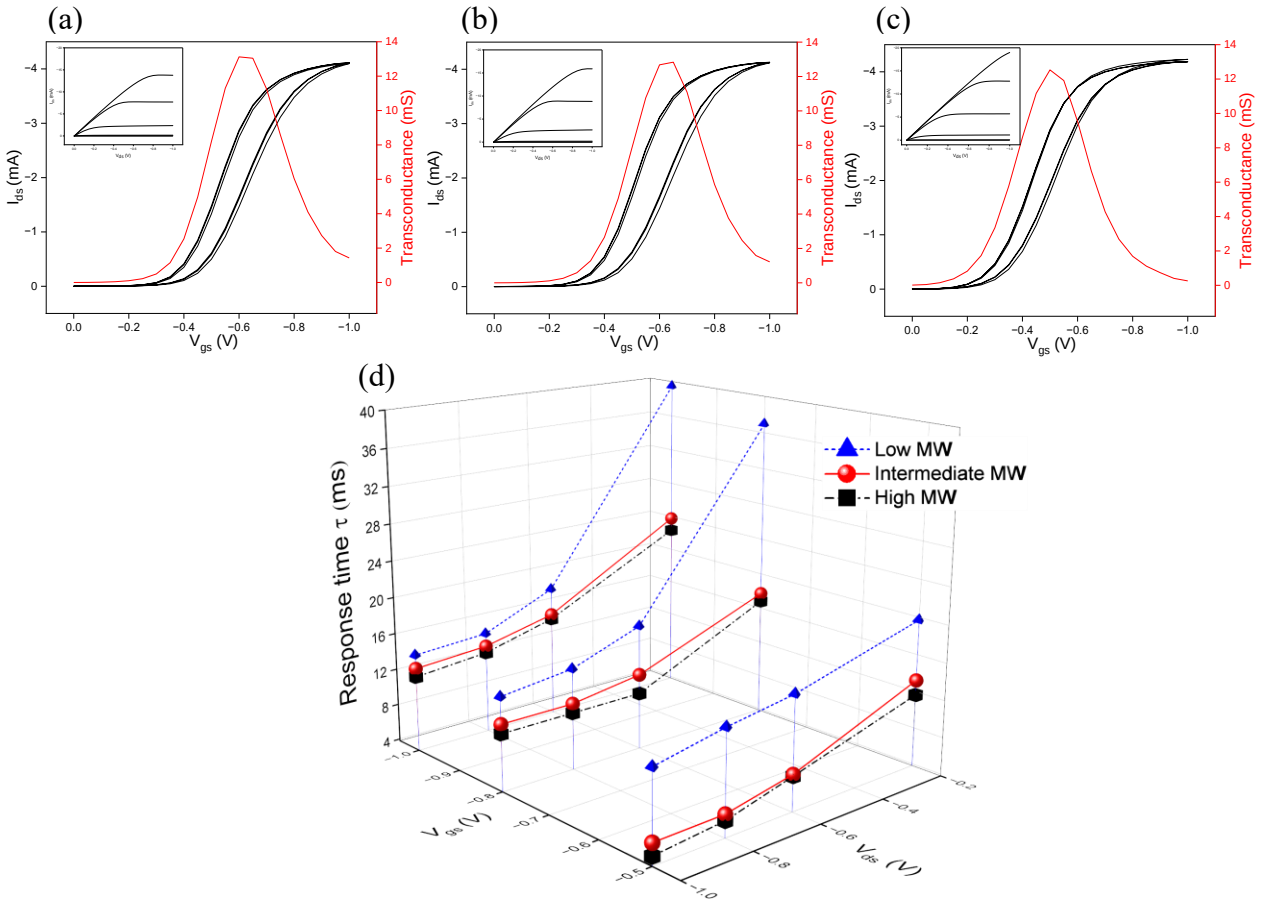


Figure 5.2 Transfer characteristics (black line) in the linear regime ($V_{ds}$ = -0.2 V, (3 cycles)) at $V_{gs}$ scan rate 50 m V $s^{-1}$ (inset: output characteristic with $V_{gs}$ = 0, -0.2, -0.4, -0.6, -0.8, -1 V at $V_{ds}$ 50 m V $s^{-1}$ scan rate) and transconductance curve (red line) for [EMIM][TFSI]-gated transistors based on a) High MW b) Intermediate MW c) Low MW P3HT deposited at 1000 rpm during 30 s. d) Transient response of an [EMIM] [TFSI]-gated P3HT transistor with high, intermediate, and low MW for $V_{gs}$ = -1, -0.8, and -0.5 V at different $V_{ds}$. The duration time of the $V_{gs}$ bias is 200 ms.

Increasing the spin-coating speed, we observe a decrease of the P3HT film thickness (Figure 5.1c). AFM images of P3HT films (Figure 5.1d, e, f) reveal that the root mean square (rms) roughness of

the surface decreases with an increase in the molecular weight (MW) of P3HT, i.e. 2.2 ± 0.6 nm for low MW, 0.8 ± 0.1 nm for intermediate MW, and 0.60 ± 0.03 nm for high MW P3HT, for a spin-coating time of 30 s at 1000 rpm. In other words, the increase in the P3HT molecular weight is associated with an increase in the smoothness of the film surface, most likely due to an increase in the short-range order within the molecular weight. [70, 72, 186, 187]

### 5.4.1 Effect of different P3HT MWs on response time and synaptic behavior of P3HT IGTs

**Transfer and output characteristics of [EMIM][TFSI]-gated P3HT IGTs**

Transfer and output characteristics show a typical p-type behavior of devices working in accumulation mode. $I_{ds}$ increases with the decrease of $V_{gs}$ scan rate from 100 to 25 m V $s^{-1}$ due to the increased time available to accommodate the redistribution of the ions (Figure B.1 and B.2). Further, $I_{ds}$ increases with the decrease of MW (Figure 5.2a-c) and the increase of the channel thickness (as determined by the spin coating conditions) (Figure 5.4a-d and 1c).

Devices fabricated using high MW P3HT exhibit a higher transconductance ($g_m = \delta I_{ds}/\delta V_{gs}$, a transistor parameter that describes how $I_{ds}$ responds to variations in $V_{gs}$ [93, 193]) than for low MW counterparts, attributable to higher ionic permeability. [72, 194, 195] The increased transconductance implies that even a slight change in $V_{gs}$ can result in a substantial variation in $I_{ds}$, rendering high-MW P3HT IGTs more sensitive to changes in $V_{gs}$ compared to lower MWs counterparts.

**Effect of $V_{gs}$ and $V_{ds}$ amplitudes on P3HT IGT response time, for different P3HT MWs**

We studied the excitatory postsynaptic current (EPSC) response upon applying a 200 ms square step $V_{gs}$ pulse with amplitudes of -0.5, -0.8, and -1 V, at $V_{ds}$ = -0.2, -0.6, -0.8, and -1 V (Figure 5.2d). Low amplitude $V_{gs}$ pre-synaptic pulses are expected to dope regions in the P3HT films close to the film's surface and/or featuring short-range order (amorphous). **[186]** These regions can rapidly de-dope, resulting in the rapid decay of the postsynaptic current (PSC). This response is analogous to STP. We notice that $\tau$ increases with the increase of $V_{gs}$ for all P3HT MWs considered. Higher values of $V_{gs}$ are expected to induce a deeper ion penetration in the films. This implies longer times for ions' removal prior to reaching the steady state, after the removal of $V_{gs}$ (LTP).

Further, in agreement with Bernards' model, [193] we observed that the increase of $V_{ds}$ causes the decrease of τ.

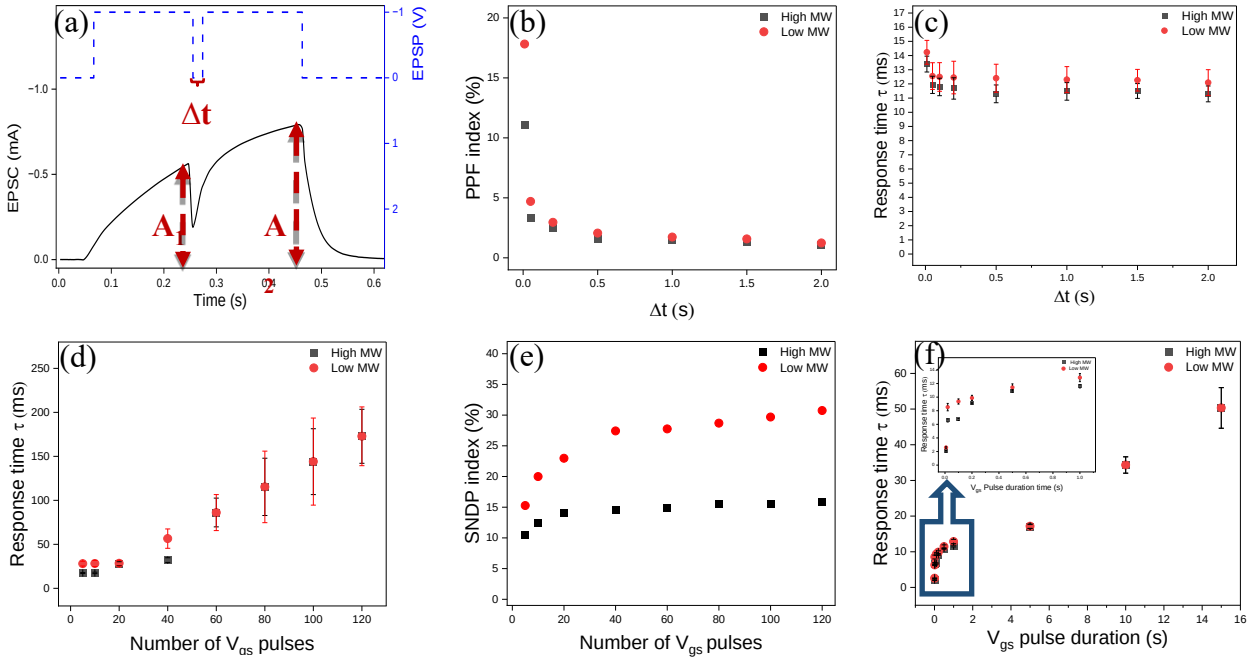


Figure 5.3 Synaptic behavior of artificial synapses based on P3HT IGTs for different P3HT MWs. a) $I_{ds}$ triggered by a pair of successive presynaptic $V_{gs}$ (-1 V) pulses with a pulse interval Δt. A1 and A2 are the amplitudes of $I_{ds}$. b) PPF index as a function of pulse interval of two consecutive $V_{gs}$ pulses, Δt = 10 ms to 2 s. Response time of second $I_{ds}$ pulses after applying two consecutive $V_{gs}$ pulses versus time interval of pulses, Δt. d) Response time of P3HT IGT versus different numbers of $V_{gs}$ square step train pulses, from 5 to 120 pulses. $V_{gs}$ = -1 V and $V_{ds}$ = -0.6 V. e) SNDP index as a function of the number of $V_{gs}$ pulses. f) Response time of IGT versus $V_{gs}$ pulse duration for low and high MW P3HT.

The response time increases with decreasing MW of P3HT, for $V_{gs}$ = -0.5, -0.8, and -1 V (Figure 5.2d). For instance, for pre-synaptic spikes with 200 ms pulse width, $V_{gs}$ = -1 V and $V_{ds}$ = -0.2, τ increases from 22.3 to 39.5 ms, i.e. by 77%, with decreasing MW. The increase of MW brings about an increase in the entanglement of the P3HT chains, paralleled by an increase in the short-range ordered portion of the films. [70, 72, 196] This is expected to promote ion permeability, i.e.,

facilitate P3HT doping/de-doping.

**Impact of different MWs on IGT synaptic behaviors**

Paired pulse facilitation (PPF) is the rate of enhancement in the EPSC amplitude after the second of two repetitive excitatory postsynaptic potentials (EPSPs). In PPF, two EPSC peaks ($A_1$ and $A_2$) are triggered, with the latter larger than the former, with $PPF = (A_2 - A_1) / A_1 \times 100\%$. In our experiments, we used $V_{gs}$ = -1 V, $V_{ds}$ = -0.6 V, with an interval $\Delta t$ (Figure 5.3a). Figure 5.3b shows PPF as a function of $\Delta t$ and P3HT MW. The highest PPF value is observed at $\Delta t$ = 10 ms. With $\Delta t$ increasing gradually, the PPF index value decreases rapidly. The mechanism governing the PPF process can be explained as follows. During the first $V_{gs}$ spike, TFSI anions move towards the surface of the P3HT films; a fraction of these anions move beneath the film surface, within film depth. When the second $V_{gs}$ spike is applied, shortly after the first one ($\Delta t < 100$ ms), the movement of the anions triggered by the first $V_{gs}$ spike is still partially present such that the effects of $A_1$ and $A_2$ sum up. Consequently, the magnitude of $A_2$ EPSC is larger than that of $A_1$. For $\Delta t > 100$ ms, anions have the time to reach the equilibrium state to the extent that the summation effect disappears.

Increasing the degree of order (i.e. increasing the roughness) in the semiconducting channel by decreasing the P3HT MW brings about limited ion permeability over an extended lapse of time. A higher quantity of ions contributes to an elevated PPF index (Figure 5.3b). The summation effect causes an increase in the IGT response time (Figure 5.3c).

**IGT response time as influenced by the number of $V_{gs}$ pulses and P3HT MW**

In order to investigate the synaptic properties of [EMIM][TFSI]-gated P3HT transistors, we applied a series of $V_{gs}$ pulses (5, 10, 20, 40, 60, 80, 100, 120 pulses). We observed a transition in the device behavior from short-term plasticity (STP) to long-term plasticity (LTP) with increasing number of pulses. Such transition is commonly regarded as the foundation for learning and memory in the human brain. We replicate LTP in P3HT IGTs by applying a series of consecutive $V_{gs}$ pulses (-1 V, 200 ms) with a 200 ms interval while maintaining $V_{ds}$ = -0.6. This sequence of $V_{gs}$ pulses effectively facilitates the permeation of ions in the P3HT films bringing about an increase in $I_{ds}$ associated with the modulation of the channel conductivity. Factors such as the increase of the

P3HT MW, with an associated increase of the amorphous portion of the channel material and channel permeability, play a role. $SNDP_{1\text{-}n} = (A_n - A_1) / A_1 \times 100\%$ (SNDP index) increases as the number of pulses increases (ranging from 5 to 120, Figure 5.3e). For Low MW P3HT, the SNDP

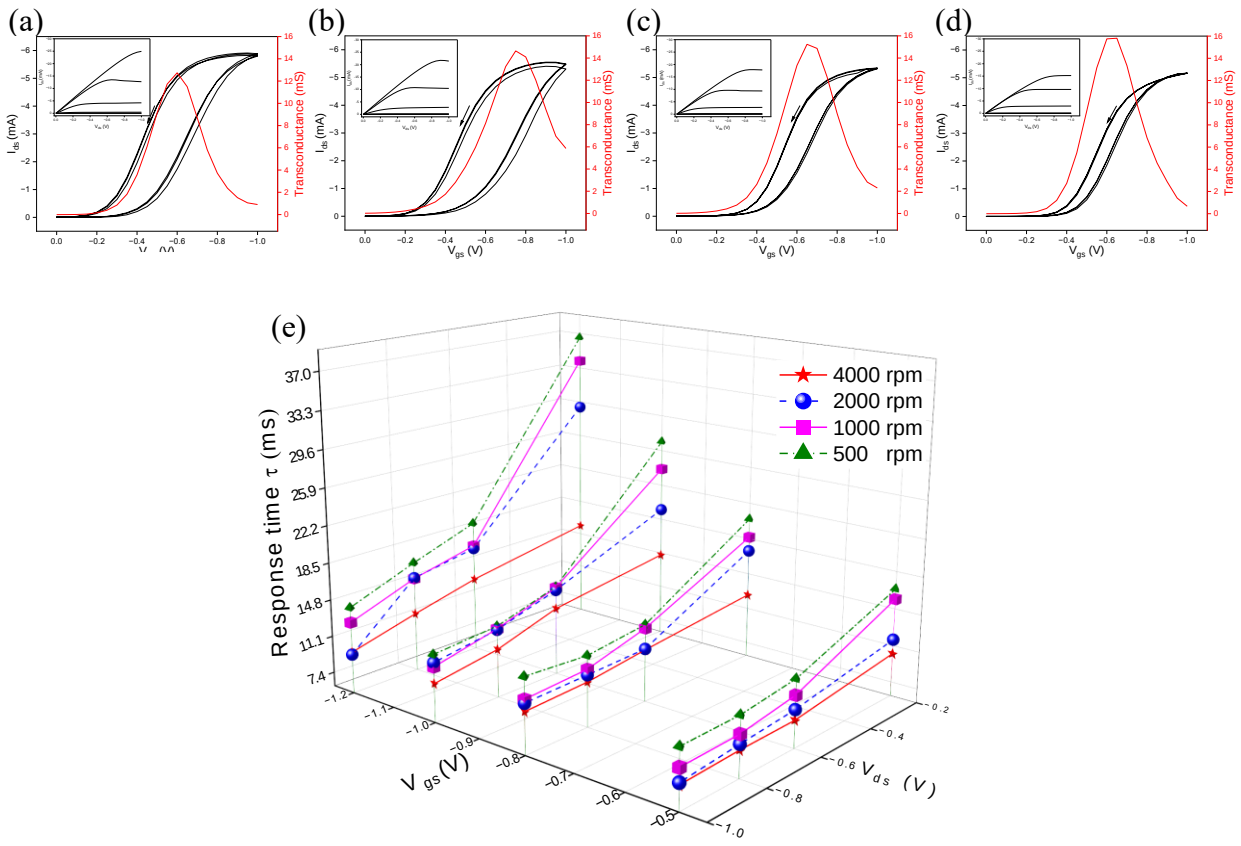


Figure 5.4 Transfer characteristics in the linear regime ($V_{ds}$ = -0.2 V (3 cycles)) at $V_{gs}$ 50 m V $s^{-1}$ scan rate (inset: output characteristic with $V_{gs}$ = 0, -0.2, -0.4, -0.6, -0.8, -1 V and $V_{ds}$ 50 m V $s^{-1}$ scan rate) and transconductance curve for [EMIM][TFSI]-gated P3HT transistors prepared with spin coating rate a) 500 rpm b) 1000 rpm c) 2000 rpm d) 4000 rpm, on 30 seconds with intermediate MW. e) Transient response of [EMIM][TFSI]-gated P3HT transistors with intermediate MW with $V_{gs}$ = -1.2, -1, -0.8, and -0.5 V, at different $V_{ds}$. The duration of the $V_{gs}$ bias is 200 ms.

index for n = 120 is about 30% while for high MW P3HT, it is 15%. This finding indicates that the transition from STP to LTP in low MW P3HT-IGTs is twice that of high MW P3HT-IGTs.

With the increase of n, there is an increase in ion redistribution time, paralleled by an increase of τ. We observed a significant impact of P3HT MW on the IGT response time when a low number of pulses was applied. However, as the number of pulses increased, τ of different P3HT MWs became nearly identical (Figure 5.3d).

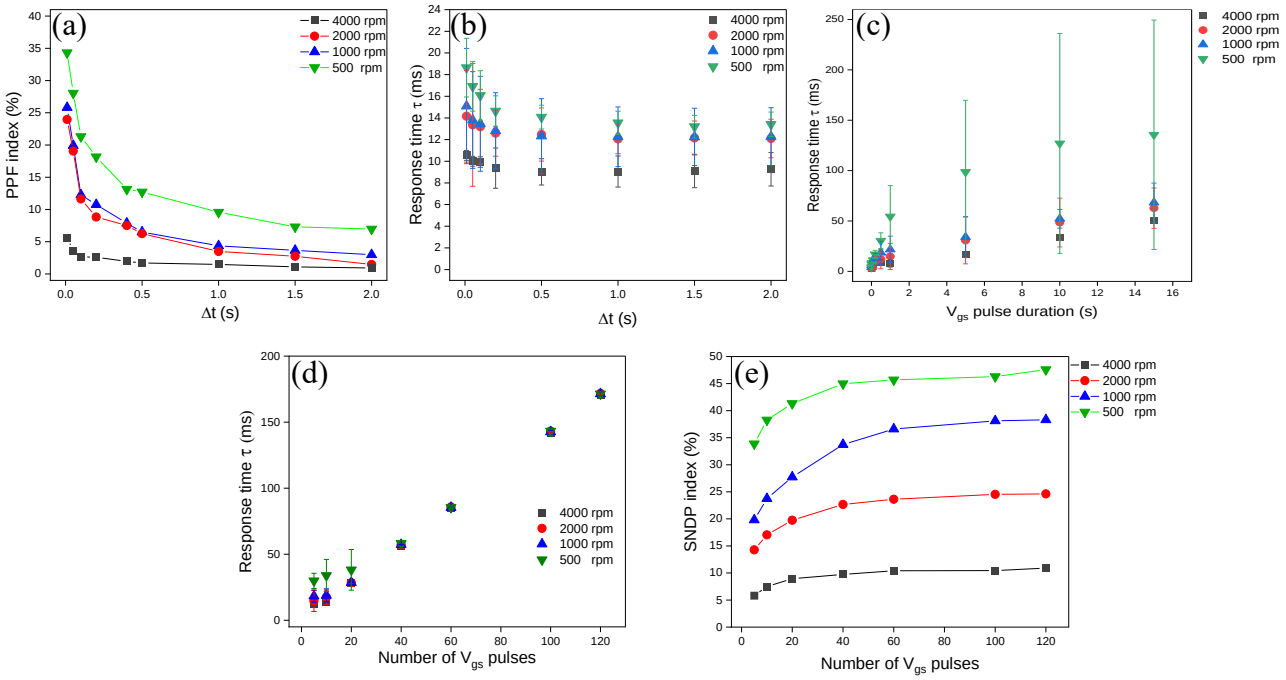


Figure 5.5 Synaptic behavior of artificial synapses based on P3HT IGTs for films spin coated at different speeds (in turn associated with thicknesses, Figure 5.1, c). a) PPF index as a function of pulse interval of two consecutive $V_{gs}$ pulses (Δt from 10 ms to 2 s). b) Response time of second $I_{ds}$ pulses after applying two consecutive $V_{gs}$ pulses versus time interval of pulses (Δt). c) Response time of IGTs versus $V_{gs}$ pulse duration. d) Response time of P3HT IGTs versus different numbers of $V_{gs}$ square step train pulses, from 5 to 120 pulses. $V_{gs}$=-1 V and $V_{ds}$=-0.6 V. e) SNDP index $(A_n - A_1)/A_1 \times 100\%$), with n = the number of $V_{gs}$ pulses, as a function of the number of $V_{gs}$ pulses.

**Impact of MW and pulse duration on IGT response time**

A longer pulse duration provides more time for ions to penetrate the channel, resulting in an extended de-doping time. Consequently, upon $V_{gs}$ removal, τ increases. For pulse durations lower

than 1 s, decreasing the MW of P3HT causes higher values of τ; for durations longer than 1 s, τ is similar for high and low MW P3HT IGTs (Figure 5.3f).

### 5.4.2 Impact of film thickness (as controlled by spin coating conditions) on response time and synaptic behavior in P3HT IGTs

IGT transfer ($V_{gs}$ scan rate 100, 50 and 25 m V $s^{-1}$, and $V_{ds}$ = -0.2 V) and output characteristics ($V_{ds}$ scan rate 100, 50 and 25 m V $s^{-1}$, and $V_{gs}$ = 0 to -1 V) show that $I_{ds}$ decreases with the increase of the spin coating speed (thinner P3HT film) (Figures 5.4a-d, Figures B.2a-l and Figure 5.1c). The higher permeability of thinner P3HT channels due to the lower degree of order brings about higher transconductance, i.e. an enhanced IGT sensitivity to changes in $V_{gs}$. [16, 185, 189, 196]

We investigated the response time of P3HT IGTs by employing a square $V_{gs}$ pulse with a width of 200 ms and varied amplitudes of -0.5, -0.8, -1, and -1.2 V. The measurements were performed at different $V_{ds}$ of -0.2, -0.6, -8, and -1 V (Figure 5.4e). Additionally, we examined the impact of different channel thicknesses (as determined by the spin coating rates used for P3HT films' deposition) on τ. The increase of τ with the increase of $V_{gs}$ and the decrease of τ with the increase of $V_{ds}$ are clear for all spin coating speeds. Further, τ increases with the decrease of the spin coating speed from 4000 to 500 rpm (Figure 5.4e). The increased order of P3HT obtained by decreasing spin coating speed decreases the permeability of ions into the channel and increases the ion redistribution time or IGT response time. We can also explain the observed result through the Bernards' model. [178]

Figure 5.5a shows increasing film thickness can enhance the pair pulse facilitation. Slow ion diffusion in a thick channel affects pair pulse facilitation, possibly leading to longer facilitation times (Figure 5.5b). With thick films, the channel can store more charge upon the first pulse, leading to more pronounced facilitation during the second pulse.

Figure 5.5c and 5.5d show that the increase of the $V_{gs}$ pulse duration time and number of pulses can have the same effect on the synaptic behavior of P3HT IGTs with different channel thicknesses (obtained by controlling the spin coating conditions as detailed in Figure 5.1c). By increasing the number of pulses and $V_{gs}$ pulse duration, we can increase τ, which can be interpreted as the

redistribution time of the ions, upon $V_{gs}$ removal. Increasing the thickness (going from a spin coating speed of 4000 rpm to 500 rpm, Figure 5.1c) results in an increase in τ for all $V_{gs}$ pulse duration times and pulse numbers (Figures 5.5c and 5.5d).

Further, we can observe a stronger transition from STP to LTP, in a thicker P3HT film. We observed that $SNDP_{1\text{-}120}$ (where $SNDP_{1\text{-}n} = (A_n - A_1)/A_1 \times 100\%$) is 48% for thick channel films (500 rpm) and 11% for thin films (4000 rpm). These values quantitatively describe the evolution of the SNDP index with the thickness of the P3HT films (Figure 5.5e and 5.1e).

## 5.5 Experimental

### 5.5.1 Microfabrication

Photolithography for electrode patterning was performed on 200±10 nm-thick $SiO_2$ on 525±25 µm-thick doped silicon wafer purchased from WaferPro, San Jose, California. Au/Ti electrodes (40 nm/5 nm) had a width (W) of 4 mm and an interelectrode distance (L) of 10 µm. The patterned substrates were cleaned with a sequential ultrasonic bath in isopropanol alcohol (IPA) for 10 min, acetone for 10 min and IPA for 10 min, prior to the deposition of the P3HT thin films.

### 5.5.2 P3HT films deposition

P3HT solutions consisting of 10 mg regioregular P3HT (RIEKE Metals) with different molecular weights, low (24 kDa), intermediate (42 kDa), and high (92 kDa), in 1 ml chlorobenzene were stirred overnight in an $N_2$ glove box ($O_2$ < 5 ppm, $H_2O$ < 5 ppm). P3HT films were deposited by 30 seconds spin coating at 1000 rpm on the $SiO_2$/Si substrates. In order to control the thickness of the films, P3HT with MW 50-70 kDa were spin coated for 30 seconds at various rotation speeds: 500, 1000, 2000, and 4000 rpm. All devices were thermally treated on a hotplate at 100 °C for 2 h in the $N_2$ glovebox. The ionic liquid used as the gating medium, [EMIM][TFSI], purchased from IoLiTec (> 99%), was purified under vacuum (ca. $10^{-5}$ Torr) for 24 h at 60 °C before use. [EMIM][TFSI] was dropped onto the DuraporeR membrane (4 mm×9 mm-sized, 125 µm-thick). The membrane was positioned in correspondence with the transistor channel. Large surface area carbon paper (Spectracarb 2050, 170 µm-thick), coated with an ink comprising activated carbon (PICACTIF SUPERCAP BP10, Pica, 28 mg $ml^{-1}$) and polyvinylidene fluoride (PVDF, KYNAR

HSV900, 1.4 mg $ml^{-1}$) binder in N-methyl pyrrolidone (NMP, Fluka) was utilized as the gate electrode (6 mm×3 mm-sized).

### 5.5.3 Characterization of the channel material

The thickness of P3HT thin films were measured by Dektak 150 Profilometer. To obtain the thin film height, the probe physically moved along the surface during the measurement. The topography of the samples was probed by atomic force microscopy (AFM), in ambient conditions, with an NT-MDT NTEGRA II microscope. The images were acquired in semi-contact (tapping) mode with an NSG10 cantilever (a length of 95 um, a width of 30 um, resonant frequency of 240 kHz and force constant of 11.8 N/m).

### 5.5.4 Electrical characterization of the devices

Transistor characterization was conducted using a semiconductor parameter analyzer, Agilent B1500A, and a house-made micromanipulated electrical probe station inside the $N_2$ glove box.

## 5.6 Conclusions

In conclusion, we conducted a comprehensive study of the properties and performance of synaptic P3HT ion-gated transistors (IGTs). We examined the effect of P3HT molecular weight (MW) on morphology, transistor device characteristics, response time, and synaptic behavior of IGTs fabricated with low (24 kDa), intermediate (42 kDa), and high (92 kDa) MW. Low MW P3HT films, exhibiting a higher degree of order, expected to be associated to lower ion permeability with respect to intermediate and high MW P3HT films, bringing about corresponding devices with lower transconductance. Further, low MW P3HT IGTs exhibit longer response times upon application of $V_{gs}$ pulses concerning counterparts making use of intermediate and high MW.

We emulated several essential synaptic functions, including PPF and SNDP, and realized a transition from STP to LTP by tuning $V_{gs}$ pulses' parameters, such as amplitude, duration, and pulses' number, in low, intermediate, and high MW P3HT-IGTs. In all cases, devices with low MW P3HT have more effective STP-to-LTP transition than medium and high MW counterparts.

The study of the dependence of response time and synaptic behavior on film thickness in P3HT-based IGTs revealed that films deposited with lower spin coating speeds (thicker films, more ordered films) feature lower transconductance. Our study demonstrates a significant increase in the response time of IGTs with an increasing thickness of the P3HT film. Moreover, increasing film thickness brings about an improvement in synaptic behavior, encompassing PPF and SNDP. The transition from STP to LTP is achieved by controlling the thickness of the films. Thicker P3HT films bring about higher levels of LTP.

In perspective, we plan to explore the development of organic synaptic phototransistors exposed to light pulses, to finely tune and modulate synaptic behaviors.

## 5.7 Author Contributions

R.K.A. and C.S. designed the experiments. R.K.A. and Z.G. performed the transistor and time-resolved characterizations. R.K.A and A.C. performed AFM experiments. R.K.A., Z.G. and C.S. drafted the manuscript. All authors commented on the manuscript.

## 5.8 Conflicts of interest

There are no conflicts to declare.

## 5.9 Acknowledgements

C.S. acknowledges NSERC (Discovery Grant) for financial support.

# CHAPTER 6 ARTICLE 3: EMULATION OF SYNAPTIC PLASTICITY IN $WO_3$-BASED ION-GATED TRANSISTORS

## 6.1 Authors

Ramin Karimi Azari[a]*, Luan Pereira Camargo[a,b], José Ramón Herrera Garza[a], Liam Collins[c], Wan-Yu Tsai[c], Lariel Chagas da Silva Neres[a,d], Patrick Dang[a], Martin Schwellberger Barbosa[e], Clara Santato [a]*

*Corresponding authors: ramin.karimi@polymtl.ca, clara.santato@polymtl.ca

[a] Engineering Physics, Polytechnique Montreal, 2500 Ch. Polytechnique, Montréal, QC, H3T 1J4, Canada.

[b] Department of Chemistry, State University of Londrina (UEL), 86057-970, Londrina, PR, Brazil.

[c] Oak Ridge National Laboratory, 1 Bethel Valley Road, Oak Ridge, TN 37830, USA

[d] Institute of Chemistry, State University of São Paulo (UNESP), 14801-970 Araraquara, SP, Brazil

[e] Institute of Chemistry, Federal University of Goiás (UFG), Goiânia - GO, 74690-900, Brazil.

Name of journal: Advanced Electronic Materials

Date of submission: October 22, 2024

## 6.2 Keywords

synaptic transistors, $WO_3$ films, ion gating media, synaptic plasticity, ion intercalation, ion gated transistors, neuromorphic computing

## 6.3 Abstract

Neuromorphic systems, inspired by the human brain, promise significant advancements in computational efficiency and power consumption by integrating processing and memory functions, thereby addressing the von Neumann bottleneck. This paper explores the synaptic plasticity of a $WO_3$-based ion-gated transistor (IGT) in [EMIM][TFSI] and a 0.1 mol $L^{-1}$ LiTFSI in [EMIM][TFSI] for neuromorphic computing applications.

Cyclic voltammetry (CV), transistor characteristics, and atomic force microscopy (AFM) force-distance (FD) profiling analyses reveal that $Li^+$ brings about ion intercalation, together with higher mobility and conductance, and slower response time ($\tau$). $WO_3$ IGTs exhibit spike amplitude-dependent plasticity (SADP), spike number-dependent plasticity (SNDP), spike duration-dependent plasticity (SDDP), frequency-dependent plasticity (FDP) and paired-pulse facilitation (PPF), which are all crucial for mimicking biological synaptic functions and understanding how to achieve different types of plasticity in the same IGT.

Our findings underscore the importance of selecting the appropriate ionic medium to optimize the performance of synaptic transistors, enabling the development of neuromorphic systems capable of adaptive learning and real-time processing, which are essential for applications in artificial intelligence (AI).

## 6.4 Introduction

Neuromorphic computation, inspired by the human brain's parallel processing, integrates both data handling and decision-making in a single location, in contrast to von Neumann architecture's separate memory and processor setup. This integration aims to enable more efficient, real-time processing and learning, marking a significant step forward in computing technology. [197-199]

Neuromorphic computation not only streamlines processing but also consumes far less power than conventional systems for data transmission and processing. This is due to its brain-like architecture, which naturally consumes less power (the human brain is incredibly power-efficient, using roughly 20 watts), making it a more sustainable alternative in the computing world compared to modern supercomputers, which require around 28 megawatts.[200-203] Biomimetic architectures, such as neuromorphic systems, are essential for advancing artificial intelligence by adopting spiking neural networks (SNNs), enabling them to learn and process information in a manner similar to the human brain.[204] They enhance AI performance and capability, supporting complex tasks like pattern recognition and sensory data interpretation while enabling simultaneous storage and processing in a single device. [201, 205, 206]

Over the past few years, there has been considerable progress in developing synaptic devices that imitate brain functions, specifically in learning and memory. These devices aim to replicate the

fundamental ability of synapses to adjust the strength of neural connections (i.e., synaptic plasticity)—a key mechanism in memory formation—and significant progress has been made in studying artificial synapses and simulating biological neurons.[201]

There are mainly two types of devices that can replicate the idea of connecting two neurons through a synapse: two-terminal devices, known as memristors, and three-terminal devices, known as transistors. [207-209] These devices can control output current based on their design and the material used, functioning as either a digital switch, abruptly altering the conductance of the channel, or as an analog switch, gradually adjusting the channel's conductance.[210]

One of the synaptic devices capable of demonstrating both memory and processing simultaneously is the ion-gated transistor. [175] Synaptic IGTs with three terminals and ionic liquid (IL) gating have been suggested as a promising method to mimic biological synapses. Recently, a variety of materials, including organic compounds, metal oxides (MO), carbon-based nanomaterials, single crystals, and two-dimensional materials have been investigated for their potential use in these synaptic IGTs. [98] Through this design, the modulation of channel conductance can be achieved with greater efficiency. [209-213]

In an IGT artificial synapse, the channel conductance represents the synaptic weight of a biological synapse. Channel conductance or plasticity can vary based on several factors, including input pulse amplitude (spike amplitude-dependent plasticity, SADP), duration (spike duration-dependent plasticity, SDDP), interval (frequency-dependent plasticity, FDP), number of spikes (spike number-dependent plasticity, SNDP), and paired-pulse facilitation (PPF). This behavior is analogous to how the excitatory postsynaptic current (EPSC) in biological synapses changes in response to variations in presynaptic pulse activity.[214] This property allows the artificial synapse to mimic both short-term (STP) and long-term plasticity (LTP), along with learning and forgetting mechanisms of biological synapses. [213, 215]

Tungsten trioxide ($WO_3$), an *n*-type metal oxide with a band gap of approximately 2.5 eV, is recognized by its applications in electrochromism, sensing, photocatalysis, and photoelectrochemistry. These applications typically benefit from high surface area mesoporous nanostructures, which facilitate the permeation of ionic media.[216, 217] Extensive research is being conducted on metal-oxide thin film-based IGTs, which have broad application in areas such

as energy conversion and storage devices, low-power wearable electronics and bioelectronics, light-emitting diodes, and neuromorphic computing.[87, 218-220]

The high surface area of the channel in IGTs that employ mesoporous nanostructured $WO_3$ thin films is expected to enhance the degree of doping. The doping mechanism may include not only two-dimensional electrostatic and conventional three-dimensional electrochemical faradaic doping, which involves the insertion and de-insertion of ions in the oxide lattice, but also a nonconventional form of electrochemical doping. This latter form, confined at the interface between the IL and the metal oxide, is especially relevant for ILs composed of relatively large ions that may not be able to insert into the oxide lattice.[193]

The diffusion barrier encountered by $Li^+$ in $WO_3$ is notably low, attributable to the diminutive size of the $Li^+$. This characteristic makes $Li^+$ a promising dopant for $WO_3$ IGTs. The intercalation and deintercalation of $Li^+$ in a mixed conductor channel could improve $WO_3$ IGT plasticity performance.[221, 222]

Among the diverse range of synaptic devices, IGT transistors based on $WO_3$ have emerged as a promising candidate for the development of hardware neural networks specifically designed for analog computing in neuromorphic applications.[223-225]

However, certain fundamental attributes observed in biological synapses, such as spontaneous decay indicative of forgetting behavior, SADP, SNDP, SDDP, FDP, PPF and the transition from STP to LTP have not yet been reported in a $WO_3$-based IGT.[226]

The structure of the electric double layer (EDL) at the interface between the IL and the IGT channel can be studied by AFM FD profiling. This technique measures the force between the AFM probe tip and the ionic layering of the interface, as the tip moves vertically. The ionic layering at various spots on the channel film surface can be measured *in operando* (in transistor operation) by observing the patterns created on FD curves.

In this work, we report on mesoporous nanostructured $WO_3$ thin film-based IGTs using different ion gating media, specifically ILs [EMIM][TFSI] and 0.1 mol $L^{-1}$ LiTFSI in [EMIM][TFSI]. Following $WO_3$ film fabrication and device assembly, we conducted electrochemical characterization of the $WO_3$ films through cyclic voltammetry, complemented by in operando AFM

FD characterization of the EDL at the interface between the ion gating medium and $WO_3$ film. This comprehensive approach allowed us to effectively evaluate the synaptic performance of the $WO_3$-based IGTs. Our findings indicate the potential of doping $WO_3$ channels with various cations for the hardware implementation of artificial synapses in analog computing and memory applications.

## 6.5 Results and discussion

### 6.5.1 Material Characterizations

$WO_3$ films with a thickness of 200 nm were deposited on $SiO_2$ substrates using spin coating. AFM topography images of $WO_3$ films deposited on $SiO_2$ substrates (Figure 6.1a-d) reveal a surface composed of small particles. The root mean square (rms) roughness is estimated to be approximately 3.0 ± 0.4 nm, as depicted in the height profile.

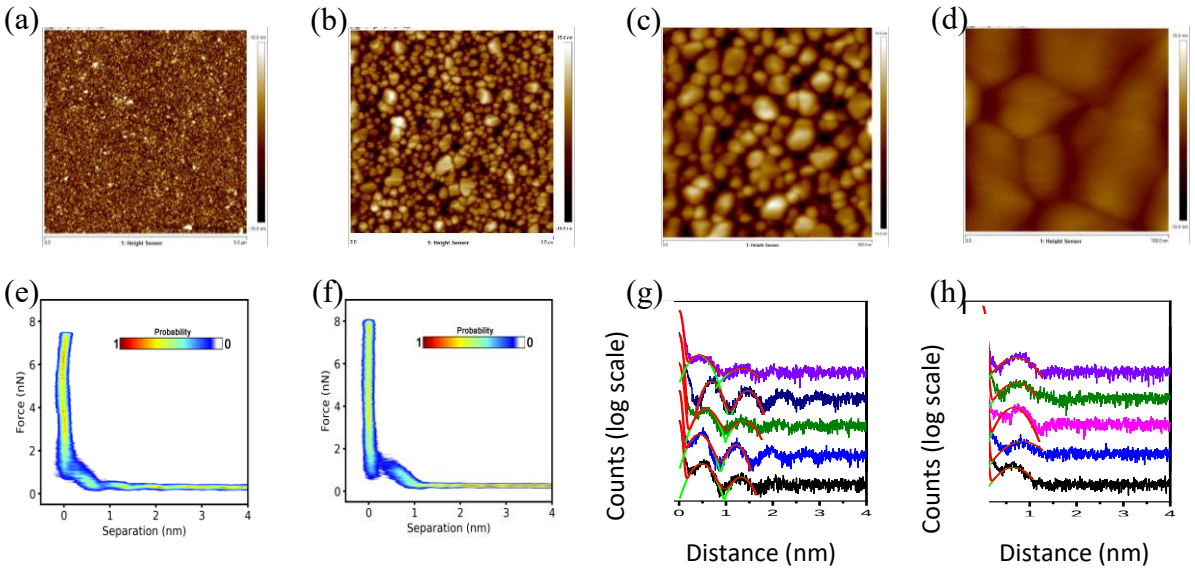


Figure 6.1 AFM height images of $WO_3$ films with size: a) 5 µm × 5 µm, b) 1 µm × 1 µm, c) 500 nm × 500 nm, d) 100 nm × 100 nm. 2D force-separation histogram from IL/$WO_3$ interface for $WO_3$ IGT based on e) [EMIM][TFSI] f) 0.1 mol $L^{-1}$ LiTFSI in [EMIM][TFSI]. Separation histogram with Gaussian fitting g) for the peaks of five different spots in a $WO_3$ IGT with [EMIM][TFSI] h) for the peaks of 5 different spots in a $WO_3$ IGT with 0.1 mol $L^{-1}$ LiTFSI in [EMIM][TFSI] gating material.

The scanning electron microscopy (SEM) images (Figure 6.2a, b) of the spin-coated $WO_3$ film display a homogeneous granular surface morphology, characterized by closely packed nanoparticles. This uniformity in film morphology is essential for achieving consistent and reliable transistor performance. The images reveal some degree of porosity in the film, with particles sizes ranging approximately from 20 to 50 nm, consistent with AFM measurements.

We investigated the surface area and porosity of the $WO_3$ films by Brunauer-Emmett-Teller (BET) analysis, critical for studying intercalation processes and ion mobility within the film. The mesoporous structure revealed by BET analysis indicates a high surface area (277 $m^2/g$), essential for efficient ion gating, particularly. The film's porosity (pore volume = 0.36 $cm^3/g$ and pore size = 4.4 nm) plays a key role in facilitating ionic mobility within the transistor channel, improving ion gating performance by enhancing ions accessibility, into the $WO_3$ lattice. This, in turn, influences the device's channel current and response time (sizes of $EMIM^+$ and $Li^+$ measuring approximately 0.7 nm and 0.07 nm)[227, 228].

The structural properties of the $WO_3$ thin films were investigated using X-ray diffraction (XRD) (Figure 6.2b-inset). The diffraction pattern confirms the formation of a monoclinic $WO_3$ phase, with prominent peaks observed at 2θ values of approximately 23°, 34°, and 49°, corresponding to the (002), (200), and (020) reflections, and a high degree of crystallinity of monoclinic $WO_3$ film (indexed to Joint Committee on Powder Diffraction Standards file #JCPDS 43-1035).

### 6.5.2 Cyclic voltammetry measurements of $WO_3$-based IGT

We analyzed the CVs of $WO_3$ thin films gated by two systems: pure [EMIM][TFSI] and a mixture of 0.1 mol $L^{-1}$ LiTFSI in [EMIM][TFSI] at different scan rates (10, 50, and 100 mV/s) (Figure 6.2c, e). The CV of the $WO_3$ thin films gated with pure [EMIM][TFSI] shows distinct redox signals. However, in the presence of $Li^+$, the CV traces display broader signals with a higher voltametric current.

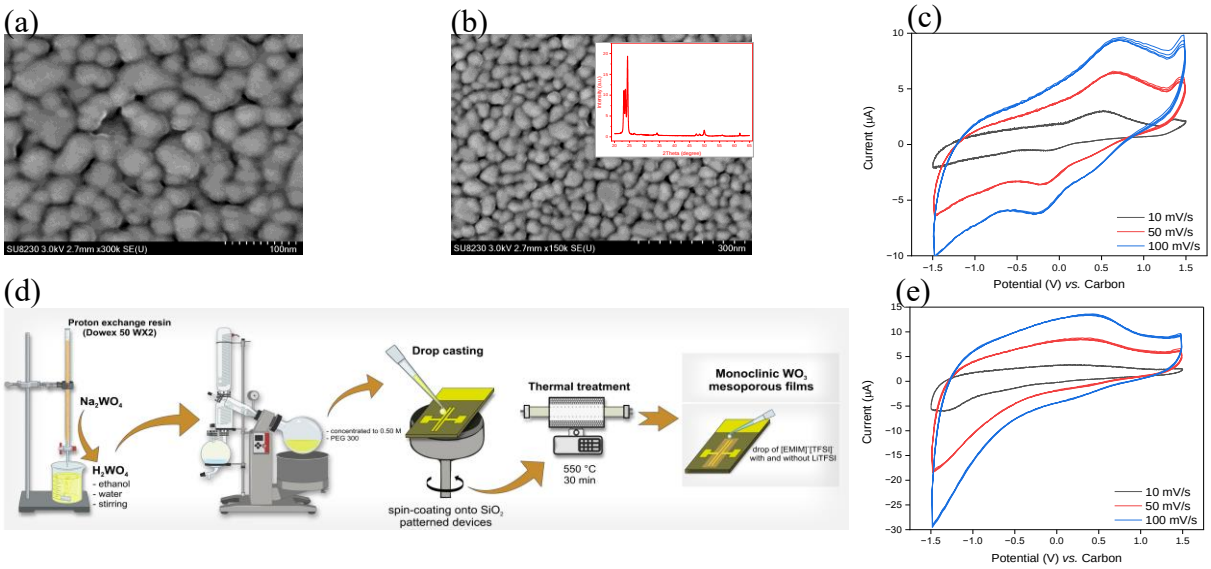


Figure 6.2 SEM images of a nanostructured $WO_3$ thin film obtained at a) 300000×, b) 150000× (inset: XRD patterns of the $WO_3$ film). CV results for spin-coated $WO_3$-IGTs with at c) [EMIM][TFSI]-gated, e) 0.1 mol $L^{-1}$ LiTFSI in [EMIM][TFSI]-gated, illustrating different scan rates (blue line: 100 mV $s^{-1}$, red line: 50 mV $s^{-1}$, black line: 10 mV $s^{-1}$). d) Schematic diagram depicting the preparation of the monoclinic $WO_3$ porous film via a solution-based method and its deposition onto gold-silicon patterned devices.

In previous works, we discussed that $WO_3$ IGTs gated by [EMIM][TFSI] undergo an interface-confined, unconventional chemical doping process, where large [EMIM] cations accumulate at the interface to compensate for the charge of the injected electrons. Conversely, in the presence of small cations such as $Li^+$, $WO_3$ undergoes an electrochemical doping process, where the cations are intercalated during the faradaic reduction via a double injection mechanism. [219]

In the absence of $Li^+$, the unconventional chemical doping mechanism dominates, with large [EMIM] cations accumulating at the interface to compensate for injected electrons, resulting in a sharper voltametric peak. Conversely, the presence of $Li^+$ enables a dual doping process, combining a conventional faradaic $Li^+/e^-$ double injection with the interface-limited unconventional $[EMIM]^+$ doping. In the pure [EMIM][TFSI] system, redox reactions primarily involve the transfer of electrons in the $WO_3$ structure. When $Li^+$ is introduced, both electron and $Li^+$ injection must be

considered ($WO_3 + ye^- + yLi^+ \leftrightarrow Li_yWO_3$). The additional charge injected via the $Li^+/e^-$ double injection mechanism results in higher voltammetric currents in the CV.

### 6.5.3 Study of EDL at the interface of gating/channel material via AFM FD profiling

To gain a better understanding of the gating mechanisms and their relationship to the neuromorphic response, we studied *in operando* the structure of the electrical double layer (EDL) formed at the ion gating medium/$WO_3$ interface. The structure of the ion layering was characterized by AFM FD profiling in devices gated with both pure [EMIM][TFSI] and 0.1 mol $L^{-1}$ LiTFSI in [EMIM][TFSI]. The devices were studied under a $V_{gs}$ = 1 V to investigate the structure of the EDL associated to an advanced degree of doping. With the AFM tip was positioned in the middle of the channel, 50-100 individual force-distance curves were collected and the results were statistically analyzed using histograms to reveal the structural characteristics of the ionic layers at the $WO_3$/IL interface. Typical two-dimensional histograms from the FD curves collected in pure [EMIM][TFSI] revealed distinguishable humps related to the first four-five ion layers (Figure 6.1e), consistent with our previous study of this type of device.[18] Interestingly, the 2D histograms collected in 0.1 mol $L^{-1}$ LiTFSI in [EMIM][TFSI] exhibited less well-resolved patterns, with clear separation observed only in the first ionic layer (Figure 6.1f).

The results were further analyzed using histograms of separations, providing clearer visualization of the peak positions and statistical distribution of the ionic layers at the selected spots. Results obtained with [EMIM][TFSI] in five different spots at the IGT channel, under $V_{gs}$ = 1 V bias (Figure 6.1g), indeed exhibited discernible peaks attributed to the first four ionic layers, with the position of the first ion layer at 0.54 ± 0.09 nm. In the case of 0.1 mol $L^{-1}$ LiTFSI in [EMIM][TFSI], only the peak related to the first ionic layer could be resolved, positioned at 0.73 ± 0.07 nm (Figure 6.1h). These results indicate that the first layer at the $WO_3$/IL interface without $Li^+$ is relatively closer to the surface compared to when $Li^+$ is present. Another significant difference related to the characteristics of the first layer peak was the value observed for the full width at half maximum (FWHM), a parameter related to the degree of ion

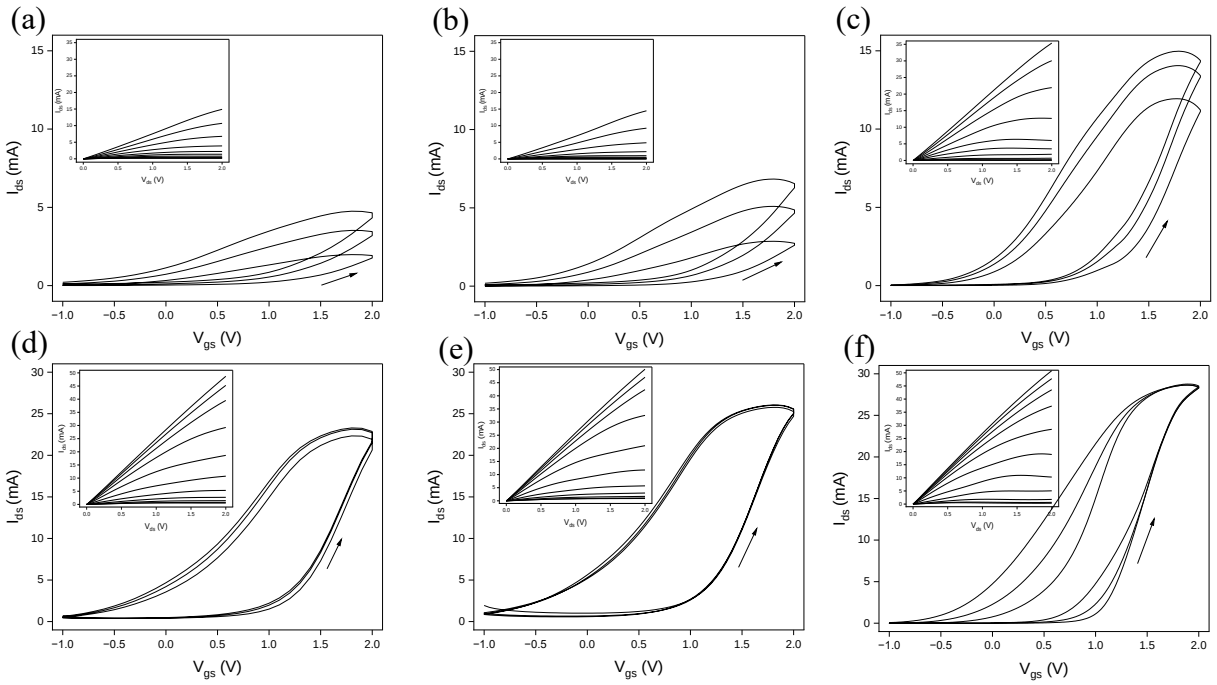


Figure 6.3. Transfer characteristics of $WO_3$-based IGT in the linear regime ( $V_{ds}$= 1.2 V, (3 cycles)) at $V_{gs}$ scan rates 100, 50, 10 $mVs^{-1}$ at a, b, c) [EMIM][TFSI]-gated, d, e, f) 0.1 mol $L^{-1}$ LiTFSI in [EMIM][TFSI]-gated (inset: output characteristics of $WO_3$ based IGT with $V_{gs}$= [0:0.2:2] V at $V_{ds}$ scan rates 100, 50, 10 $mVs^{-1}$ at a, b, c) [EMIM][TFSI]-gated, d, e, f) 0.1 mol $L^{-1}$ LiTFSI in [EMIM][TFSI]-gated)

ordering. [229] For the IL without $Li^+$, an FWHM value of 0.53 ± 0.01 nm was observed, whereas with $Li^+$ it is 0.85 ± 0.07 nm. Therefore, the sharper peaks observed in the IL without $Li^+$ suggest that the first $[EMIM]^+$ layer is much more ordered and compact compared to the layering of both $[EMIM]^+$ and $Li^+$. The absence of peaks related to subsequent layers in the presence of $Li^+$ further indicates the disordered nature of the ionic arrangement in the $Li^+$-rich ionic media.

### 6.5.4 Transistor Characterization

Transfer and output characterization of $WO_3$-based IGT with [EMIM][TFSI] (Figure 6.3a-c) and 0.1 mol $L^{-1}$ LiTFSI in [EMIM][TFSI] (Figure 6.3d-f) as gating media shows n-type semiconductor behavior. In the transfer characteristics, we observe that the $I_{ds}$ increases as $V_{gs}$ scan rate decreases from 100 to 10 $mVs^{-1}$ in both ionic media, due to the increased time available to accommodate ion

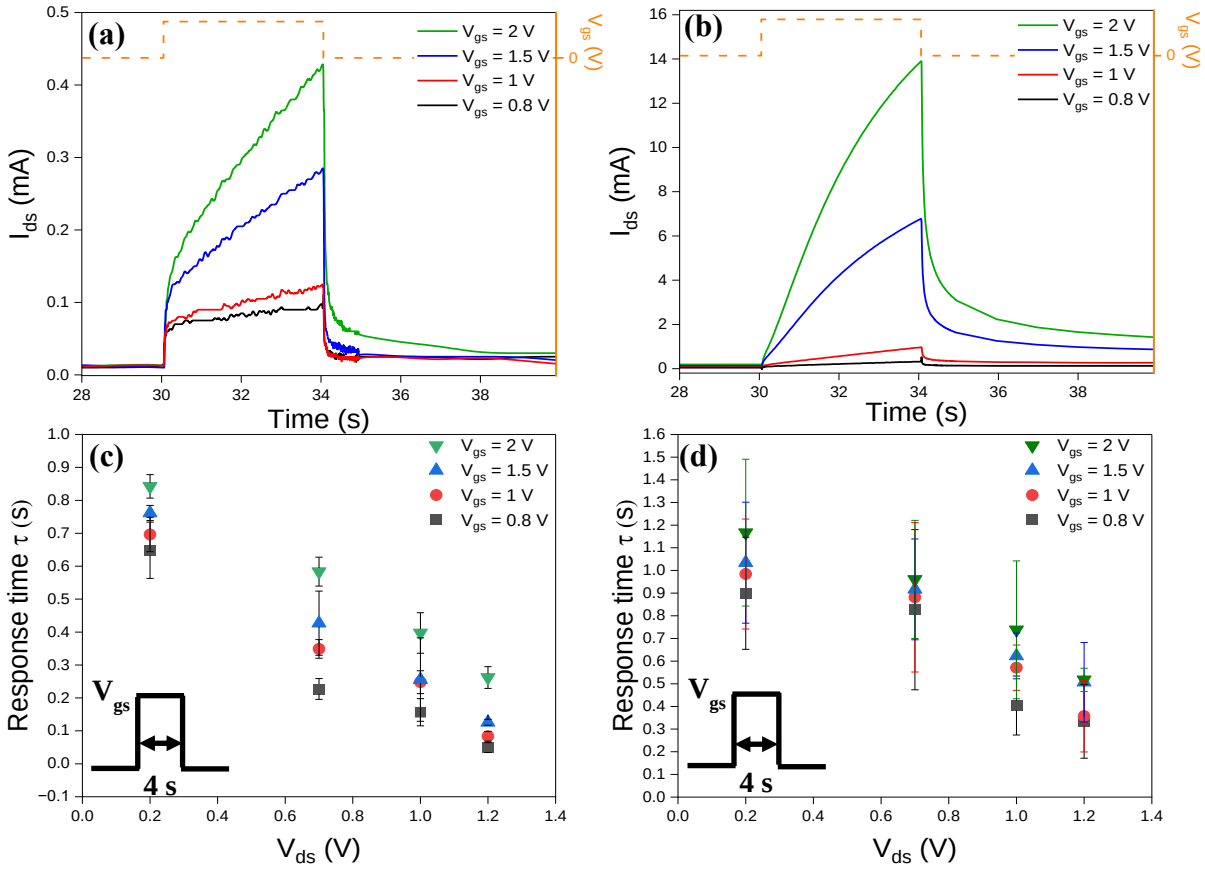


Figure 6.4 a) Spike amplitude-dependent plasticity (SADP) of $WO_3$ IGTs, showing EPSC ($I_{ds}$ pulses) responses to $V_{gs}$ pulses with varying amplitudes ($V_{gs}$ = 0.8, 1, 1.5, and 2 V), all with a duration of 4 s and $V_{ds}$ = 1.2 V, gated by a) [EMIM][TFSI] b) 0.1 mol $L^{-1}$ LiTFSI in [EMIM][TFSI]. Response time c) [EMIM][TFSI]-gated $WO_3$ based IGT d) 0.1 mol $L^{-1}$ LiTFSI in [EMIM][TFSI]-gated $WO_3$ based IGT in response to different $V_{gs}$ pulses (0.8, 1, 1.5, and 2 V) and $V_{ds}$ values (0.2, 0.7, 1, and 1.2 V), with a pulse duration of 4 s.

movement. The approximately threefold increase in $I_{ds}$ modulation observed for the $WO_3$ IGT gated with 0.1 mol $L^{-1}$ LiTFSI in [EMIM][TFSI] is attributed to the additional charge injection via the electrochemical doping process through the $Li^+/e^-$ double injection mechanism.

### 6.5.5 Synaptic behaviors and response time of WO3-based IGTs

Synaptic IGT responses to input voltage pulses are essential properties for mimicking various types of plasticity observed in neural synapses. We examined changes in response time and $I_{ds}$ current

amplitude under the application of $V_{gs}$ pulses with varied pulse amplitudes, pulse frequencies, number of pulses, and pulse durations.

**Spike amplitude-dependent plasticity (SADP) influenced by the gating medium**

An increase in $I_{ds}$ replicates the EPSC observed in biological neurons, enabling the implementation of artificial synapses. Figures 6.4a, b demonstrate SADP, illustrating the tuning of synaptic plasticity through $V_{gs}$ spike amplitude. We recorded $I_{ds}$ peaks induced by various

$V_{gs}$ amplitudes (0.8, 1, 1.5, and 2 V), all maintained at a duration of 4 s and a $V_{ds}$ of 1.2 V. We observe $I_{ds}$ peak increases with $V_{gs}$ pulse amplitude in both [EMIM][TFSI] and 0.1 mol $L^{-1}$ LiTFSI in [EMIM][TFSI]-gated $WO_3$-based IGTs. The variation in $I_{ds}$ is significantly greater in the presence of $Li^+$, with the $I_{ds}$ peak in 0.1 mol $L^{-1}$ LiTFSI in [EMIM][TFSI]-gated $WO_3$-based IGTs being 3 to 30 times higher than that in [EMIM][TFSI]-gated $WO_3$-based IGTs under applied $V_{gs}$ values ranging from 0.8 to 2 V. This transition STP to LTP, achieved through careful selection of the gating medium, results from the augmented electrochemical doping of the channel due to the intercalation of $Li^+$ within the $WO_3$ film lattice. After $V_{gs}$ pulses are removed, $I_{ds}$ start to decay, exhibiting varying response times. Both types of transistors exhibit an increase in response time with higher $V_{gs}$ and lower $V_{ds}$ (Figure 6.4c, d).

The 0.1 mol $L^{-1}$ LiTFSI in [EMIM][TFSI]-gated $WO_3$-based IGT exhibits a slower response time and maintains higher $I_{ds}$ peaks compared to the [EMIM][TFSI]-gated device, mimicking the long-term synaptic weight modulation seen in biological synapses (long-term plasticity, LTP).

This slower response time is achieved by introducing $Li^+$ from the ionic medium into the $WO_3$ channel of the IGT. $Li^+$ can penetrate the $WO_3$ lattice more deeply than the larger $[EMIM]^+$. When positive $V_{gs}$ is removed, $Li^+$ diffuse back from the $WO_3$ lattice to the ionic medium over a longer duration than $[EMIM]^+$, leading to a slower response time (Figure 6.4c, d). The errors observed in the results, derived from experiments conducted on three $WO_3$-based transistors.

**Spike number-dependent plasticity (SNDP) influenced by the gating medium**

To investigate the impact of incorporating $Li^+$ on LTP in $WO_3$-based IGTs, we applied $V_{gs}$ pulse trains. Successive stimuli contribute to the gradual modulation of electrical conductance or synaptic weight, a phenomenon known as SNDP, calculated as $(I_{dsn} - I_{ds1}) / I_{ds1} \times 100\%$, where *n* represents

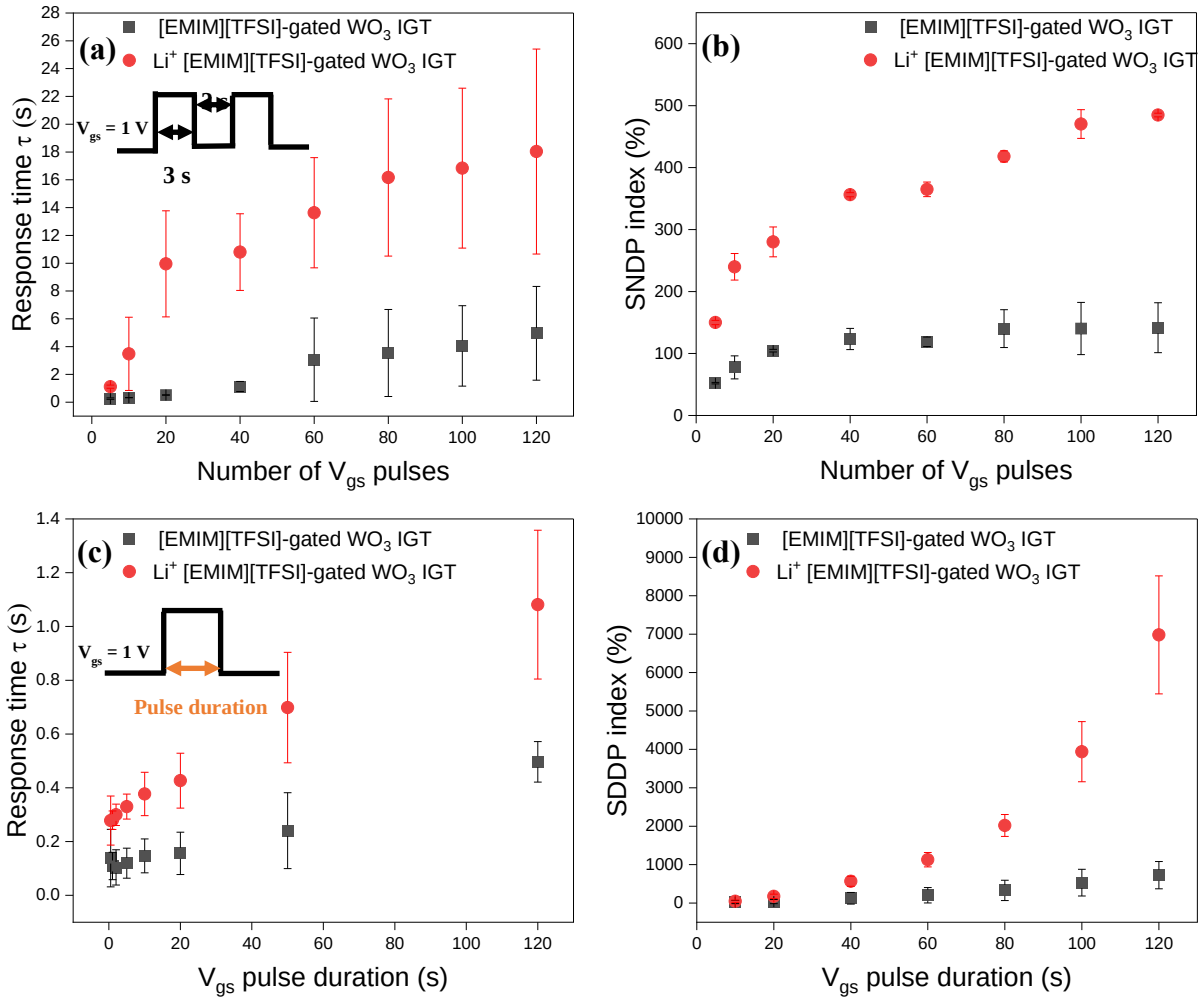


Figure 6.5 Synaptic behavior of artificial synapses for 0.1 mol $L^{-1}$ LiTFSI in [EMIM][TFSI] and [EMIM][TFSI] gated $WO_3$ IGT. a) Response time of $WO_3$ IGT versus different numbers of square step train $V_{gs}$ pulses, from 5 to 120 pulses. $V_{gs}$ and $V_{ds}$ = 1 V. b) SNDP index as a function of the number of $V_{gs}$ pulses, $V_{gs}$ and $V_{ds}$ = 1 V. c) Response time of $WO_3$ IGT versus $V_{gs}$ pulse duration. d) SDDP index as a function

the number of $V_{gs}$ pulses. Figure 6.5b shows the SNDP index behavior in both [EMIM][TFSI]-gated and 0.1 mol $L^{-1}$ LiTFSI in [EMIM][TFSI]-gated $WO_3$-based IGTs, where we applied 5, 10, 20, 40, 60, 80, 100, and 120 consecutive $V_{gs}$ = 1 V pulses with a constant $V_{ds}$ = 1 V, a pulse duration and interval of 3 s.

Two major differences were observed between the two types of transistors. First, the [EMIM][TFSI]-gated transistor exhibited a faster response time than the other type following $V_{gs}$ pulse trains, as shown in Figure 6.5a. The increasing number of pulses leads to deeper insertion of $Li^+$ into the $WO_3$ lattice, resulting in a prolonged de-doping process and a slower

response time. Second, the SNDP index of the [EMIM][TFSI]-gated IGT, as shown in Figure 6.5b, exhibited saturation with an increasing number of $V_{gs}$ pulses; this saturation was not of the Vgs pulses duration.

observed in the presence of Li+, thus indicating the difference in the change of channel conductance between the two different gating media of $WO_3$-based IGTs. These differences in

conductance changes became more pronounced after 100 to 120 consecutive pulses. Therefore, it can be concluded from Figure 6.5a, b that the transition from STP to LTP in the artificial synapse is highly dependent on the number of $V_{gs}$ pulses, especially in the presence of $Li^+$.

**Spike duration-dependent plasticity (SDDP)influenced by the gating medium**

When $V_{gs}$ pulses with pulse durations of 10 s or shorter were applied, both [EMIM][TFSI]-gated and 0.1 mol $L^{-1}$ LiTFSI in [EMIM][TFSI]-gated $WO_3$ based IGTs exhibited STP behavior, as shown in Figure 6.5c. However, if the pulse duration is applied for more than 50 s, IGTs start to show LTP.

Figure 6.5d shows the SDDP diagrams in the $WO_3$ artificial synapse exclusively in dependence on two input parameters: gating medium and pulse duration. During the SDDP index measurement shown in Figure 6.5d, we increase the pulse duration from 0.5 s to 120 s. We varied the gating medium from [EMIM][TFSI]-gated IGT to 0.1 mol $L^{-1}$ LiTFSI in [EMIM][TFSI]-gated IGT are measured under $V_{gs}$ = 1 and $V_{ds}$=1. With increasing pulse duration in both IGTs, the response time increases, although we can see a much slower response time in the presence of $Li^+$. Lithiation can cause a delay in de-doping time and increase $\tau$.

**Frequency-Dependent Plasticity (FDP) influenced by the gating medium**

The FDP synaptic behavior we study here refers to a characteristic of the IGT artificial synapse, where the synaptic weight (conductance state) changes not only with the duration of the applied

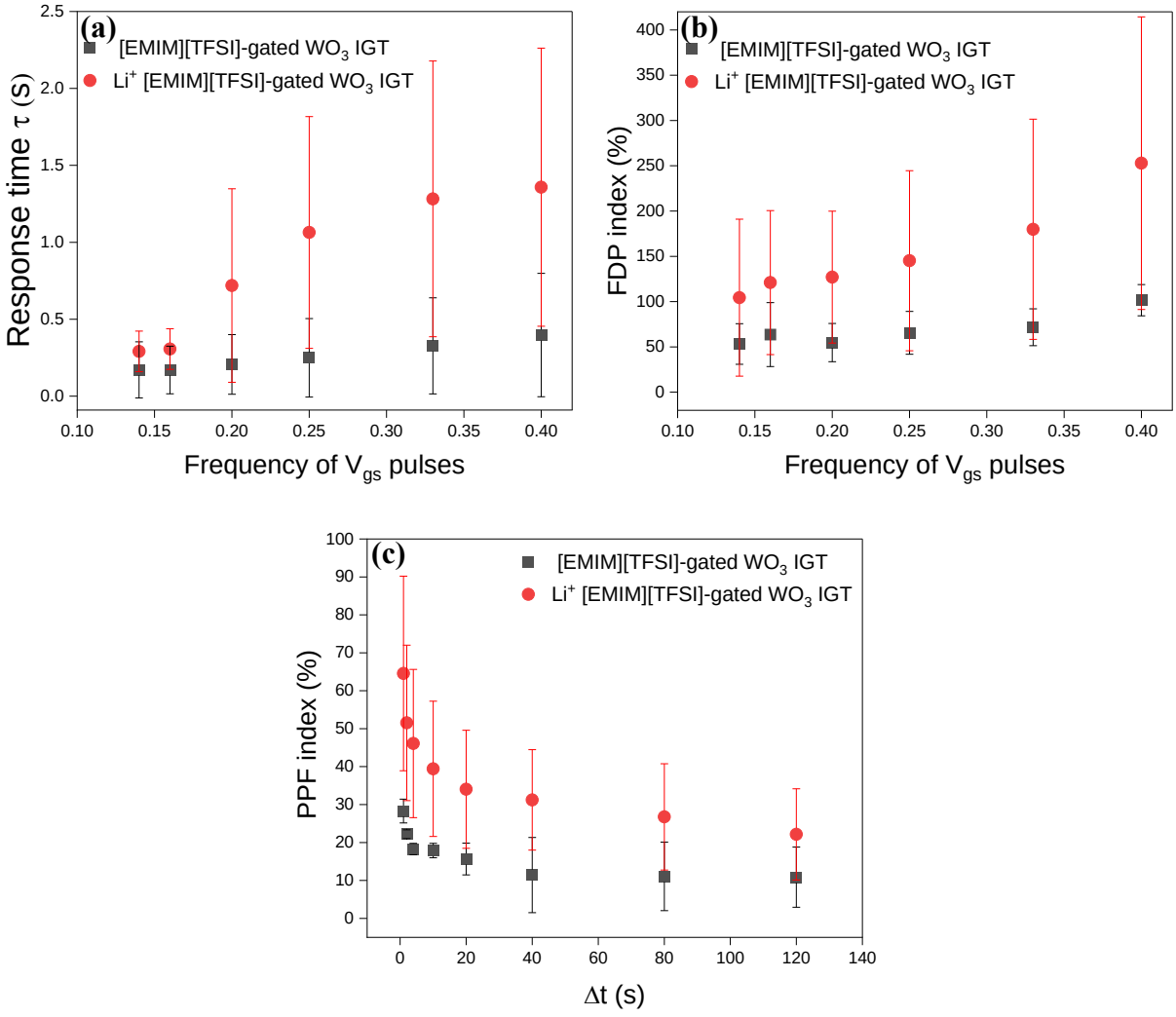


Figure 6.6. a) Response time versus $V_{gs}$ pulse frequency for 0.1 mol $L^{-1}$ LiTFSI in [EMIM][TFSI] and [EMIM][TFSI] gated $WO_3$ IGT. b) FDP index as a function of the frequency of $V_{gs}$ pulses. c) PPF index after applying two consecutive $V_{gs}$ = 1 V pulses versus Δt, the time interval of pulses.

$V_{gs}$ pulse but is also strongly related to the variation of $V_{gs}$ time interval within each spike cycle of presynaptic spike trains. To measure the effect of FDP we apply the train of 10 $V_{gs}$ pulses with an amplitude of 1 V, same duration time 2 s, and frequency of 0.14, 0.16, 0.2, 0.25, 0.33, 0.4 Hz to [EMIM][TFSI]-gated and 0.1 mol $L^{-1}$ LiTFSI in [EMIM][TFSI]-gated $WO_3$ IGT. The FDP index demonstrates that as the frequency of the presynaptic spike ($V_{gs}$) train increases, $I_{ds}$ gradually increases for both types of IGTs with different gating media. Figure 6.6b illustrates the frequency-

dependent $I_{ds}$ gain, which is calculated as FDP = $(I_{ds10} - I_{ds1})/I_{ds1} \times 100\%$, where $I_{ds10}$ and $I_{ds1}$ represent the $10^{th}$ and $1^{st}$ $I_{ds}$ values, respectively. The FDP gain increases from 53% to 101% as the frequency rises from 0.14 to 0.4 Hz for the [EMIM][TFSI]-gated $WO_3$-IGT. In comparison, the presence of $Li^+$ in the gating medium leads to a more pronounced enhancement of the FDP index, increasing from 104% to 253% over the same frequency range. Figure 6.6a shows the response time of $WO_3$-IGT as a function of $V_{gs}$ frequency, where an increase in response time with rising frequency is observed. At higher $V_{gs}$ frequencies (with the same number of spikes), more ions penetrate the channel, leading to longer redistribution times and slower response. The presence of $Li^+$ in the gating medium further extends the redistribution time, making it longer than that of the [EMIM][TFSI]-gated IGT (Figure 6.6a).

**Paired-pulse facilitation (PPF)**

Paired-pulse facilitation (PPF) is known for decoding temporal information in auditory and visual signals. We investigated PPF behavior and compared them between [EMIM][TFSI]-gated and 0.1 mol $L^{-1}$ LiTFSI in [EMIM][TFSI]-gated $WO_3$-IGT. PPF behavior was induced by applying a pair of identical $V_{gs}$ pulses (1 V, 4 s), with varying interval time ($\Delta t$), (1, 2, 4, 10, 20, 40, 80, 120 s) as shown in Figure 6.6c (PPF = $\Delta I_{ds}/I_{ds1} \times 100\%$). We observed that the $I_{ds}$ change induced by the second pulse is greater than that caused by the first. This increase in conductance (facilitation) is attributed to ion insertion into the channel during the first pulse, while the second pulse was applied before the ions had fully diffused back into the ionic medium. As a result, $I_{ds}$ increased after the second pulse due to higher ion concentration in the channel. In the presence of $Li^+$, the $I_{ds}$ increase induced by the second pulse is greater than that observed in IGTs without $Li^+$ in the system. In this case, the delithiation of $WO_3$ takes more time after the removal of the first $V_{gs}$ pulse, allowing $I_{ds}$ to experience a greater increase with the application of the second $V_{gs}$ pulse. The highest PPF index of 72% was achieved in the 0.1 mol $L^{-1}$ LiTFSI in [EMIM][TFSI]-gated IGT, while the PPF index for the [EMIM][TFSI]-gated IGT was 32%. The PPF index was found to decrease as the interval time increased. This decrease occurs because longer intervals between pulses allow ions to relax back into the ionic medium, thereby diminishing the effect.

## 6.6 Conclusion

In conclusion, this study successfully demonstrates the fabrication and detailed characterization of a $WO_3$-based ion-gated synaptic transistor tailored for neuromorphic computing applications. By using [EMIM][TFSI] and 0.1 mol $L^{-1}$ LiTFSI in [EMIM][TFSI] as gating media, we systematically investigate the material and transistor characteristics, revealing significant insights into their behavior and performance.

AFM FD profiling and CV analyses provide a comprehensive understanding of the EDL structure and electrochemical properties. The combined experiments suggest that the less ordered and less compact EDL at the IL/MO interface layer in 0.1 mol $L^{-1}$ LiTFSI in [EMIM][TFSI] results from $Li^+$ being present inside the channel bringing about electrochemical doping. On the other hand, in $WO_3$ IGT gated with pure [EMIM][TFSI], there is evidence that the interface-confined unconventional doping and electrostatic effect leads to a higher degree of organization of the EDL and clearly-defined voltammetric peaks. The differences between the dominance of faster electrostatic/interface-confined and slower electrochemical doping processes (which include ionic transport) significantly impact conductance modulation and time response to different bias signals in the neuromorphic devices using the two gating media. Notably, the presence of $Li^+$ in the gating medium enhances the device performance, as evidenced by a threefold increase in $I_{ds}$ in the transfer curves. This enhancement is attributed to $Li^+$ intercalation, which enhances conductivity while affecting the device's response time.

The synaptic behavior observed in the $WO_3$-based IGTs, including STP, LTP, SADP, SNDP, SDDP, FDP, and PPF, demonstrate that these devices can effectively mimic key neural synapse functions, highlighting their potential in neuromorphic systems. These findings underscore the importance of ionic medium selection in optimizing the synaptic transistor response time, current amplifying, and transition between STP and LTP, paving the way for the development of energy-efficient and high-performance neuromorphic systems capable of adaptive learning and real-time processing.

Overall, our study highlights the promise of $WO_3$-based IGTs in advancing intelligent systems, emphasizing their potential to replicate the dynamic and adaptive functionalities of biological synapses, thereby contributing to the future of neuromorphic computing. Future work will focus

on further optimizing the material properties and exploring other ionic compositions to enhance the synaptic behavior and overall performance of these promising devices.

## 6.7 Experimental Section/Methods

### 6.7.1 Preparation of $WO_3$ Films

We used a solution-based method to prepare the $WO_3$ thin films (Figure 6.2d). [1] Specifically, tungstic acid ($H_2WO_4$) was prepared by passing 20 mL of a 0.5 mol $L^{-1}$ $Na_2WO_4$ aqueous solution through proton-exchange resin (Dowex 50WX2, 100-200 mesh). The resin was previously preconditioned in 50 mL of 1 mol $L^{-1}$ $H_2SO_4$ for 30 min and washed several times with deionized water (DIW) to achieve a pH of 7. The eluted solution was collected in 16 mL of ethanol under continuous magnetic stirring to slow down the condensation. Subsequently, the solution's volume was reduced under low pressure and heating to achieve a concentration of approximately 0.5 mol $dm^{-3}$. As an organic stabilizer, 4 mL of PEG-300 was added to the freshly evaporated stirred solution ($WO_3$/PEG-300 ratio of ~0.5 w/w). A viscous, pale yellowish precursor solution (under continuous stirring) was stored in dark conditions before precipitation and used to fabricate $WO_3$ films for no more than three days. The precursor was spin-coated onto the device surface. The deposition involved drop-casting 40 µL and spinning at 4000 rpm for 40 seconds. The deposited layer was dried at room temperature for 10 minutes and subsequently annealed in a tubular furnace (under flowing oxygen) at 550 °C for 30 minutes.

### 6.7.2 Fabrication of the IGT device

We used $WO_3$ films on $SiO_2$/Si substrates as [EMIM][TFSI]-gated IGT channels, with photolithographically patterned source and drain electrodes (40 nm Au on 5 nm Ti) spaced L = 10 µm apart and W = 4 mm wide. Before $WO_3$ film deposition, substrates were sequentially ultrasonically cleaned with isopropyl alcohol, acetone, and isopropyl alcohol (10 min each), then exposed to UV-Ozone for 15 minutes. Before use, the ionic liquid [EMIM][TFSI] (from IoLiTec, with a purity of over 99%) was purified under vacuum conditions of approximately $10^{-5}$ Torr for 24 hours at 60 °C and then was dropped on a DuraporeR membrane, typically 4 mm × 9 mm in size and 125 µm thick, positioned in alignment with the transistor channel. To prepare an alternative gating medium, 0.1 mol $L^{-1}$ LiTFSI in [EMIM][TFSI] for applying on the membrane,

bis(trifluoromethane)-sulfonimide lithium salt (LiTFSI, Sigma-Aldrich, 99.95%) was dissolved in purified [EMIM][TFSI] until $Li^+$ concentration of 0.1 mol $L^{-1}$ was achieved. The gate, along with the reference/counter electrode, was composed of a high surface area carbon paper (Spectracarb 2050), measuring 6 mm × 3 mm and 170 μm in thickness. This was coated with an ink formulated from activated carbon (PICACTIF SUPERCAP BP10, Pica, at a concentration of 28 mg $ml^{-1}$) and a polyvinylidene fluoride (PVDF, KYNAR HSV900, at a concentration of 1.4 mg $ml^{-1}$) binder, all in N-methyl pyrrolidone (NMP, sourced from Fluka).

### 6.7.3 Materials characterization

AFM, SEM and XRD were employed to investigate the $WO_3$ film under ambient conditions. The AFM images were acquired in semi-contact (tapping) mode using an NSG10 cantilever with specific dimensions (length: 95 μm, width: 30 μm, resonant frequency: 240 kHz, and force constant: 11.8 N/m) utilizing an NT-MDT NTEGRA II microscope. Additionally, the structure of $WO_3$ films was analyzed via XRD using a Bruker D8 instrument with a Cu-Kα source (wavelength: 1.54 Å). The film thickness was determined using a profilometer (Dektak 150). SEM images were obtained using a Hitachi SU-8230 Cold Field Emission Scanning Electron Microscope (CFE-SEM), which has an electron source size of 5 nm, and an energy spread ranging from 0.2 to 0.3 eV.

### 6.7.4 Electrical and electrochemical characterizations of $WO_3$-IGT

In an $N_2$ glovebox with $H_2O$ and $O_2$ concentrations below 3 ppm, electrical and electrochemical characterizations were conducted. Transistor characteristics were analyzed using an Agilent B1500A semiconductor parameter analyzer in a custom electrical probe station. Cyclic voltammetry measurements were taken with a VersaSTAT4 potentiostat.

AFM FD profiles were collected using a Cypher AFM from Asylum Research (Oxford Instruments, UK) using the Cypher droplet holder and TR800PB (Olympus) probes with a nominal spring constant of 0.61 N/m. A droplet of purified [EMIM][TFSI] or 0.1 mol $L^{-1}$ LiTFSI in [EMIM][TFSI] was added to the devices. The FD curves were collected with a ramp distance of 30 nm and a ramp rate of 0.5 Hz. To control the drain-source and gate-source electrical bias (electrical measurements), an SP-300 two-channel potentiostat (Biologic) was used.

## 6.8 Acknowledgements

C.S. acknowledges NSERC (Discovery Grant) and the Canada Research Chairs for financial support.

# CHAPTER 7 GENERAL DISCUSSION

In this PhD thesis, our focus was on IGTs as bio-inspired synaptic devices for neuromorphic applications. Neuromorphic computing, inspired by the human brain's capability to process and store information simultaneously, represents a major step forward in computing technology. Across the three papers presented in this dissertation, we explored various aspects of synaptic IGTs, focusing on different materials, configurations, and factors affecting their synaptic behavior, especially in the context of spike-amplitude and width dependent plasticity, SNDP and FDP. This work contributes to the understanding of how IGTs, particularly those using P3HT organic semiconductors and $WO_3$ metal oxides as channel materials, can replicate synaptic plasticity, a key requirement for neuromorphic systems. We utilized IL as gating media to replace conventional dielectrics such as $SiO_2$. The channel materials we used can take up ions when interfaced with the ionic medium, leading to electrostatic and/or electrochemical doping. Using ILs as the gating media takes advantage of their excellent thermal stability and wide electrochemical window. This enables the formation of EDLs at the interface between the ion gating medium and the semiconductor channel, resulting in high capacitance (10-40 μF $cm^{-2}$) and charge carrier density (~$10^{15}$ $cm^{-2}$), and low operating voltages (less than 2 V). We used different ions in the gating media to evaluate the performance of the IGTs. The diffusion barrier for Li ions in our IGTs is quite low due to their small size. This makes the channel material more easily (de)doped by $Li^+$ ions. The intercalation and deintercalation of $Li^+$ ions into the mixed (ionic and electronic) conductor channel enhance the plasticity performance. The doping mechanism of an IGT can be precisely adjusted by engineering materials and operation parameters, enabling fine-tuning for specific applications, such as processing and memory functions in neuromorphic systems.

In Article 1 (Chapter 4) we fabricated an [EMIM][TFSI]-gated IGT based on regioregular P3HT organic semiconductor channel. This article begins by exploring the doping mechanism of our P3HT-based IGTs. We investigated this mechanism by fabricating P3HT channel materials (50-70 kDa MW), considering the semiconducting polymer transistor channel morphologies. Applying $V_{gs}$ pulses (pre-synaptic spike) induces the formation of an EDL, doping regions in the P3HT near the interface and/or in the (preferentially) amorphous areas of channel. We used AFM and XRD techniques to investigate the topography and structure of the films. Different sweep rates of 100,

50, 25, and 1 mV/s were used to study the ion-gating behavior. ON/OFF ratios of $1.7\times10^3$, $2\times2.6\times10^3$, $3.1\times10^3$, and $5.8\times10^4$, along with charge carrier densities of $1.3\times10^{15}$, $1.7\times10^{15}$, $2.1\times10^{15}$, and $5.7\times10^{15}$, were obtained at these sweep rates. The results showed that both the ON/OFF ratio and charge carrier density increased as the sweep rate decreased. We demonstrated how the response time ($\tau$) of P3HT-based IGTs could be controlled by varying the input $V_{gs}$ and $V_{ds}$ amplitude, pulse duration, pulse frequency, and number of pulses. The results revealed that increasing the $V_{gs}$ pulse amplitude and number of pulses brings about longer response times, with deep ion penetration into the P3HT channel being one of the critical factors modulating the transition from STP to LTP. This transition mirrors the biological processes observed in synaptic connections, where repeated stimuli lead to memory formation.

Article 2 (Chapter 5) focused on the influence of the molecular weight (MW) and film thickness of channel material on P3HT IGT response time and synaptic behavior.

We investigated the p-type organic semiconductor P3HT with low, intermediate, and high MWs (i.e. 24 kDa, 42 kDa, 92 kDa) as the channel material of [EMIM][TFSI] gated IGTs. At a sweep rate of 25 mV/s, ON/OFF ratios of $0.8 \times 10^3$, $2.1 \times 10^3$, and $3.5 \times 10^3$ were obtained for low, intermediate, and high MW P3HT, respectively. Corresponding charge carrier densities of $1.6 \times 10^{15}$, $2 \times 10^{15}$, and $2.3 \times 10^{15}$ $cm^{-2}$ were observed. The study revealed that films with higher MWs exhibit higher transconductance. We observed increasing the MW leads to greater entanglement of P3HT chains, along with an increase in the short-range ordered regions of the films, expected to enhance ion permeability, thereby facilitating the (de)doping of P3HT.

We observed that $\tau$ increases as $V_{gs}$ increases for all P3HT MWs. Higher $V_{gs}$ likely leads to deeper ion penetration into the films, which explains the longer ion removal times and the steady state of $I_{ds}$ after $V_{gs}$ is removed (LTP). Additionally, we found that increasing $V_{ds}$ leads to a decrease in $\tau$ that is in line with Bernards' model. [92] Based on the decreasing ion permeability in low MWs, the $\tau$ was longer for P3HT with lower MWs.

We evaluated the effect of MW on the synaptic behavior of IGTs. By studying SNDP in synaptic P3HT IGTs with different MWs, we observed a transition from STP to LTP as the number of $V_{gs}$ pulses increased. The increase in P3HT MW, accompanied by a corresponding increase in the amorphous regions of the channel material, paralleled by enhanced channel permeability,

contributes to a two-fold faster transition from STP to LTP in low MW compared to their high MW counterparts. We identified the same trend in PPF and pulse duration-dependent plasticity.

We examined the effect of varying channel thicknesses, determined by spin coating rates (500, 1000, 2000, 4000 rpm), on τ. Thinner P3HT channels, with lower degrees of order (as supported by AFM and XRD data), exhibited higher permeability, resulting in faster τ. Our study demonstrates a significant increase in response time as the thickness of the P3HT film increases. Additionally, thicker films led to improved synaptic behavior, including PPF and SNDP, both crucial for mimicking the adaptive learning capabilities of biological systems. The transition from STP to LTP was controlled by adjusting the film thickness, with thicker P3HT films achieving higher levels of LTP.

In manuscript 3 (Chapter 6), we expanded our study of IGTs to include n-type $WO_3$-based transistors with two room-temperature IL gating media, [EMIM][TFSI] and 0.1 mol $L^{-1}$ LiTFSI in [EMIM][TFSI]. $WO_3$ films were synthesized using the sol-gel solution process and deposited by spin-coating. AFM and SEM images revealed that $WO_3$ films exhibit a mesoporous and homogeneous granular structure, characterized by closely packed nanoparticles with sizes ranging from 20 to 50 nm. BET analysis shows a pore volume of 0.36 $cm^3/g$ and a pore size of 4.4 nm. This porosity is crucial for facilitating ionic transport within the channel and improving ion gating performance by enhancing the accessibility of ions such as $[EMIM]^+$ and $Li^+$, which are definitively smaller than the pore size, though their effective sizes vary depending on the measurement technique and their interaction with the surrounding environment. We observed two types of mechanisms contributing to the doping process in the nanostructured $WO_3$ channel: electrostatic and electrochemical (faradic) doping. This finding was supported by in operando and AFM Force Distance profiling. The operating voltages of $WO_3$-IGTs are approximately 1 V, and the ON/OFF ratios reach values as high as $10^2$ - $10^5$.

This contribution presents key insights from the design, fabrication, characterization, and investigation of the synaptic behavior of $WO_3$-IGTs for applications in neuromorphic computing. These insights are discussed in relation to the nature of different ion gating media, nanostructured $WO_3$ films, EDL creation at the IL/$WO_3$ interface, and the effect of these parameters on response time and synaptic behaviors of IGT. The incorporation of $Li^+$ into the gating medium significantly

boosts device performance, reflected by a threefold rise in $I_{ds}$ within the transfer curve. This improvement is linked to $Li^+$ intercalation, which leads to the increase of the transistor current and impacts the device response time. Both [EMIM][TFSI] and 0.1 mol $L^{-1}$ LiTFSI gated $WO_3$-IGTs exhibited synaptic behaviors such as STP, LTP, SADP, SNDP, SDDP, FDP, and PPF, indicating their ability to replicate essential neural synapse functions and underscoring their potential in neuromorphic applications. The findings also revealed that incorporating $Li^+$ ions into the IL gating medium significantly slows response time, enhancing the transition from STP to LTP. $WO_3$-based IGTs feature memory retention and synaptic weight modulation relevant for analog computing, where efficient, low-power learning mechanisms are essential.

While this research has made significant strides in understanding and optimizing IGT performance, several challenges remain. One limitation is the relatively slow response times observed in some configurations, particularly in $WO_3$-based devices. While slower response times can be advantageous for long-term memory retention, they may limit the applicability of these devices in real-time computing scenarios where rapid information processing is critical. Future research should focus on balancing speed and memory retention by optimizing the composition of the gating medium and refining the channel materials. Another limitation lies in the scalability of these devices. While P3HT and $WO_3$ offer promising results, the fabrication processes for these materials are complex and may hinder large-scale implementation. Developing simpler, more cost-effective fabrication techniques will be crucial for the widespread adoption of neuromorphic systems. Additionally, current studies focused primarily on electrical characteristics such as response time, transconductance, and plasticity modulation. However, the integration of these IGTs into fully functional neuromorphic networks remains an area for further exploration. Future work should investigate how these devices perform in more complex, interconnected systems, evaluating their robustness and efficiency in larger networks that more closely mimic the structure of biological brains. Lastly, the environmental stability of these materials, particularly organic semiconductors like P3HT, poses a concern for long-term applications. Research aimed at improving the durability of these materials under varying environmental conditions, such as humidity and temperature fluctuations, or by encapsulating devices, will be crucial for their implementation in real-world applications.

In general, the findings presented in this dissertation highlight several critical factors that influence the performance of synaptic IGTs, paving the way for more efficient neuromorphic systems. The ability to transition between STP and LTP is particularly significant, as it mimics the learning and memory formation mechanisms of biological synapses. The fine-tuning of response times through the manipulation of materials, device structure, and gating conditions opens opportunities for creating more energy-efficient, adaptive computing systems.

Neuromorphic computing seeks to overcome the limitations of traditional von Neumann architecture, which separates memory and processing units, by integrating both in the same hardware. The IGTs discussed in this work align well with this goal, as they offer a platform for collocated memory and processing. Additionally, the low power consumption of these devices makes them suitable for applications in large-scale neural networks, where energy efficiency is paramount. The different material systems investigated -P3HT for its organic flexibility and $WO_3$ for its robust ionic conduction properties- offer unique advantages. P3HT-based IGTs exhibit faster response times, making them ideal for applications requiring quick, short-term memory functions. In contrast, $WO_3$-based devices, especially when doped with Li ions, demonstrate stronger long-term memory retention, positioning them as suitable candidates for tasks that require durable learning mechanisms.

# CHAPTER 8 CONCLUSION AND RECOMMENDATIONS

This dissertation has demonstrated the versatility of synaptic ion-gated transistors as neuromorphic devices capable of mimicking key aspects of biological synapses. By exploring the effects of material composition, device architecture, and gating conditions, we have made significant progress in understanding how to optimize IGT performance for neuromorphic computing applications. The results from these studies contribute to the ongoing development of more efficient, adaptive computing systems that could one day rival the processing power and energy efficiency of the human brain.

We fabricated IGTs with solution-processed channels, incorporating different materials for both the channel (organic polymer and $WO_3$) and gating. These transistors operate at threshold voltages around 1 V, using a rigid $SiO_2$/Si substrate, gold source and drain electrodes, a high surface area activated carbon gate electrode, and ionic liquids (ILs) as the gating medium. We propose a correlation between ex situ analyses like XRD, AFM, SEM, and BET, and in operando tones, such as AFM FD and CV. This correlation includes channel material morphology, structural changes of the EDL at the interface of the channel material and ILs under the application of $V_{gs}$, as well as the transistor transfer and output characteristics. We investigated the doping mechanism of IGTs by varying the channel material, thickness, and ion size in the ion-gating medium. Our observations revealed that the operation of IGTs relies on a combination of electrostatic and electrochemical doping. The significance of this study is that we demonstrate the potential of IGTs to function as neuromorphic devices, integrating both memory (LTP) and processing (STP) functions within the same device, depending on the applied electrical biasing conditions.

First, we fabricated IGTs based on spin-coated organic P3HT films, designed as bio-inspired artificial synapses. The response time and synaptic plasticity of P3HT IGTs were investigated by manipulating input stimuli, including $V_{gs}$ and $V_{ds}$ amplitudes, as well as the number, duration, and frequency of $V_{gs}$ pulses. Results indicated that both response time and plasticity improved with higher Vgs values, increased pulse durations (SDDP), and repetitions (SNDP), along with reduced pulse frequency (FDP). Additionally, we successfully emulated synaptic functions, demonstrating

short-term plasticity (STP), long-term plasticity (LTP), and their transition, all maintained at low driving voltages (~1 V).

Second, we investigated how the structure of the transistor channel material, as associated to different P3HT MWs and film thicknesses, affects how the applied bias conditions affect response time. We fabricated P3HT IGTs with low (24 kDa), intermediate (42 kDa), and high (92 kDa) MWs. The low MW P3HT films exhibited a higher degree of order, correlating with lower ion permeability compared to intermediate and high MW P3HT films, which resulted in devices with low transconductance and longer response times, when subjected to $V_{gs}$ pulses. We mimicked synaptic behaviors, such as PPF and SNDP, STP, LTP, and transition between them, by adjusting $V_{gs}$ pulses parameters. IGTs with low MW P3HT consistently demonstrated a more efficient transition from STP to LTP than those with high MW P3HT.

We also found that, in P3HT-based IGTs, thicker P3HT films, deposited at lower spin coating speeds and resulting in more ordered structures, exhibit lower transconductance and significantly higher response time. Additionally, increasing the thickness of the P3HT films shifts synaptic behaviors, including PPF, SNDP, and the transition from STP to LTP.

Lastly, studying artificial synapses in metal oxide ion-gated transistors is of significant interest. This research can broaden our understanding of synaptic devices by systematically investigating material and transistor characteristics, leading to valuable insights into their behavior and performance. We conducted the fabrication and detailed characterization of a $WO_3$-IGTs by utilizing [EMIM][TFSI] and 0.1 mol $L^{-1}$ LiTFSI in [EMIM][TFSI] as gating media, designed for neuromorphic computing applications.

We conducted CV AFM and FD profiling analyses to investigate the EDL structure and electrochemical properties. In $WO_3$ IGTs gated with pure [EMIM][TFSI], we observed a higher degree of organization in the EDL due to the relatively large size of $[EMIM]^+$, which brings about interface-confined unconventional doping and electrostatic doping mechanisms. Conversely, the presence of $Li^+$ ions in the gating medium resulted in a less ordered and less compact EDL at the ionic medium/metal oxide interface, paralleled by electrochemical doping. Including Li ions in the gating medium of $WO_3$-IGTs leads to increased channel conductance (a threefold increase in $I_{ds}$) and time response, at various $V_{gs}$ biases.

The synaptic behavior observed in the $WO_3$-based IGTs, including STP, LTP, SADP, SNDP, SDDP, FDP, and PPF, demonstrate that these devices effectively mimic key neural synapse functions, highlighting their potential in neuromorphic systems. These findings emphasize the importance of the ionic medium selection for optimizing the synaptic transistor response time, current amplification, and transition between STP and LTP, paving the way for the development of energy-efficient, high-performance neuromorphic systems capable of adaptive learning and real-time processing.

In conclusion, this dissertation successfully achieved its objectives by fabricating and characterizing P3HT and $WO_3$-based IGTs, elucidating the effects of the device operating conditions, ion gating medium and channel morphology on transistor performance. We explored the role of room temperature ionic liquids in doping processes, investigated the factors affecting response time and synaptic behavior, and examined the influence of transistor channel thickness on device performance. Additionally, we integrated materials science with neuromorphic applications through ex situ and in operando characterization techniques, establishing critical relationships between materials' properties and synaptic functions. Our study underscores the considerable potential of IGTs in advancing intelligent systems, particularly their ability to replicate the dynamic and adaptive functionalities of biological synapses. Such capabilities are essential for the progress of neuromorphic computing, which aims to develop systems that process information similarly to the human brain.

Future research will concentrate on optimizing the materials' properties of these devices and exploring various compositions for the ion gating media to further enhance their synaptic behavior and overall performance. Additionally, we propose that research should focus on improving the scalability, speed, and robustness of IGTs while investigating their integration into larger, more complex neural networks. With ongoing advancements in materials science and device engineering, the realization of brain-like computing systems may soon be within reach.

# REFERENCES

References


[1] Q. Wan, M. T. Sharbati, J. R. Erickson, Y. Du, and F. Xiong, "Emerging artificial synaptic devices for neuromorphic computing," *Advanced Materials Technologies,* vol. 4, no. 4, p. 1900037, 2019.

[2] Q. Liu *et al.*, "Fully printed all-solid-state organic flexible artificial synapse for neuromorphic computing," *ACS applied materials & interfaces,* vol. 11, no. 18, pp. 16749-16757, 2019.

[3] Y. Van De Burgt *et al.*, "A non-volatile organic electrochemical device as a low-voltage artificial synapse for neuromorphic computing," *Nature materials,* vol. 16, no. 4, pp. 414-418, 2017.

[4] F. Molina-Lopez *et al.*, "Inkjet-printed stretchable and low voltage synaptic transistor array," *Nature communications,* vol. 10, no. 1, p. 2676, 2019.

[5] J. J. Hopfield, "Neural networks and physical systems with emergent collective computational abilities," *Proceedings of the national academy of sciences,* vol. 79, no. 8, pp. 2554-2558, 1982.

[6] Y. LeCun, Y. Bengio, and G. Hinton, "Deep learning," *nature,* vol. 521, no. 7553, pp. 436-444, 2015.

[7] L. F. Abbott and S. B. Nelson, "Synaptic plasticity: taming the beast," *Nature neuroscience,* vol. 3, no. 11, pp. 1178-1183, 2000.

[8] L. Merces, L. M. M. Ferro, A. Nawaz, and P. Sonar, "Advanced Neuromorphic Applications Enabled by Synaptic Ion-Gating Vertical Transistors," *Advanced Science,* p. 2305611, 2024.

[9] D. Simatos *et al.*, "Electrolyte-gated organic field-effect transistors with high operational stability and lifetime in practical electrolytes," *SmartMat,* p. e1291, 2024.

[10] E. R. Kandel, J. H. Schwartz, T. M. Jessell, S. Siegelbaum, A. J. Hudspeth, and S. Mack, *Principles of neural science*. McGraw-hill New York, 2000.

[11] D. Kim and J. S. Lee, "Neurotransmitter-induced excitatory and inhibitory functions in artificial synapses," *Advanced Functional Materials,* vol. 32, no. 21, p. 2200497, 2022.

[12] G. D. Spyropoulos, J. N. Gelinas, and D. Khodagholy, "Internal ion-gated organic electrochemical transistor: A building block for integrated bioelectronics," *Science advances,* vol. 5, no. 2, p. eaau7378, 2019.

[13] S. Y. Yeung, A. Veronica, Y. Li, and I. M. Hsing, "High-performance internal ion-gated organic electrochemical transistors for high-frequency bioimpedance analysis," *Advanced Materials Technologies,* vol. 8, no. 4, p. 2201116, 2023.

[14] A. Subramanian, *Metal Oxides for Ion-Gated Transistors*. Ecole Polytechnique, Montreal (Canada), 2021.

[15] L. C. da Silva Neres *et al.*, "Metal oxide ion-gated transistors: A perspective on in operando characterizations and emerging Li-ion-based applications," *MRS Communications,* vol. 13, no. 5, pp. 695-703, 2023.

[16] T. Lan, Z. Gao, M. S. Barbosa, and C. Santato, "Flexible ion-gated transistors making use of poly-3-hexylthiophene (P3HT): effect of the molecular weight on the effectiveness of gating and device performance," *Journal of Electronic Materials,* vol. 49, pp. 5302-5307, 2020.

[17] C. Cea, G. D. Spyropoulos, P. Jastrzebska-Perfect, J. J. Ferrero, J. N. Gelinas, and D. Khodagholy, "Enhancement-mode ion-based transistor as a comprehensive interface and real-time processing unit for in vivo electrophysiology," *Nature materials,* vol. 19, no. 6, pp. 679-686, 2020.

[18] M. S. Barbosa, N. Balke, W.-Y. Tsai, C. Santato, and M. O. Orlandi, "Structure of the electrical double layer at the interface between an ionic liquid and tungsten oxide in ion-gated transistors," *The Journal of Physical Chemistry Letters,* vol. 11, no. 9, pp. 3257-3262, 2020.

[19] X. Liu *et al.*, "Neuromorphic Nanoionics for Human–Machine Interaction: From Materials to Applications," *Advanced Materials,* p. 2311472, 2024.

[20] G. Liu, Y. Guo, and Y. Liu, "Design of ion-gated transistor materials at the molecular level," *Matter,* 2024.

[21] L. Xiang, L. Liu, F. Zhang, C. a. Di, and D. Zhu, "Ion-Gating Engineering of Organic Semiconductors toward Multifunctional Devices," *Advanced Functional Materials,* vol. 31, no. 32, p. 2102149, 2021.

[22] B. Qu, A. Younis, and D. Chu, "Recent progress in tungsten oxides based memristors and their neuromorphological applications," *Electronic Materials Letters,* vol. 12, pp. 715-731, 2016.

[23] M. Modak, S. Rane, and S. Jagtap, "WO3: a review of synthesis techniques, nanocomposite materials and their morphological effects for gas sensing application," *Bulletin of Materials Science,* vol. 46, no. 1, p. 28, 2023.

[24] H. G. Cragon, *Computer architecture and implementation*. Cambridge University Press, 2000.

[25] M. Sharad, C. Augustine, G. Panagopoulos, and K. Roy, "Proposal for neuromorphic hardware using spin devices," *arXiv preprint arXiv:1206.3227,* 2012.

[26] C. Mead, "Neuromorphic electronic systems," *Proceedings of the IEEE,* vol. 78, no. 10, pp. 1629-1636, 1990.

[27] W. Wang *et al.*, "Learning of spatiotemporal patterns in a spiking neural network with resistive switching synapses," *Science advances,* vol. 4, no. 9, p. eaat4752, 2018.

[28] P. Wang *et al.*, "Inversion of a large-scale circuit model reveals a cortical hierarchy in the dynamic resting human brain," *Science advances,* vol. 5, no. 1, p. eaat7854, 2019.

[29] Q. Xia and J. J. Yang, "Memristive crossbar arrays for brain-inspired computing," *Nature materials,* vol. 18, no. 4, pp. 309-323, 2019.

[30] X. Guo *et al.*, "Fast, energy-efficient, robust, and reproducible mixed-signal neuromorphic classifier based on embedded NOR flash memory technology," in *2017 IEEE International Electron Devices Meeting (IEDM)*, 2017: IEEE, pp. 6.5. 1-6.5. 4.

[31] J.-W. Jang, S. Park, G. W. Burr, H. Hwang, and Y.-H. Jeong, "Optimization of conductance change in Pr 1–x Ca x MnO 3-based synaptic devices for neuromorphic systems," *IEEE Electron Device Letters,* vol. 36, no. 5, pp. 457-459, 2015.

[32] D. Ham, H. Park, S. Hwang, and K. Kim, "Neuromorphic electronics based on copying and pasting the brain," *Nature Electronics,* vol. 4, no. 9, pp. 635-644, 2021.

[33] D. B. Strukov, G. S. Snider, D. R. Stewart, and R. S. Williams, "The missing memristor found," *nature,* vol. 453, no. 7191, pp. 80-83, 2008.

[34] D. Kuzum, S. Yu, and H. P. Wong, "Synaptic electronics: materials, devices and applications," *Nanotechnology,* vol. 24, no. 38, p. 382001, 2013.

[35] D. Ielmini and H.-S. P. Wong, "In-memory computing with resistive switching devices," *Nature electronics,* vol. 1, no. 6, pp. 333-343, 2018.

[36] W. Ou, S. Xiao, C. Zhu, W. Han, and Q. Zhang, "An overview of brain-like computing: Architecture, applications, and future trends," *Frontiers in neurorobotics,* vol. 16, p. 1041108, 2022.

[37] Y. Nie, T. Ren, and Z. Shi, "The developments and applications of brain-like computing chips," in *International Conference on Algorithms, Microchips and Network Applications*, 2022, vol. 12176: SPIE, pp. 272-285.

[38] I. Power, "750 and 760 Technical Overview and Introduction," ed: IBM, Somers, NY, USA, 2015.

[39] R. A. Nawrocki, R. M. Voyles, and S. E. Shaheen, "A mini review of neuromorphic architectures and implementations," *IEEE Transactions on Electron Devices,* vol. 63, no. 10, pp. 3819-3829, 2016.

[40] Y. Zhang *et al.*, "Brain-inspired computing with memristors: Challenges in devices, circuits, and systems," *Applied Physics Reviews,* vol. 7, no. 1, 2020.

[41] X. Zhang *et al.*, "An artificial spiking afferent nerve based on Mott memristors for neurorobotics," *Nature communications,* vol. 11, no. 1, p. 51, 2020.

[42] M. Zhao, B. Gao, J. Tang, H. Qian, and H. Wu, "Reliability of analog resistive switching memory for neuromorphic computing," *Applied Physics Reviews,* vol. 7, no. 1, 2020.

[43] Y. van De Burgt, A. Melianas, S. T. Keene, G. Malliaras, and A. Salleo, "Organic electronics for neuromorphic computing," *Nature Electronics,* vol. 1, no. 7, pp. 386-397, 2018.

[44] F. Cai *et al.*, "A fully integrated reprogrammable memristor–CMOS system for efficient multiply–accumulate operations," *Nature electronics*, vol. 2, no. 7, pp. 290-299, 2019.

[45] L. J. Edgar, "Method and apparatus for controlling electric currents," ed: Google Patents, 1930.

[46] S. William, "Circuit element utilizing semiconductive material," ed: Google Patents, 1951.

[47] W. Brattain and C. Garrett, "Experiments on the interface between germanium and an electrolyte," *Bell System Technical Journal*, vol. 34, no. 1, pp. 129-176, 1955.

[48] K. Dawon, "Electric field controlled semiconductor device," ed: Google Patents, 1963.

[49] J. W. Park, B. H. Kang, and H. J. Kim, "A review of low-temperature solution-processed metal oxide thin-film transistors for flexible electronics," *Advanced Functional Materials*, vol. 30, no. 20, p. 1904632, 2020.

[50] E. Fortunato, P. Barquinha, and R. Martins, "Oxide semiconductor thin-film transistors: a review of recent advances," *Advanced materials*, vol. 24, no. 22, pp. 2945-2986, 2012.

[51] D. K. Schroder, *Semiconductor material and device characterization*. John Wiley & Sons, 2015.

[52] W. E. Bradley, "The Surface-Barrier Transistor: Part I-Principles of the Surface-Barrier Transistor," *Proceedings of the IRE*, vol. 41, no. 12, pp. 1702-1706, 1953, doi: 10.1109/JRPROC.1953.274351.

[53] I. Kymissis, *Organic Field Effect Transistors: Theory, Fabrication and Characterization*. Springer Publishing Company, Incorporated, 2009.

[54] W. Bradley, "The surface-barrier transistor: Part I-Principles of the surface-barrier transistor," *Proceedings of the IRE*, vol. 41, no. 12, pp. 1702-1706, 1953.

[55] X. Tong, E. Ashalley, F. Lin, H. Li, and Z. M. Wang, "Advances in MoS 2-based field effect transistors (FETs)," *Nano-Micro Letters*, vol. 7, pp. 203-218, 2015.

[56] "Application to OLED Displays," in *Physics and Technology of Crystalline Oxide Semiconductor CAAC-IGZO*, 2016, pp. 183-305.

[57] S. Li and D. Chu, "A review of thin-film transistors/circuits fabrication with 3D self-aligned imprint lithography," *Flexible and Printed Electronics*, vol. 2, no. 1, p. 013002, 2017.

[58] H. Tan, "Advancements And Applications of Field-Effect Transistors in Modern Electronics," *Highlights in Science, Engineering and Technology*, vol. 81, pp. 318-322, 2024.

[59] S. Ono, S. Seki, R. Hirahara, Y. Tominari, and J. Takeya, "High-mobility, low-power, and fast-switching organic field-effect transistors with ionic liquids," *Applied Physics Letters*, vol. 92, no. 10, p. 103313, 2008, doi: 10.1063/1.2898203.

[60] X. Bu, H. Xu, D. Shang, Y. Li, H. Lv, and Q. Liu, "Ion-Gated Transistor: An Enabler for Sensing and Computing Integration," *Advanced Intelligent Systems*, vol. 2, no. 12, p. 2000156, 2020, doi: https://doi.org/10.1002/aisy.202000156.

[61] D. Wang, S. Zhao, R. Yin, L. Li, Z. Lou, and G. Shen, "Recent advanced applications of ion-gel in ionic-gated transistor," *npj Flexible Electronics,* vol. 5, no. 1, p. 13, 2021/06/14 2021, doi: 10.1038/s41528-021-00110-2.

[62] E. J. Fuller *et al.*, "Redox transistors for neuromorphic computing," *IBM Journal of Research and Development,* vol. 63, no. 6, pp. 9:1-9:9, 2019, doi: 10.1147/JRD.2019.2942285.

[63] L. Wu, H. Li, H. Chai, Q. Xu, Y. Chen, and L. Chen, "Anion-dependent molecular doping and charge transport in ferric salt-doped P3HT for thermoelectric application," *ACS Applied Electronic Materials,* vol. 3, no. 3, pp. 1252-1259, 2021.

[64] F.-Y. Yang, K.-J. Chang, M.-Y. Hsu, and C.-C. Liu, "High-performance poly (3-hexylthiophene) transistors with thermally cured and photo-cured PVP gate dielectrics," *Journal of Materials Chemistry,* vol. 18, no. 48, pp. 5927-5932, 2008.

[65] N. Chandrasekaran, A. Kumar, L. Thomsen, D. Kabra, and C. R. McNeill, "High performance as-cast P3HT: PCBM devices: understanding the role of molecular weight in high regioregularity P3HT," *Materials Advances,* vol. 2, no. 6, pp. 2045-2054, 2021.

[66] Z. Rahimzadeh, S. M. Naghib, Y. Zare, and K. Y. Rhee, "An overview on the synthesis and recent applications of conducting poly (3, 4-ethylenedioxythiophene)(PEDOT) in industry and biomedicine," *Journal of materials science,* vol. 55, pp. 7575-7611, 2020.

[67] Y. Zhang *et al.*, "Fiber organic electrochemical transistors based on multi-walled carbon nanotube and polypyrrole composites for noninvasive lactate sensing," *Analytical and Bioanalytical Chemistry,* vol. 412, pp. 7515-7524, 2020.

[68] A. L. Briseno, F. S. Kim, A. Babel, Y. Xia, and S. A. Jenekhe, "n-Channel polymer thin film transistors with long-term air-stability and durability and their use in complementary inverters," *Journal of Materials Chemistry,* vol. 21, no. 41, pp. 16461-16466, 2011.

[69] B. D. Paulsen and C. D. Frisbie, "Dependence of conductivity on charge density and electrochemical potential in polymer semiconductors gated with ionic liquids," *The Journal of Physical Chemistry C,* vol. 116, no. 4, pp. 3132-3141, 2012.

[70] R. Noriega *et al.*, "A general relationship between disorder, aggregation and charge transport in conjugated polymers," *Nature materials,* vol. 12, no. 11, pp. 1038-1044, 2013.

[71] A. M. Ballantyne *et al.*, "The effect of poly (3-hexylthiophene) molecular weight on charge transport and the performance of polymer: fullerene solar cells," *Advanced Functional Materials,* vol. 18, no. 16, pp. 2373-2380, 2008.

[72] A. G. Dixon, R. Visvanathan, N. A. Clark, N. Stingelin, N. Kopidakis, and S. E. Shaheen, "Molecular weight dependence of carrier mobility and recombination rate in neat P3HT films," *Journal of Polymer Science Part B: Polymer Physics,* vol. 56, no. 1, pp. 31-35, 2018.

[73] S. Mardi, M. Pea, A. Notargiacomo, N. Yaghoobi Nia, A. D. Carlo, and A. Reale, "The molecular weight dependence of thermoelectric properties of poly (3-hexylthiophene)," *Materials,* vol. 13, no. 6, p. 1404, 2020.

[74] T.-D. Nguyen *et al.*, "Molecular weight-dependent physical and photovoltaic properties of poly (3-alkylthiophene) s with butyl, hexyl, and octyl side-chains," *Polymers,* vol. 13, no. 19, p. 3440, 2021.

[75] D. Dong, W. Wang, C. Zhan, C. Li, Q. Zhou, and S. Xiao, "Effect of Molecular Weight on Thermoelectric Performance of P3HT Analogues with 2-Propoxyethyl Side Chains," *Journal of Wuhan University of Technology-Mater. Sci. Ed.,* vol. 39, no. 2, pp. 268-281, 2024.

[76] J. Y. Na, B. Kang, and Y. D. Park, "Influence of molecular weight on the solidification of a semiconducting polymer during time-controlled spin-coating," *The Journal of Physical Chemistry C,* vol. 123, no. 28, pp. 17102-17111, 2019.

[77] K. Banger *et al.*, "Low-temperature, high-performance solution-processed metal oxide thin-film transistors formed by a ‘sol–gel on chip’process," *Nature materials,* vol. 10, no. 1, pp. 45-50, 2011.

[78] K. Nomura, H. Ohta, A. Takagi, T. Kamiya, M. Hirano, and H. Hosono, "Room-temperature fabrication of transparent flexible thin-film transistors using amorphous oxide semiconductors," *nature,* vol. 432, no. 7016, pp. 488-492, 2004.

[79] L. Petti *et al.*, "Metal oxide semiconductor thin-film transistors for flexible electronics," *Applied Physics Reviews,* vol. 3, no. 2, 2016.

[80] D. J. Borah, A. T. T. Mostako, R. Chetia, S. Konwer, and M. Paul, "Tuning temperature-dependent microstructural properties of tungsten oxide thin films for acetone sensor," *Journal of Materials Science: Materials in Electronics,* vol. 33, no. 25, pp. 19854-19870, 2022.

[81] Y. Yao, D. Sang, L. Zou, Q. Wang, and C. Liu, "A review on the properties and applications of WO3 nanostructure-based optical and electronic devices," *Nanomaterials,* vol. 11, no. 8, p. 2136, 2021.

[82] M. Gillet, K. Aguir, C. Lemire, E. Gillet, and K. Schierbaum, "The structure and electrical conductivity of vacuum-annealed WO3 thin films," *Thin Solid Films,* vol. 467, no. 1, pp. 239-246, 2004/11/22/ 2004, doi: https://doi.org/10.1016/j.tsf.2004.04.018.

[83] R. S. Vemuri, K. K. Bharathi, S. K. Gullapalli, and C. V. Ramana, "Effect of structure and size on the electrical properties of nanocrystalline WO3 films," (in eng), *ACS Appl Mater Interfaces,* vol. 2, no. 9, pp. 2623-2628, 2010/09// 2010, doi: 10.1021/am1004514.

[84] J. Ortiz, D. Acosta, and C. Magaña, "Long-term cycling and stability of crystalline WO3 electrochromic thin films prepared by spray pyrolysis," *Journal of Solid State Electrochemistry,* vol. 26, no. 8, pp. 1667-1676, 2022.

[85] H. Zheng, J. Z. Ou, M. S. Strano, R. B. Kaner, A. Mitchell, and K. Kalantar-zadeh, "Nanostructured tungsten oxide–properties, synthesis, and applications," *Advanced Functional Materials,* vol. 21, no. 12, pp. 2175-2196, 2011.

[86] H. Li *et al.*, "Mesoporous WO3-TiO2 heterojunction for a hydrogen gas sensor," *Sensors and Actuators B: Chemical,* vol. 341, p. 130035, 2021.

[87] X. Meng *et al.*, "Electrolyte-gated WO3 transistors: electrochemistry, structure, and device performance," *The Journal of Physical Chemistry C*, vol. 119, no. 37, pp. 21732-21738, 2015.

[88] W. Huang *et al.*, "Dielectric materials for electrolyte gated transistor applications," *Journal of Materials Chemistry C*, vol. 9, no. 30, pp. 9348-9376, 2021.

[89] M. Freemantle, "An introduction to ionic liquids," (in English), 2010. [Online]. Available: http://www.books24x7.com/marc.asp?bookid=49978.

[90] T. Welton, "Room-Temperature Ionic Liquids. Solvents for Synthesis and Catalysis," (in eng), *Chem Rev*, vol. 99, no. 8, pp. 2071-2084, Aug 11 1999, doi: 10.1021/cr980032t.

[91] R. Hagiwara *et al.*, "Physicochemical properties of 1,3-dialkylimidazolium fluorohydrogenate room-temperature molten salts," (in English), *J. Electrochem. Soc.*, vol. 150, no. 12, pp. D195-D199, 2003, doi: 10.1149/1.1621414.

[92] D. A. Bernards and G. G. Malliaras, "Steady-state and transient behavior of organic electrochemical transistors," *Advanced Functional Materials*, vol. 17, no. 17, pp. 3538-3544, 2007.

[93] J. Rivnay, S. Inal, A. Salleo, R. M. Owens, M. Berggren, and G. G. Malliaras, "Organic electrochemical transistors," *Nature Reviews Materials*, vol. 3, no. 2, pp. 1-14, 2018.

[94] J. H. Cho, J. Lee, Y. He, B. Kim, T. P. Lodge, and C. D. Frisbie, "High-capacitance ion gel gate dielectrics with faster polarization response times for organic thin film transistors," *Advanced materials*, vol. 20, no. 4, pp. 686-690, 2008.

[95] Y. Dong *et al.*, "Plasticity of synaptic transmission in human stem cell-derived neural networks," *Iscience*, vol. 23, no. 2, 2020.

[96] A. Citri and R. C. Malenka, "Synaptic plasticity: multiple forms, functions, and mechanisms," *Neuropsychopharmacology*, vol. 33, no. 1, pp. 18-41, 2008.

[97] J. Leger, M. Berggren, and S. Carter, *Iontronics: Ionic carriers in organic electronic materials and devices*. CRC Press, 2016.

[98] P. Monalisha, A. P. Kumar, X. R. Wang, and S. Piramanayagam, "Emulation of synaptic plasticity on a cobalt-based synaptic transistor for neuromorphic computing," *ACS Applied Materials & Interfaces*, vol. 14, no. 9, pp. 11864-11872, 2022.

[99] L. Q. Zhu, C. J. Wan, L. Q. Guo, Y. Shi, and Q. Wan, "Artificial synapse network on inorganic proton conductor for neuromorphic systems," *Nature Communications*, vol. 5, no. 1, p. 3158, 2014, doi: 10.1038/ncomms4158.

[100] P. Gkoupidenis, N. Schaefer, X. Strakosas, J. A. Fairfield, and G. G. Malliaras, "Synaptic plasticity functions in an organic electrochemical transistor," *Applied Physics Letters*, vol. 107, no. 26, 2015.

[101] J. Y. Gerasimov *et al.*, "An evolvable organic electrochemical transistor for neuromorphic applications," *Advanced Science*, vol. 6, no. 7, p. 1801339, 2019.

[102] X. Liu, D. Li, Y. Wang, D. Yang, and X. Pi, "Flexible optoelectronic synaptic transistors for neuromorphic visual systems," *APL Machine Learning*, vol. 1, no. 3, 2023.

[103] J. H. Baek *et al.*, "Two-terminal lithium-mediated artificial synapses with enhanced weight modulation for feasible hardware neural networks," *Nano-Micro Letters*, vol. 15, no. 1, p. 69, 2023.

[104] C. A. Lea-Carnall, N. J. Trujillo-Barreto, M. A. Montemurro, W. El-Deredy, and L. M. Parkes, "Evidence for frequency-dependent cortical plasticity in the human brain," *Proceedings of the National Academy of Sciences*, vol. 114, no. 33, pp. 8871-8876, 2017.

[105] N. Du *et al.*, "Synaptic plasticity in memristive artificial synapses and their robustness against noisy inputs," *Frontiers in neuroscience*, vol. 15, p. 660894, 2021.

[106] N. Garg *et al.*, "Voltage-dependent synaptic plasticity: Unsupervised probabilistic Hebbian plasticity rule based on neurons membrane potential," *Frontiers in Neuroscience*, vol. 16, p. 983950, 2022.

[107] T. Lan, Z. Gao, M. S. Barbosa, and C. Santato, "Flexible Ion-Gated Transistors Making Use of Poly-3-hexylthiophene (P3HT): Effect of the Molecular Weight on the Effectiveness of Gating and Device Performance," *Journal of Electronic Materials*, vol. 49, no. 9, pp. 5302-5307, 2020/09/01 2020, doi: 10.1007/s11664-020-08242-3.

[108] Y. Diao, L. Shaw, Z. Bao, and S. C. Mannsfeld, "Morphology control strategies for solution-processed organic semiconductor thin films," *Energy & Environmental Science*, vol. 7, no. 7, pp. 2145-2159, 2014.

[109] C. Santato, M. Odziemkowski, M. Ulmann, and J. Augustynski, "Crystallographically oriented mesoporous WO3 films: synthesis, characterization, and applications," *Journal of the American Chemical Society*, vol. 123, no. 43, pp. 10639-10649, 2001.

[110] M. C. Buzzeo, R. G. Evans, and R. G. Compton, "Non-haloaluminate room-temperature ionic liquids in electrochemistry—A review," *ChemPhysChem*, vol. 5, no. 8, pp. 1106-1120, 2004.

[111] I. Valitova, P. Kumar, X. Meng, F. Soavi, C. Santato, and F. Cicoira, "Photolithographically patterned TiO2 films for electrolyte-gated transistors," *ACS applied materials & interfaces*, vol. 8, no. 23, pp. 14855-14862, 2016.

[112] D. Measured, "Provided by IoLiTec Ionic Liquids Technologies GmbH," *Heilbronn/Germany*, 2012.

[113] A. Subramanian *et al.*, "Ion-gated transistors based on porous and compact TiO2 films: Effect of Li ions in the gating medium," *AIP Advances*, vol. 10, no. 6, 2020.

[114] R. K. Azari, Z. Gao, A. Carrière, and C. Santato, "Exploring response time and synaptic plasticity in P3HT ion-gated transistors for neuromorphic computing: impact of P3HT molecular weight and film thickness," *RSC Applied Interfaces*, vol. 1, no. 3, pp. 564-572, 2024.

[115] R. K. Azari, T. Lan, and C. Santato, "On the factors affecting the response time of synaptic ion-gated transistors," *Journal of Materials Chemistry C*, 10.1039/D3TC00161J 2023, doi: 10.1039/D3TC00161J.

[116] D. K. Gosser, *Cyclic voltammetry: simulation and analysis of reaction mechanisms*. VCH New York, 1993.

[117] A. J. Bard and L. R. Faulkner, "Electrochemical methods: fundamentals and applications," *Surf. Technol*, vol. 20, no. 1, pp. 91-92, 1983.

[118] G. Binnig, C. F. Quate, and C. Gerber, "Atomic force microscope," *Physical review letters,* vol. 56, no. 9, p. 930, 1986.

[119] A. R. Harris, D. B. Grayden, and S. E. John, "Electrochemistry in a two-or three-electrode configuration to understand monopolar or bipolar configurations of platinum bionic implants," *Micromachines,* vol. 14, no. 4, p. 722, 2023.

[120] S. Mundinamani and M. Rabinal, "Cyclic voltammetric studies on the role of electrode, electrode surface modification and electrolyte solution of an electrochemical cell," *J. Appl. Chem,* vol. 7, no. 9, pp. 45-52, 2014.

[121] M. Voelker and P. Fromherz, "Signal Transmission from Individual Mammalian Nerve Cell to Field-Effect Transistor," *Small,* vol. 1, no. 2, pp. 206-210, 2005, doi: https://doi.org/10.1002/smll.200400077.

[122] J. J. Jun *et al.*, "Fully integrated silicon probes for high-density recording of neural activity," (in eng), *Nature,* vol. 551, no. 7679, pp. 232-236, Nov 8 2017, doi: 10.1038/nature24636.

[123] C. G. Bischak *et al.*, "A Reversible Structural Phase Transition by Electrochemical Ion Injection into a Conjugated Polymer," *arXiv preprint arXiv:1910.06440,* 2019.

[124] M. Berggren and A. Richter-Dahlfors, "Organic bioelectronics," *Advanced Materials,* vol. 19, no. 20, pp. 3201-3213, 2007.

[125] J. Rivnay, R. M. Owens, and G. G. Malliaras, "The rise of organic bioelectronics," *Chemistry of Materials,* vol. 26, no. 1, pp. 679-685, 2014.

[126] D. Moia *et al.*, "Design and evaluation of conjugated polymers with polar side chains as electrode materials for electrochemical energy storage in aqueous electrolytes," *Energy & Environmental Science,* vol. 12, no. 4, pp. 1349-1357, 2019.

[127] I. E. Jacobs and A. J. Moulé, "Controlling molecular doping in organic semiconductors," *Advanced Materials,* vol. 29, no. 42, p. 1703063, 2017.

[128] H. Yuan, H. Shimotani, A. Tsukazaki, A. Ohtomo, M. Kawasaki, and Y. Iwasa, "High-density carrier accumulation in ZnO field-effect transistors gated by electric double layers of ionic liquids," *Advanced Functional Materials,* vol. 19, no. 7, pp. 1046-1053, 2009.

[129] X. Bu, H. Xu, D. Shang, Y. Li, H. Lv, and Q. Liu, "Ion-gated transistor: An enabler for sensing and computing integration," *Advanced Intelligent Systems,* vol. 2, no. 12, p. 2000156, 2020.

[130] D. Wang, V. Noël, and B. Piro, "Electrolytic gated organic field-effect transistors for application in biosensors—A Review," *Electronics,* vol. 5, no. 1, p. 9, 2016.

[131] K. Ueno *et al.*, "Electric-field-induced superconductivity in an insulator," *Nature materials,* vol. 7, no. 11, pp. 855-858, 2008.

[132] J. Rivnay, S. Inal, A. Salleo, R. M. Owens, M. Berggren, and G. G. Malliaras, "Organic electrochemical transistors," *Nature Reviews Materials,* vol. 3, no. 2, p. 17086, 2018/01/16 2018, doi: 10.1038/natrevmats.2017.86.

[133] M. J. Panzer and C. D. Frisbie, "Exploiting ionic coupling in electronic devices: electrolyte-gated organic field-effect transistors," *Advanced Materials,* vol. 20, no. 16, pp. 3177-3180, 2008.

[134] P. Hapiot and C. Lagrost, "Electrochemical reactivity in room-temperature ionic liquids," *Chemical reviews,* vol. 108, no. 7, pp. 2238-2264, 2008.

[135] A. Laiho, L. Herlogsson, R. Forchheimer, X. Crispin, and M. Berggren, "Controlling the dimensionality of charge transport in organic thin-film transistors," *Proceedings of the National Academy of Sciences,* vol. 108, no. 37, pp. 15069-15073, 2011.

[136] M. Zakrewsky *et al.*, "Ionic liquids as a class of materials for transdermal delivery and pathogen neutralization," *Proceedings of the National Academy of Sciences,* vol. 111, no. 37, pp. 13313-13318, 2014.

[137] T.-H. Le, Y. Kim, and H. Yoon, "Electrical and electrochemical properties of conducting polymers," *Polymers,* vol. 9, no. 4, p. 150, 2017.

[138] H. Shimotani, H. Asanuma, J. Takeya, and Y. Iwasa, "Electrolyte-gated charge accumulation in organic single crystals," *Applied Physics Letters,* vol. 89, no. 20, p. 203501, 2006.

[139] R. Giridharagopal *et al.*, "Electrochemical strain microscopy probes morphology-induced variations in ion uptake and performance in organic electrochemical transistors," *Nature materials,* vol. 16, no. 7, pp. 737-742, 2017.

[140] Y. Xia, J. H. Cho, J. Lee, P. P. Ruden, and C. D. Frisbie, "Comparison of the mobility–carrier density relation in polymer and single-crystal organic transistors employing vacuum and liquid gate dielectrics," *Advanced Materials,* vol. 21, no. 21, pp. 2174-2179, 2009.

[141] J. O. Guardado and A. Salleo, "Structural Effects of Gating Poly (3-hexylthiophene) through an Ionic Liquid," *Advanced Functional Materials,* vol. 27, no. 32, p. 1701791, 2017.

[142] E. M. Thomas, M. A. Brady, H. Nakayama, B. C. Popere, R. A. Segalman, and M. L. Chabinyc, "X-Ray Scattering Reveals Ion-Induced Microstructural Changes During Electrochemical Gating of Poly (3-Hexylthiophene)," *Advanced Functional Materials,* vol. 28, no. 44, p. 1803687, 2018.

[143] V. Kaphle, S. Liu, A. Al-Shadeedi, C. M. Keum, and B. Lüssem, "Contact resistance effects in highly doped organic electrochemical transistors," *Advanced Materials,* vol. 28, no. 39, pp. 8766-8770, 2016.

[144] K. Izutsu, *Electrochemistry in nonaqueous solutions*. John Wiley & Sons, 2009.

[145] L. Kergoat *et al.*, "A water-gate organic field-effect transistor," *Advanced Materials,* vol. 22, no. 23, pp. 2565-2569, 2010.

[146] M. J. Earle *et al.*, "The distillation and volatility of ionic liquids," *Nature,* vol. 439, no. 7078, pp. 831-834, 2006.

[147] J. H. Cho, J. Lee, Y. He, B. S. Kim, T. P. Lodge, and C. D. Frisbie, "High-Capacitance Ion Gel Gate Dielectrics with Faster Polarization Response Times for Organic Thin Film Transistors," *Advanced Materials,* vol. 20, no. 4, pp. 686-690, 2008, doi: https://doi.org/10.1002/adma.200701069.

[148] S. L. Jackman and W. G. Regehr, "The mechanisms and functions of synaptic facilitation," *Neuron,* vol. 94, no. 3, pp. 447-464, 2017.

[149] L. F. Abbott and W. G. Regehr, "Synaptic computation," *Nature,* vol. 431, no. 7010, pp. 796-803, 2004/10/01 2004, doi: 10.1038/nature03010.

[150] M. A. Lynch, "Long-term potentiation and memory," *Physiological reviews,* vol. 84, no. 1, pp. 87-136, 2004.

[151] E. M. Thomas, B. C. Popere, H. Fang, M. L. Chabinyc, and R. A. Segalman, "Role of disorder induced by doping on the thermoelectric properties of semiconducting polymers," *Chemistry of Materials,* vol. 30, no. 9, pp. 2965-2972, 2018.

[152] B. C. Popere *et al.*, "Photocrosslinking polymeric ionic liquids via anthracene cycloaddition for organic electronics," *Journal of Materials Chemistry C,* vol. 6, no. 32, pp. 8762-8769, 2018.

[153] L.-a. Kong *et al.*, "Long-term synaptic plasticity simulated in ionic liquid/polymer hybrid electrolyte gated organic transistors," *Organic Electronics,* vol. 47, pp. 126-132, 2017.

[154] C. Qian, L.-a. Kong, J. Yang, Y. Gao, and J. Sun, "Multi-gate organic neuron transistors for spatiotemporal information processing," *Applied Physics Letters,* vol. 110, no. 8, p. 083302, 2017.

[155] P. Gkoupidenis, N. Schaefer, B. Garlan, and G. G. Malliaras, "Neuromorphic functions in PEDOT: PSS organic electrochemical transistors," *Advanced Materials,* vol. 27, no. 44, pp. 7176-7180, 2015.

[156] C. Qian, J. Sun, L. Zhang, H. Huang, J. Yang, and Y. Gao, "Crystal-Domain Orientation and Boundary in Highly Ordered Organic Semiconductor Thin Film," *The Journal of Physical Chemistry C,* vol. 119, no. 27, pp. 14965-14971, 2015/07/09 2015, doi: 10.1021/acs.jpcc.5b03727.

[157] D. Rawlings, E. M. Thomas, R. A. Segalman, and M. L. Chabinyc, "Controlling the Doping Mechanism in Poly(3-hexylthiophene) Thin-Film Transistors with Polymeric Ionic Liquid Dielectrics," *Chemistry of Materials,* vol. 31, no. 21, pp. 8820-8829, 2019/11/12 2019, doi: 10.1021/acs.chemmater.9b02803.

[158] C. D. Schuman, S. R. Kulkarni, M. Parsa, J. P. Mitchell, P. Date, and B. Kay, "Opportunities for neuromorphic computing algorithms and applications," *Nature Computational Science,* vol. 2, no. 1, pp. 10-19, 2022/01/01 2022, doi: 10.1038/s43588-021-00184-y.

[159] K. Sun, J. Chen, and X. Yan, "The Future of Memristors: Materials Engineering and Neural Networks," *Advanced Functional Materials,* vol. 31, no. 8, p. 2006773, 2021, doi: https://doi.org/10.1002/adfm.202006773.

[160] Y. Zhang *et al.*, "A system hierarchy for brain-inspired computing," *Nature,* vol. 586, no. 7829, pp. 378-384, 2020/10/01 2020, doi: 10.1038/s41586-020-2782-y.

[161] X. Zou, S. Xu, X. Chen, L. Yan, and Y. Han, "Breaking the von Neumann bottleneck: architecture-level processing-in-memory technology," *Science China Information Sciences,* vol. 64, no. 6, p. 160404, 2021/04/27 2021, doi: 10.1007/s11432-020-3227-1.

[162] Y. Yang, P. Gao, S. Gaba, T. Chang, X. Pan, and W. Lu, "Observation of conducting filament growth in nanoscale resistive memories," *Nature communications,* vol. 3, no. 1, p. 732, 2012.

[163] Y. Yang, X. Zhang, L. Qin, Q. Zeng, X. Qiu, and R. Huang, "Probing nanoscale oxygen ion motion in memristive systems," *Nature communications,* vol. 8, no. 1, p. 15173, 2017.

[164] A. Wedig *et al.*, "Nanoscale cation motion in TaO x, HfO x and TiO x memristive systems," *Nature nanotechnology,* vol. 11, no. 1, pp. 67-74, 2016.

[165] P. Sheridan and F. Cai, "C. du, W. Ma, Z. Zhang, WD Lu, Sparse coding with memristor networks," *Nat. Nanotechnol,* vol. 12, pp. 784-789, 2017.

[166] P. Yao *et al.*, "Face classification using electronic synapses," *Nature communications,* vol. 8, no. 1, p. 15199, 2017.

[167] C. Li *et al.*, "Analogue signal and image processing with large memristor crossbars," *Nature electronics,* vol. 1, no. 1, pp. 52-59, 2018.

[168] S. Kim, C. Du, P. Sheridan, W. Ma, S. Choi, and W. D. Lu, "Experimental demonstration of a second-order memristor and its ability to biorealistically implement synaptic plasticity," *Nano letters,* vol. 15, no. 3, pp. 2203-2211, 2015.

[169] S. Yamamoto, A. G. Polyravas, S. Han, and G. G. Malliaras, "Correlation between Transient Response and Neuromorphic Behavior in Organic Electrochemical Transistors," *Advanced Electronic Materials,* vol. 8, no. 4, p. 2101186, 2022, doi: https://doi.org/10.1002/aelm.202101186.

[170] J. Y. Gerasimov *et al.*, "A Biomimetic Evolvable Organic Electrochemical Transistor," *Advanced Electronic Materials,* vol. 7, no. 11, p. 2001126, 2021, doi: https://doi.org/10.1002/aelm.202001126.

[171] Y.-T. Yang, H.-C. Tien, C.-C. Chueh, and W.-Y. Lee, "Polymer synaptic transistors from memory to neuromorphic computing," *Materials Chemistry and Physics,* vol. 287, p. 126263, 2022/08/01/ 2022, doi: https://doi.org/10.1016/j.matchemphys.2022.126263.

[172] Z. Wang *et al.*, "Signal Filtering Enabled by Spike Voltage-Dependent Plasticity in Metalloporphyrin-Based Memristors," *Advanced Materials,* vol. 33, no. 43, p. 2104370, 2021, doi: https://doi.org/10.1002/adma.202104370.

[173] G.-T. Go *et al.*, "Achieving microstructure-controlled synaptic plasticity and long-term retention in ion-gel-gated organic synaptic transistors," *Advanced Intelligent Systems,* vol. 2, no. 11, p. 2000012, 2020.

[174] S. Wang *et al.*, "An organic electrochemical transistor for multi-modal sensing, memory and processing," *Nature Electronics,* vol. 6, no. 4, pp. 281-291, 2023.

[175] R. Karimi Azari, T. Lan, and C. Santato, "On the factors affecting the response time of synaptic ion-gated transistors," *Journal of Materials Chemistry C,* 10.1039/D3TC00161J vol. 11, no. 24, pp. 8293-8299, 2023, doi: 10.1039/D3TC00161J.

[176] R. S. Zucker and W. G. Regehr, "Short-term synaptic plasticity," *Annual review of physiology,* vol. 64, no. 1, pp. 355-405, 2002.

[177] D. E. Clapham, "Calcium signaling," *Cell,* vol. 131, no. 6, pp. 1047-1058, 2007.

[178] D. A. Bernards and G. G. Malliaras, "Steady-State and Transient Behavior of Organic Electrochemical Transistors," *Advanced Functional Materials,* vol. 17, no. 17, pp. 3538-3544, 2007, doi: https://doi.org/10.1002/adfm.200601239.

[179] N. M. B. Neto, M. D. Silva, P. T. Araujo, and R. N. Sampaio, "Photoinduced Self-Assembled Nanostructures and Permanent Polaron Formation in Regioregular Poly (3-hexylthiophene)," *Advanced Materials,* vol. 30, no. 16, p. 1705052, 2018.

[180] Z. Chiguvare and J. Parisi, "Current conduction in poly (3-Hexylthiophene) and in poly (3-hexylthiophene) doped [6, 6]-phenyl C61-butyric acid methylester composite thin film devices," *Zeitschrift für Naturforschung A,* vol. 67, no. 10-11, pp. 589-600, 2012.

[181] A. Nawaz, A. Kumar, and I. A. Hümmelgen, "Ultra-high mobility in defect-free poly (3-hexylthiophene-2, 5-diyl) field-effect transistors through supra-molecular alignment," *Organic Electronics,* vol. 51, pp. 94-102, 2017.

[182] A. Salleo, "Charge transport in polymeric transistors," *Materials today,* vol. 10, no. 3, pp. 38-45, 2007.

[183] L. Hrostea, M. Girtan, R. Mallet, and L. Leontie, "Optical and morphological properties of P3HT and P3HT: PCBM thin films used in photovoltaic applications," in *IOP Conference Series: Materials Science and Engineering*, 2018, vol. 374, no. 1: IOP Publishing, p. 012015.

[184] N. E. Persson, P.-H. Chu, M. McBride, M. Grover, and E. Reichmanis, "Nucleation, growth, and alignment of poly (3-hexylthiophene) nanofibers for high-performance OFETs," *Accounts of Chemical Research,* vol. 50, no. 4, pp. 932-942, 2017.

[185] R. J. Kline, M. D. McGehee, E. N. Kadnikova, J. Liu, and J. M. J. Fréchet, "Controlling the Field-Effect Mobility of Regioregular Polythiophene by Changing the Molecular Weight," *Advanced Materials,* vol. 15, no. 18, pp. 1519-1522, 2003, doi: https://doi.org/10.1002/adma.200305275.

[186] C. Goh, R. J. Kline, M. D. McGehee, E. N. Kadnikova, and J. M. Fréchet, "Molecular-weight-dependent mobilities in regioregular poly (3-hexyl-thiophene) diodes," *Applied Physics Letters,* vol. 86, no. 12, p. 122110, 2005.

[187] O. G. Reid *et al.*, "The influence of solid-state microstructure on the origin and yield of long-lived photogenerated charge in neat semiconducting polymers," *Journal of Polymer Science Part B: Polymer Physics,* vol. 50, no. 1, pp. 27-37, 2012.

[188] H. Yang, T. Joo Shin, Z. Bao, and C. Y. Ryu, "Structural transitions of nanocrystalline domains in regioregular poly (3-hexyl thiophene) thin films," *Journal of Polymer Science Part B: Polymer Physics,* vol. 45, no. 11, pp. 1303-1312, 2007.

[189] L. H. Jimison, S. Himmelberger, D. T. Duong, J. Rivnay, M. F. Toney, and A. Salleo, "Vertical confinement and interface effects on the microstructure and charge transport of P3HT thin films," *Journal of Polymer Science Part B: Polymer Physics,* vol. 51, no. 7, pp. 611-620, 2013, doi: https://doi.org/10.1002/polb.23265.

[190] S. Joshi, S. Grigorian, and U. Pietsch, "X-ray structural and crystallinity studies of low and high molecular weight poly (3-hexylthiophene)," *Physica status solidi (a),* vol. 205, no. 3, pp. 488-496, 2008.

[191] W. Porzio, G. Scavia, L. Barba, G. Arrighetti, and S. Milita, "Depth-resolved molecular structure and orientation of polymer thin films by synchrotron X-ray diffraction," *European polymer journal,* vol. 47, no. 3, pp. 273-283, 2011.

[192] S. Joshi *et al.*, "Thickness dependence of the crystalline structure and hole mobility in thin films of low molecular weight poly (3-hexylthiophene)," *Macromolecules,* vol. 41, no. 18, pp. 6800-6808, 2008.

[193] J. Rivnay *et al.*, "High-performance transistors for bioelectronics through tuning of channel thickness," *Science Advances,* vol. 1, no. 4, p. e1400251, 2015, doi: doi:10.1126/sciadv.1400251.

[194] S. Ludwigs, *P3HT revisited-from molecular scale to solar cell devices*. Springer, 2014.

[195] C. Poelking, K. Daoulas, A. Troisi, and D. Andrienko, "Morphology and charge transport in P3HT: a theorist's perspective," *P3HT Revisited–From Molecular Scale to Solar Cell Devices,* pp. 139-180, 2014.

[196] A. M. Ballantyne *et al.*, "The Effect of Poly(3-hexylthiophene) Molecular Weight on Charge Transport and the Performance of Polymer:Fullerene Solar Cells," *Advanced Functional Materials,* vol. 18, no. 16, pp. 2373-2380, 2008, doi: https://doi.org/10.1002/adfm.200800145.

[197] N. Zins, Y. Zhang, C. Yu, and H. An, "Neuromorphic Computing: A Path to Artificial Intelligence Through Emulating Human Brains," in *Frontiers of Quality Electronic Design (QED): AI, IoT and Hardware Security*, A. Iranmanesh Ed. Cham: Springer International Publishing, 2023, pp. 259-296.

[198] D. Ivanov, A. Chezhegov, and D. Larionov, "Neuromorphic artificial intelligence systems," *Frontiers in Neuroscience,* vol. 16, p. 959626, 2022.

[199] M. Dragoman and D. Dragoman, "Neuromorphic Computation," in *Atomic-Scale Electronics Beyond CMOS*. Cham: Springer International Publishing, 2021, pp. 187-213.

[200] S. Choi, J. Yang, and G. Wang, "Emerging Memristive Artificial Synapses and Neurons for Energy-Efficient Neuromorphic Computing," *Advanced Materials,* vol. 32, no. 51, p. 2004659, 2020, doi: https://doi.org/10.1002/adma.202004659.

[201] D. Marković, A. Mizrahi, D. Querlioz, and J. Grollier, "Physics for neuromorphic computing," *Nature Reviews Physics,* vol. 2, no. 9, pp. 499-510, 2020/09/01 2020, doi: 10.1038/s42254-020-0208-2.

[202] M. Zolfagharinejad, U. Alegre-Ibarra, T. Chen, S. Kinge, and W. G. van der Wiel, "Brain-inspired computing systems: a systematic literature review," *The European Physical Journal B,* vol. 97, no. 6, p. 70, 2024.

[203] S. Reardon, "Artificial neurons compute faster than the human brain," *Nature,* vol. 26, 2018.

[204] A. J. Edwards, G. Krylov, J. S. Friedman, and E. G. Friedman, "Harnessing stochasticity for superconductive multi-layer spike-rate-coded neuromorphic networks," *Neuromorphic Computing and Engineering,* vol. 4, no. 1, p. 014005, 2024.

[205] Y. Sun, H. Wang, and D. Xie, "Recent Advance in Synaptic Plasticity Modulation Techniques for Neuromorphic Applications," *Nano-Micro Letters,* vol. 16, no. 1, p. 211, 2024/06/06 2024, doi: 10.1007/s40820-024-01445-x.

[206] K. Roy, A. Jaiswal, and P. Panda, "Towards spike-based machine intelligence with neuromorphic computing," *Nature,* vol. 575, no. 7784, pp. 607-617, 2019.

[207] H. Han, H. Yu, H. Wei, J. Gong, and W. Xu, "Recent progress in three-terminal artificial synapses: from device to system," *Small,* vol. 15, no. 32, p. 1900695, 2019.

[208] S. Jiang, S. Nie, Y. He, R. Liu, C. Chen, and Q. Wan, "Emerging synaptic devices: from two-terminal memristors to multiterminal neuromorphic transistors," *Materials Today Nano,* vol. 8, p. 100059, 2019.

[209] K.-T. Chen and J.-S. Chen, "Perspective on oxide-based three-terminal artificial synapses in physical neural networks," *Applied Physics Letters,* vol. 121, no. 19, 2022.

[210] G. Li, M. Dai, and Y. Zhang, "Multi-Terminal Artificial Synaptic Devices with More Controllable Brain-Like Spike-Based Behaviors," *Advanced Electronic Materials,* vol. 8, no. 7, p. 2101003, 2022.

[211] Y. Park, M.-K. Kim, and J.-S. Lee, "Ion-gating synaptic transistors with long-term synaptic weight modulation," *Journal of Materials Chemistry C,* vol. 9, no. 16, pp. 5396-5402, 2021.

[212] X. Li *et al.,* "Multi-terminal ionic-gated low-power silicon nanowire synaptic transistors with dendritic functions for neuromorphic systems," *Nanoscale,* vol. 12, no. 30, pp. 16348-16358, 2020.

[213] P. Subin, A. Asha, K. Saji, and M. Jayaraj, "Spike-dependent plasticity modulation in TiO2-based synaptic device," *Journal of Materials Science: Materials in Electronics,* vol. 32, no. 10, pp. 13051-13061, 2021.

[214] R. K. Azari, Z. Gao, A. Carrière, and C. Santato, "Exploring Response Time and Synaptic Plasticity in P3HT Ion-Gated Transistors for Neuromorphic Computing: Impact of P3HT Molecular Weight and Film Thickness," *RSC Applied Interfaces,* 2024.

[215] K. Hadiyal, R. Ganesan, A. Rastogi, and R. Thamankar, "Bio-inspired artificial synapse for neuromorphic computing based on NiO nanoparticle thin film," *Scientific Reports,* vol. 13, no. 1, p. 7481, 2023.

[216] C. G. Granqvist, "Electrochromic tungsten oxide films: review of progress 1993–1998," *Solar Energy Materials and Solar Cells,* vol. 60, no. 3, pp. 201-262, 2000.

[217] A. Ponzoni *et al.*, "Ultrasensitive and highly selective gas sensors using three-dimensional tungsten oxide nanowire networks," *Applied Physics Letters,* vol. 88, no. 20, 2006.

[218] Y. Li *et al.*, "Metal oxide ion gated transistors based sensors," *Science China Technological Sciences,* vol. 67, no. 4, pp. 1040-1060, 2024.

[219] G. V. D. O. Silva *et al.*, "Tungsten oxide ion-gated phototransistors using ionic liquid and aqueous gating media," *Journal of Physics D: Applied Physics,* vol. 52, no. 30, p. 305102, 2019.

[220] J. R. H. Garza *et al.*, "A study of the doping process in Li 4 Ti 5 O 12 and TiO 2 battery electrode materials studied in the ion-gated transistor configuration," *Journal of Materials Chemistry C,* vol. 12, no. 7, pp. 2416-2422, 2024.

[221] Y. Cui, Q. Wang, G. Yang, and Y. Gao, "Electronic properties, optical properties and diffusion behavior of WO3 with H+, Li+ and Na+ intercalated ions: A first-principles study," *Journal of Solid State Chemistry,* vol. 297, p. 122082, 2021.

[222] J. T. Yang *et al.*, "Artificial synapses emulated by an electrolyte-gated tungsten-oxide transistor," *Advanced Materials,* vol. 30, no. 34, p. 1801548, 2018.

[223] B. Park *et al.*, "Robust 2D MoS2 artificial synapse device based on a lithium silicate solid electrolyte for high-precision analogue neuromorphic computing," *ACS Applied Materials & Interfaces,* vol. 14, no. 47, pp. 53038-53047, 2022.

[224] R. D. Nikam, M. Kwak, J. Lee, K. G. Rajput, and H. Hwang, "Controlled ionic tunneling in lithium nanoionic synaptic transistor through atomically thin graphene layer for neuromorphic computing," *Advanced Electronic Materials,* vol. 6, no. 2, p. 1901100, 2020.

[225] E. J. Fuller *et al.*, "Li-ion synaptic transistor for low power analog computing," *Advanced Materials,* vol. 29, no. SAND-2017-0895J, 2016.

[226] J. Zhou, C. Wan, L. Zhu, Y. Shi, and Q. Wan, "Synaptic behaviors mimicked in flexible oxide-based transistors on plastic substrates," *IEEE electron device letters,* vol. 34, no. 11, pp. 1433-1435, 2013.

[227] K. Liang *et al.*, "Engineering the interlayer spacing by pre-intercalation for high performance supercapacitor MXene electrodes in room temperature ionic liquid," *Advanced Functional Materials,* vol. 31, no. 33, p. 2104007, 2021.

[228] N. Agmon, "Isoelectronic theory for cationic radii," *Journal of the American Chemical Society,* vol. 139, no. 42, pp. 15068-15073, 2017.

[229] J. M. Black *et al.*, "Fundamental aspects of electric double layer force-distance measurements at liquid-solid interfaces using atomic force microscopy," *Scientific reports,* vol. 6, no. 1, p. 32389, 2016.

[230] J. Sayago, F. Soavi, Y. Sivalingam, F. Cicoira, and C. Santato, "Low voltage electrolyte-gated organic transistors making use of high surface area activated carbon gate electrodes," *Journal of Materials Chemistry C,* vol. 2, no. 28, pp. 5690-5694, 2014.

[231] Y. Na and F. S. Kim, "Nanodroplet-embedded semiconducting polymer layers for electrochemically stable and high-conductance organic electrolyte-gated transistors," *Chemistry of Materials,* vol. 31, no. 13, pp. 4759-4768, 2019.

[232] Y. Xia, J. Cho, B. Paulsen, C. D. Frisbie, and M. J. Renn, "Correlation of on-state conductance with referenced electrochemical potential in ion gel gated polymer transistors," *Applied Physics Letters,* vol. 94, no. 1, 2009.

# APPENDIX A SUPPORTING INFORMATION ARTICLE 1

## ON THE FACTORS AFFECTING THE RESPONSE TIME OF SYNAPTIC ION-GATED TRANSISTORS

Ramin Karimi Azari*[a], Tian Lan[a], Clara Santato*[a]

[a] Engineering Physics, Polytechnique Montreal, 2500 Ch. Polytechnique, H3T 1J4, Montreal, QC, Canada

Corresponding authors: ramin.karimi@polymtl.ca, clara.santato@polymtl.ca

**Morphology and structure of the P3HT films**

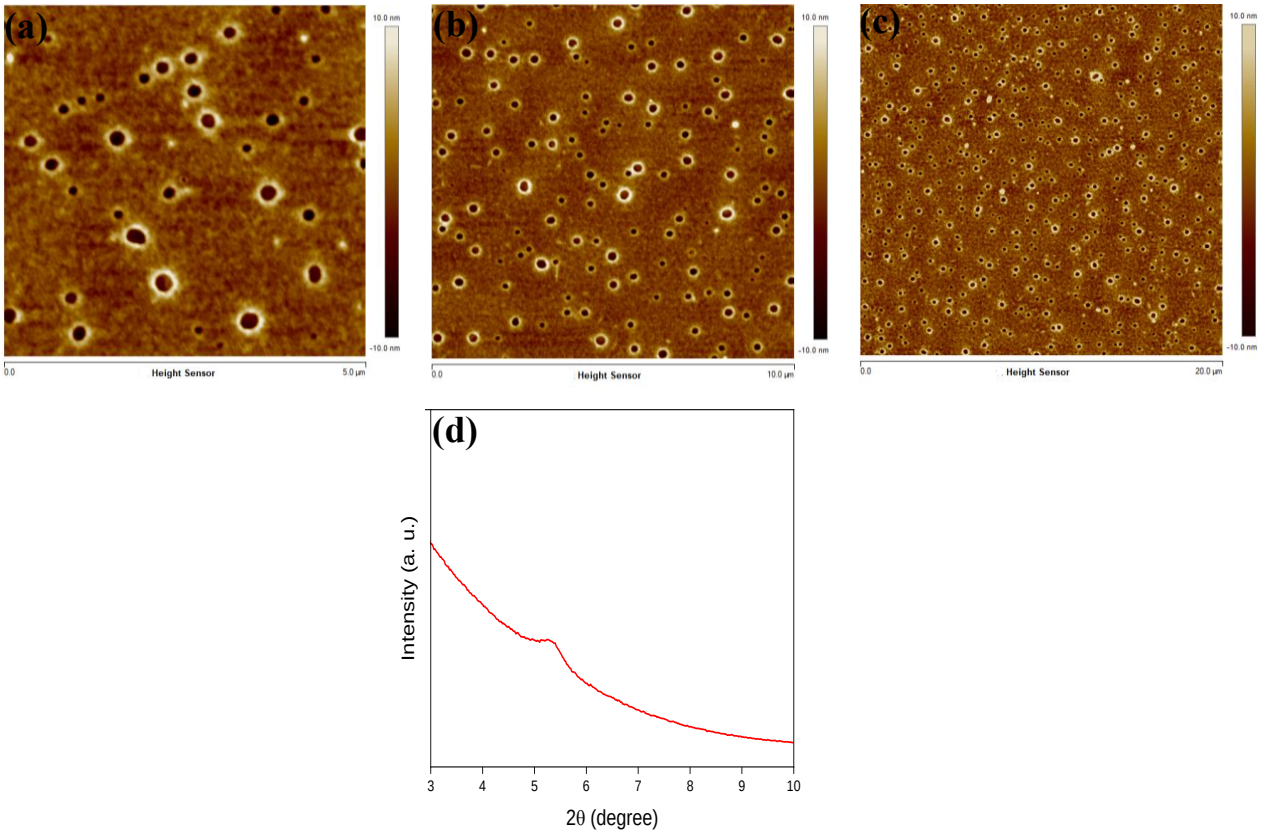


Figure A.1 AFM height images of P3HT films with size: **a)** 5 μm×5 μm, **b)** 10 μm×10 μm, **c)** 20 μm×20 μm and **d)** XRD patterns of the P3HT films.

**Transfer and output characteristics of IGTs at different $V_{gs}$ scan rates**

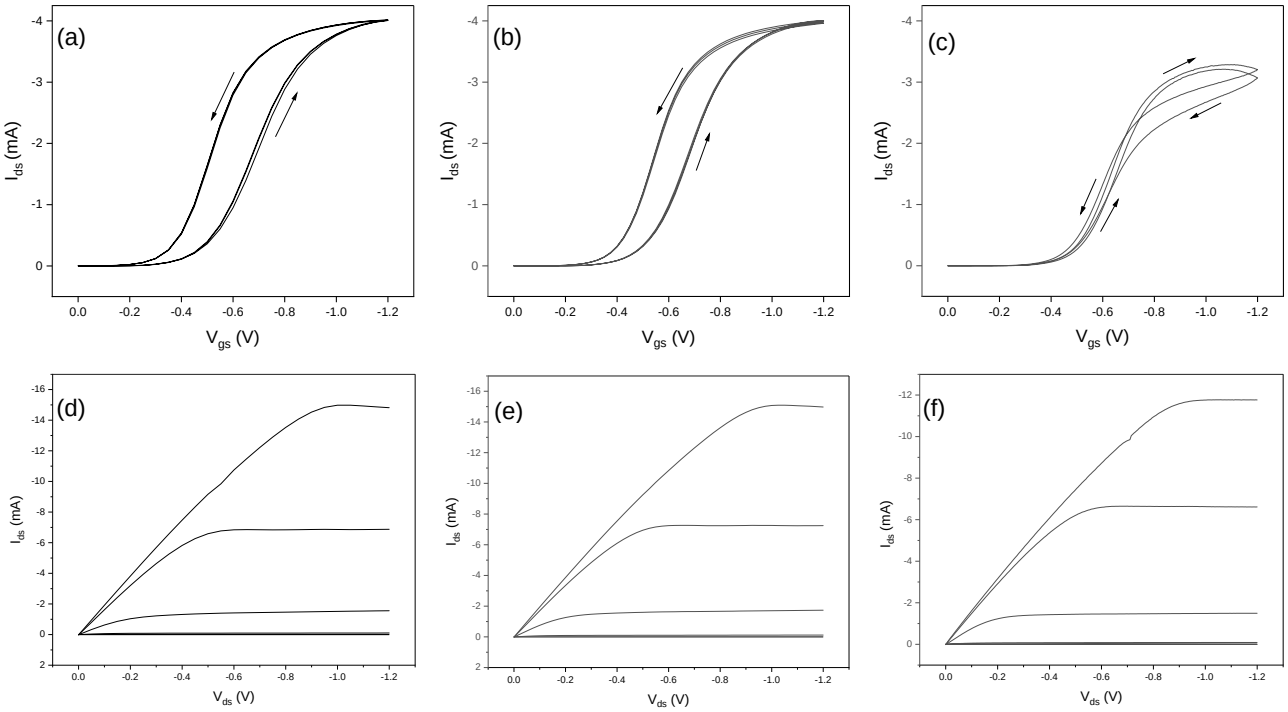


Figure A.2 Transfer characteristics of [EMIM][TFSI]-gated P3HT transistors in the linear regime ($V_{ds}$= -0.2 V (3 cycles)) at $V_{gs}$ scan rates of: a) 50 $mVs^{-1}$, b) 25 $mVs^{-1}$ and c) 5 $mVs^{-1}$. Output characteristics with $V_{gs}$= 0, -0.2, -0.4, -0.6, -0.8, -1 V with $V_{ds}$ scan rates of: d) 50 $mVs^{-1}$, e) 25 $mVs^{-1}$, f) 5 $mVs^{-1}$.

We calculated the charge carrier density ($\rho$, $cm^2$) and mobility (m, $cm^2V^{-1}s^{-1}$) in our P3HT channels from the transfer characteristics with $V_{gs}$ sweeping rates of 5, 25, 50, and 100 $mVs^{-1}$ and $V_{ds}$ = -0.2 V (Table A1).

We obtained the charge carrier density from the equation: $\rho = \frac{Q}{eA} = \frac{\int I_g dV_{gs}}{eAr_v}$, where Q represents the amount of charge accumulated during the forward scan in the transfer curve (resulting from the integration of $I_{gs}$ with $V_{gs}$), e is the elementary charge, A is the interfaced area of the P3HT film, and the ionic media (4 mm×9 mm), and $r_v$ is the scan rate of $V_{gs}$. [230]

The charge carrier mobility, $\mu$, is obtained by $\mu = \frac{L}{W}\frac{I_{ds}}{QV_{ds}}$. [136]

The ON/OFF ratio, calculated from the transfer curves, is the ratio between $I_{ds}$ in the ON state and $I_{ds}$ in the OFF state ($I_{on}/I_{off}$), calculated for a fixed $V_{gs}$. The threshold voltage, $V_{th}$, was calculated using a linear extrapolation of the $I_{ds}$ - $V_{gs}$ curve, in the linear regime. [231]

Table A.1 The values of threshold voltage and ON/OFF ratios of [EMIM][TFSI]-gated P3HT transistors ($V_{ds}$= -0.2 V) at different $V_{gs}$ scan rates:100, 50, 25, and 5 $mVs^{-1}$.

| $V_{gs}$ scan rate ($mVs^{-1}$) | ON/OFF ratios | Threshold voltage (V) | Mobility ($cm^2V^{-1}s^{-1}$) | Charge carrier density ($cm^{-2}$) |
|---|---|---|---|---|
| 100 | $1.7\times10^3$ | -0.47 ± 0.03 | 0.26 ± 0.08 | $1.3\times10^{15} \pm 0.5\times10^{15}$ |
| 50 | $2.6\times10^3$ | -0.46 ± 0.03 | 0.19 ± 0.06 | $1.7\times10^{15} \pm 0.5\times10^{15}$ |
| 25 | $3.1\times10^3$ | -0.45 ± 0.03 | 0.14 ± 0.04 | $2.1\times10^{15} \pm 0.5\times10^{15}$ |
| 5 | $5.8\times10^4$ | -0.44 ± 0.03 | 0.06 ± 0.01 | $5.7\times10^{15} \pm 0.8\times10^{15}$ |

**Importance of the $V_{gs}$ sampling time on the measurement of the response time**

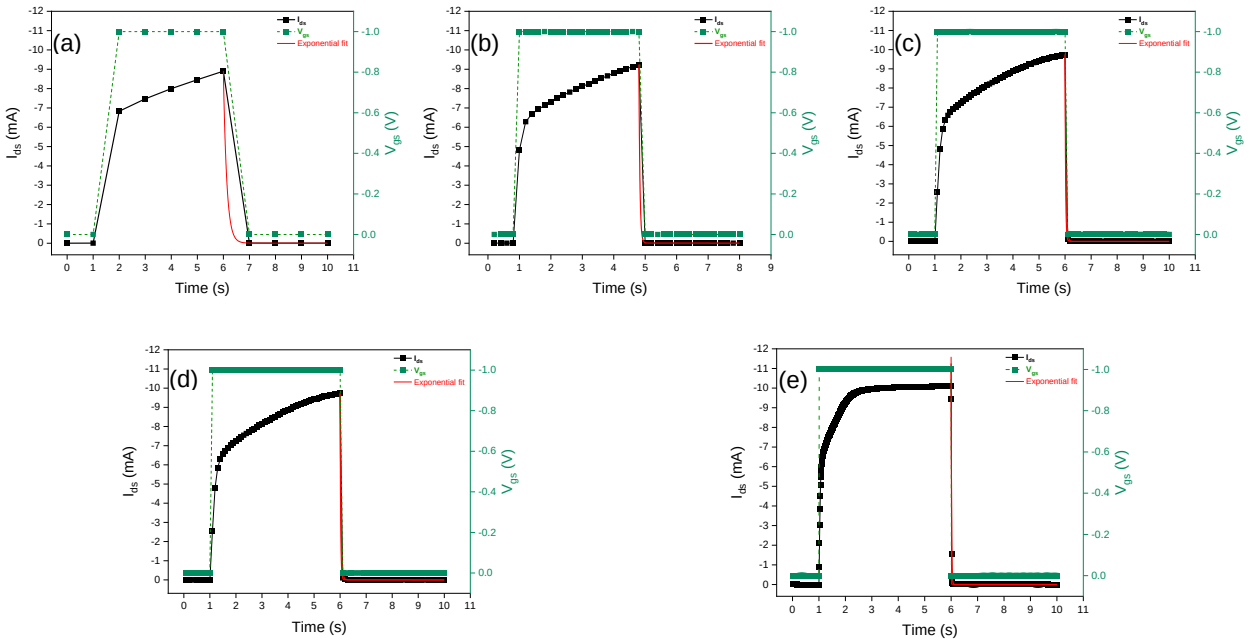


Figure A.3 Transient Ids characteristics of [EMIM][TFSI]-gated P3HT transistors at different Vgs. pulse sampling times: a) 1s, b) 250 ms, c) 100 ms, d) 50 ms, e) 10 ms in response to a single Vgs = -1 V pulse, with Vds=-0.8 V; the duration of the Vgs. pulse is 5 s.

**Fitting parameters for exponential fitting curves**

R-square, also known as the coefficient of determination, measures a model's goodness of fit. The closer the fit is to the data points, the closer R-square will be to the value of 1.

We report fitting parameters for figures 4.3-4.5 in the tables below.

Table A.2 R-square parameter values related to exponential fits used to estimate the response time of different numbers of $V_{gs}$ pulses.

| Number of $V_{gs}$ pulses | 5 pulses | 10 pulses | 25 pulses |
|---|---|---|---|
| R-square | 0.92 | 0.91 | 0.91 |

Table A.3 R-square parameter values related to exponential fits used to estimate the response time of different duration time of pulse.

| Duration time of $V_{gs}$ pulse | 10 ms | 100 ms | 500 ms | 1 s | 5 s | 9 s |
|---|---|---|---|---|---|---|
| R-square | 0.99 | 0.94 | 0.92 | 0.91 | 0.92 | 0.93 |

Table A.4 R-square parameter values related to exponential fits used to estimate the response time of different frequencies of $V_{gs}$ pulses.

| Frequency of $V_{gs}$ pulses | 1 Hz | 5 Hz | 10 Hz |
|---|---|---|---|
| R-square | 0.92 | 0.94 | 0.96 |

Table A.5 R-square parameter related to exponential fits used to estimate the response time of different $V_{gs}$ pulse sampling times.

| $V_{gs}$ pulse sampling times | 10 ms | 25 ms | 50 ms | 100 ms | 250 ms | 500 ms | 1 s |
|---|---|---|---|---|---|---|---|
| R-square ($V_{ds}$=-0.6) | 0.95 | 0.94 | 0.99 | 0.99 | 1 | 1 | 1 |
| R-square ($V_{ds}$=-0.8) | 0.94 | 0.96 | 0.98 | 0.99 | 1 | 1 | 1 |

All R-square parameters are close to 1 and it shows a good fit between the exponential model and the associated decay curves.

# APPENDIX B SUPPORTING INFORMATION ARTICLE 2

## EXPLORING RESPONSE TIME AND SYNAPTIC PLASTICITY IN P3HT ION-GATED TRANSISTORS FOR NEUROMORPHIC COMPUTING: IMPACT OF P3HT MOLECULAR WEIGHT AND FILM THICKNESS

Ramin Karimi Azari,*[a] Zhaojing Gao[a], Alexandre Carrière[a] and Clara Santato

Table B.1 Figures of merit for different MWs [EMIM][TFSI]-gated P3HT transistors at different $V_{gs}$ scan rates (100, 50, and 25 m V $s^{-1}$*).*

| MW | $V_{gs}$ scan rate ($mV\ s^{-1}$) | ON/OFF | $V_{th}$ (V) | Mobility ($cm^2\ V^{-1}\ s^{-1}$) | Charge carrier density ($cm^{-2}$) |
|---|---|---|---|---|---|
| Low | 25 | $(0.8 \pm 1.6) \times 10^3$ | -0.32 ± 0.03 | 0.20 ± 0.03 | $(1.6 \pm 0.2) \times 10^{15}$ |
| | 50 | $(2.1 \pm 0.1) \times 10^3$ | -0.34 ± 0.03 | 0.26 ± 0.09 | $(1.2 \pm 0.1) \times 10^{15}$ |
| | 100 | $(1.6 \pm 0.2) \times 10^3$ | -0.34 ± 0.05 | 0.33 ± 0.02 | $(0.9 \pm 0.3) \times 10^{15}$ |
| Intermediate | 25 | $(2.1 \pm 0.7) \times 10^3$ | -0.44 ± 0.02 | 0.16 ± 0.02 | $(2.0 \pm 0.8) \times 10^{15}$ |
| | 50 | $(3.0 \pm 0.5) \times 10^3$ | -0.44 ± 0.04 | 0.19 ± 0.05 | $(1.6 \pm 0.5) \times 10^{15}$ |
| | 100 | $(2.0 \pm 0.3) \times 10^3$ | -0.44 ± 0.01 | 0.25 ± 0.04 | $(1.2 \pm 0.2) \times 10^{15}$ |
| High | 25 | $(3.5 \pm 0.5) \times 10^3$ | -0.45 ± 0.2 | 0.13 ± 0.09 | $(2.3 \pm 0.09) \times 10^{15}$ |
| | 50 | $(3.0 \pm 0.1) \times 10^3$ | -0.45 ± 0.01 | 0.16 ± 0.06 | $(1.9 \pm 0.3) \times 10^{15}$ |
| | 100 | $(1.9 \pm 0.3) \times 10^3$ | -0.45 ± 0.01 | 0.22 ± 0.01 | $(1.4 \pm 0.2) \times 10^{15}$ |

The threshold voltage, $V_{th}$, was determined by linearly extrapolating the $I_{ds}$-$V_{gs}$ curve within the linear regime. The ON/OFF ratio, derived from the transfer curves, represents the ratio of $I_{ds}$ at a constant $V_{gs}$ in the ON and OFF states ($I_{on}/I_{off}$). [69]

We calculated the charge carrier density (ρ, $cm^2$), and then the mobility (μ, $cm^2V^{-1}s^{-1}$), from the transfer characteristics with $V_{gs}$ sweeping rates of 25, 50, and 100 $mVs^{-1}$ at $V_{ds}$ = -0.2 V (Table B.2). [140]

The charge carrier density was calculated from the equation: $\rho = \frac{Q}{eA} = \frac{\int I_g dV_{gs}}{eAr_v}$, Q signifies the quantity of charge accumulated during the forward scan in the transfer curve (derived from the integration of $I_{gs}$ with $V_{gs}$), *A* is the area of the P3HT film interfaced with the ionic liquid (4 mm×9 mm), *e* is the elementary charge, and $r_v$ is the scan rate of $V_{gs}$. [136, 232]

The charge carrier mobility, and $\mu$, was obtained by $\mu = \frac{L}{W}\frac{I_{ds}}{QV_{ds}}$. [231]

Table B.2 Figures of merit for different spin coating speeds [EMIM][TFSI]-gated P3HT transistors at different $V_{gs}$ scan rates (100, 50, and 25 m V $s^{-1}$*).*

| Spin coating speed (rpm) | $V_{gs}$ scan rate (m V $s^{-1}$) | ON/OFF | $V_{th}$ (V) | Mobility ($cm^2$ $V^{-1}$ $s^{-1}$) | Charge carrier density ($cm^{-2}$) |
|---|---|---|---|---|---|
| 500 | 25 | (3.1 ± 1.6) × $10^3$ | -0.43 ± 0.02 | 0.10 ± 0.03 | (3.4 ± 1.2) × $10^{15}$ |
| | 50 | (2.0 ± 1.1) × $10^3$ | -0.44 ± 0.02 | 0.12 ± 0.04 | (2.8 ± 0.9) × $10^{15}$ |
| | 100 | (1.2 ± 0.8) × $10^3$ | -0.45 ± 0.03 | 0.16 ± 0.04 | (2.1 ± 0.5) × $10^{15}$ |
| 1000 | 25 | (1.5 ± 0.3) × $10^3$ | -0.48 ± 0.06 | 0.25 ± 0.07 | (1.9 ± 0.5) × $10^{15}$ |
| | 50 | (2.6 ± 1.5) × $10^3$ | -0.49 ± 0.06 | 0.33 ± 0.08 | (1.4 ± 0.3) × $10^{15}$ |
| | 100 | (2.2 ± 1.2) × $10^3$ | -0.50 ± 0.07 | 0.52 ± 0.08 | (8.2 ± 0.6) × $10^{14}$ |

| | | | | | |
|---|---|---|---|---|---|
| 2000 | 25 | $(2.0 \pm 1.0) \times 10^3$ | -0.46 ± 0.02 | 0.20 ± 0.06 | $(1.5 \pm 0.1) \times 10^{15}$ |
| | 50 | $(2.7 \pm 0.3) \times 10^3$ | -0.47 ± 0.02 | 0.26 ± 0.07 | $(1.2 \pm 0.1) \times 10^{15}$ |
| | 100 | $(1.7 \pm 0.2) \times 10^3$ | -0.45 ± 0.03 | 0.34 ± 0.10 | $(8.1 \pm 0.7) \times 10^{14}$ |
| 4000 | 25 | $(1.0 \pm 1.0) \times 10^4$ | -0.44 ± 0.03 | 0.34 ± 0.11 | $(8.2 \pm 0.8) \times 10^{14}$ |
| | 50 | $(8.6 \pm 6.2) \times 10^3$ | -0.44 ± 0.02 | 0.45 ± 0.11 | $(6.3 \pm 0.6) \times 10^{14}$ |
| | 100 | $(5.1 \pm 3.0) \times 10^3$ | -0.44 ± 0.02 | 0.61 ± 0.17 | $(4.6 \pm 0.3) \times 10^{14}$ |

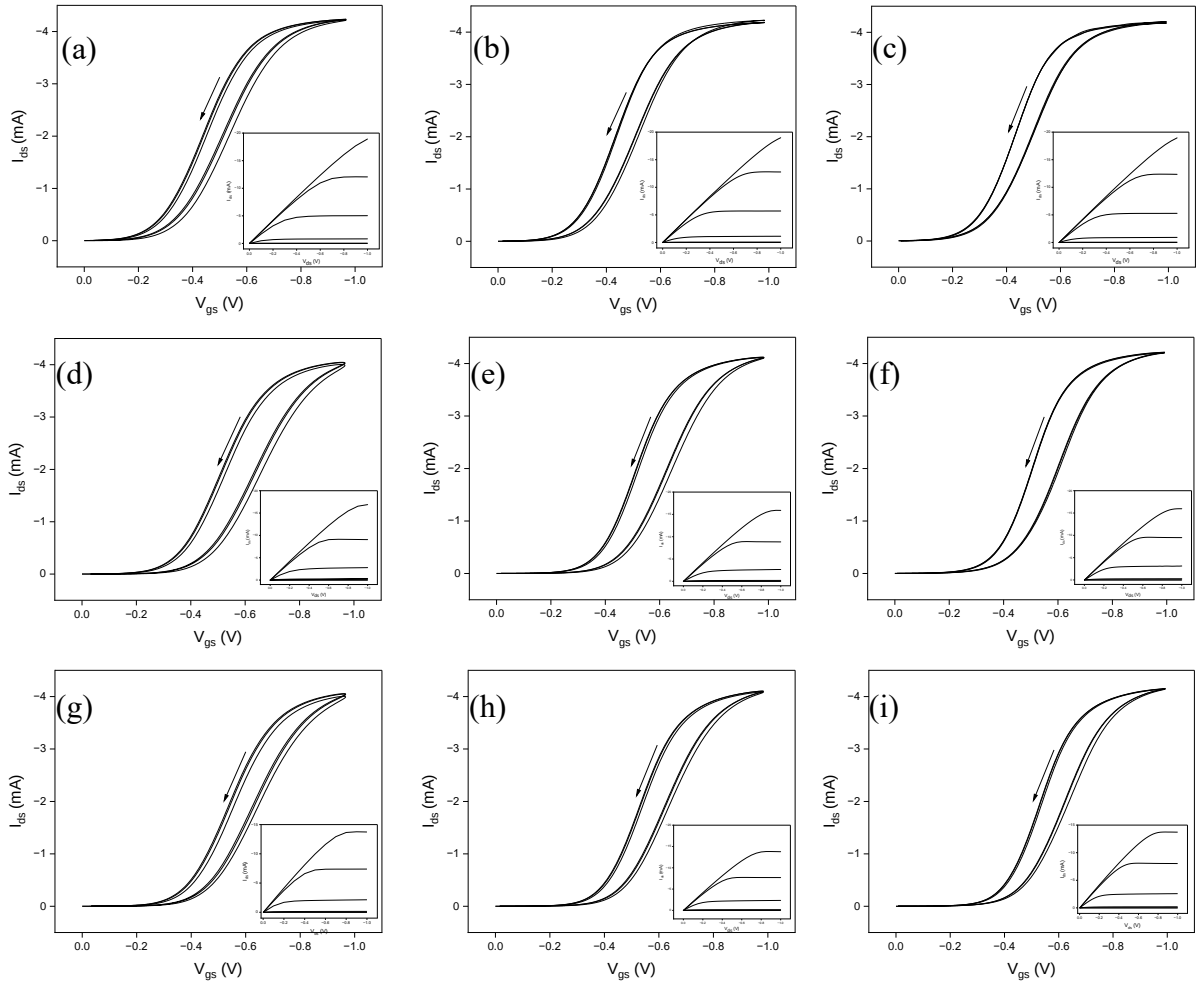


Figure B.1 Transfer characteristics in the linear regime ($V_{ds}$ = -0.2 V, (3 cycles)) at $V_{gs}$ scan rate 100, 50, and 25 m V $s^{-1}$ (inset: output characteristic with $V_{gs}$ = 0, -0.2, -0.4, -0.6, -0.8, -1 V and $V_{ds}$ 100, 50, and 25 m V $s^{-1}$ scan rate) for [EMIM][TFSI]-gated transistors based on a, b, c) low MW d, e, f) intermediate MW g, h, i) high MW P3HT.

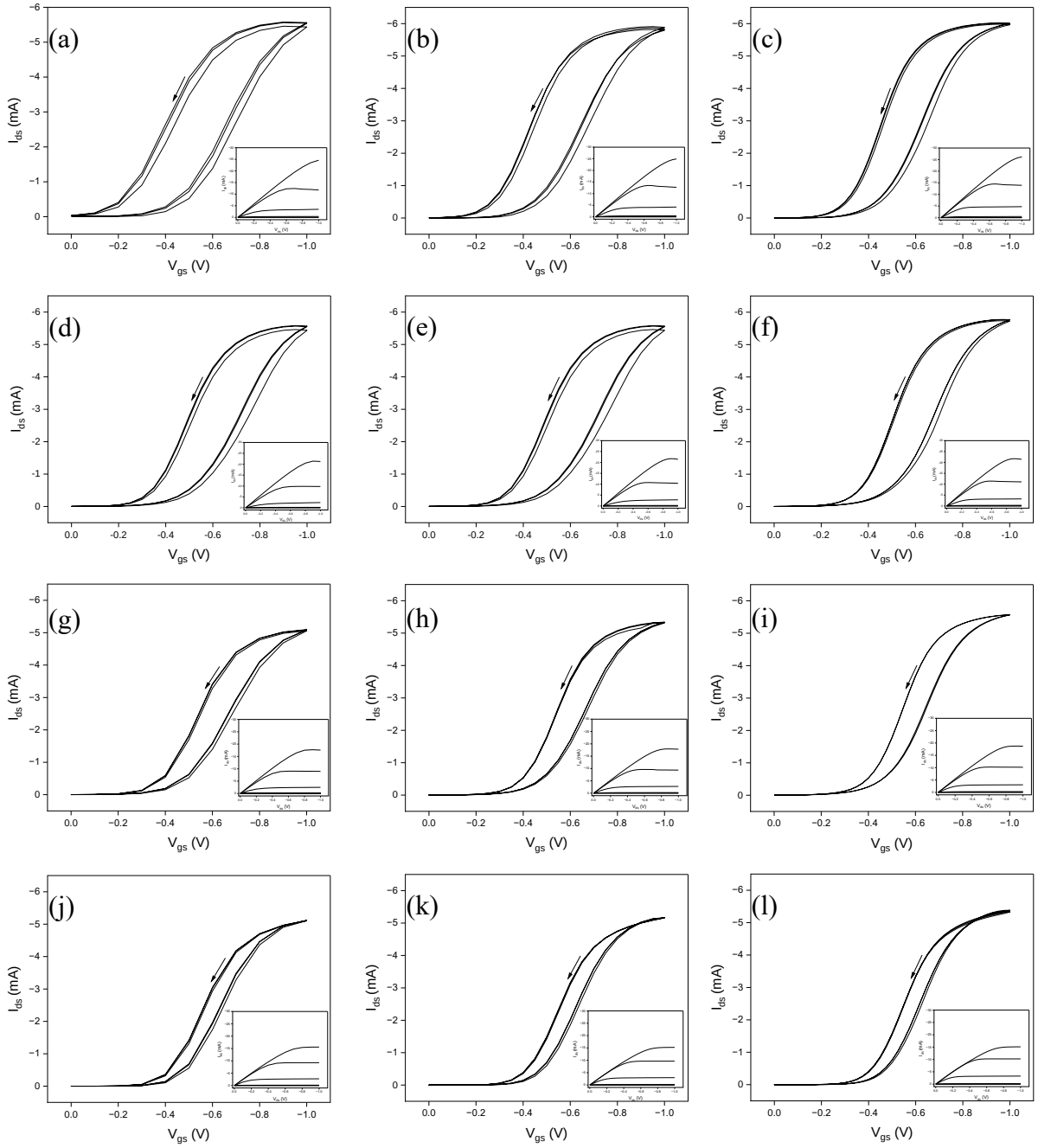


Figure B.2 Transfer characteristics in the linear regime ($V_{ds}$ = -0.2 V, (3 cycles)) at $V_{gs}$ scan rate 100, 50, and 25 m V $s^{-1}$ (inset: output characteristic with $V_{gs}$ = 0, -0.2, -0.4, -0.6, -0.8, -1 V and $V_{ds}$ 100, 50, and 25 m V $s^{-1}$ scan rate) for [EMIM][TFSI]-gated transistors P3HT transistors prepared with spin coating speed a, b, c) 500 rpm d, e, f) 1000 rpm g, h, i) 2000 rpm j, k, l) 4000 rpm.

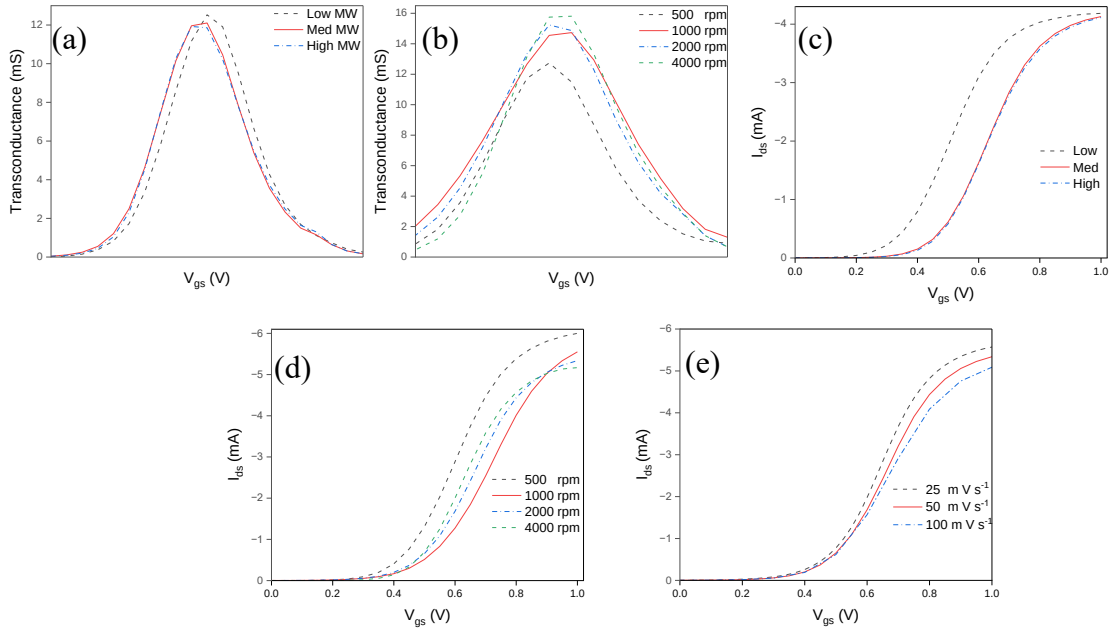


Figure B.3 Transconductance curve for [EMIM][TFSI]-gated transistors based on P3HT deposited at a) high MW (blue line), intermediate MW (red line), and low MW (black line) at 1000 rpm during 30 s b) spin coating rate 500 rpm (black line), 1000 rpm, (red line), 2000 rpm (blue line), and 4000 rpm (green line), on 30 seconds with intermediate MW. Ids level ($V_{ds}$ = -0.2 V) at $V_{gs}$ 50 m V $s^{-1}$ scan rate for [EMIM][TFSI]-gated transistors based on P3HT deposited at c) high MW (blue line), intermediate MW (red line), and low MW (black line ) d) spin coating rate 500 rpm (black line), 1000 rpm (red line), 2000 rpm (blue line), and 4000 rpm (green line), on 30 seconds with intermediate MW e) intermediate MW and 1000 rpm at $V_{gs}$ 25 (black line), 50 (red line), and 100 (blue line) m V $s^{-1}$ scan rate.

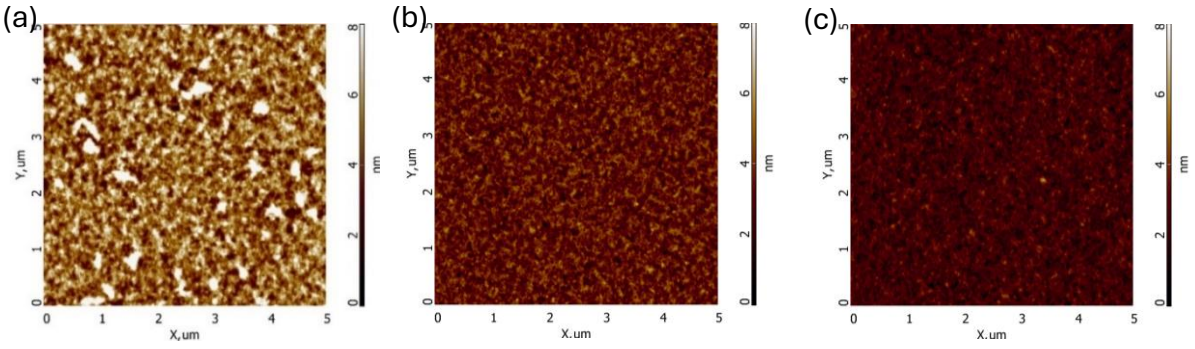


Figure B.4 AFM height images of (a) low MW, (b) intermediate MW and (c) high MW with a same height scale of 0 to 8 nm.

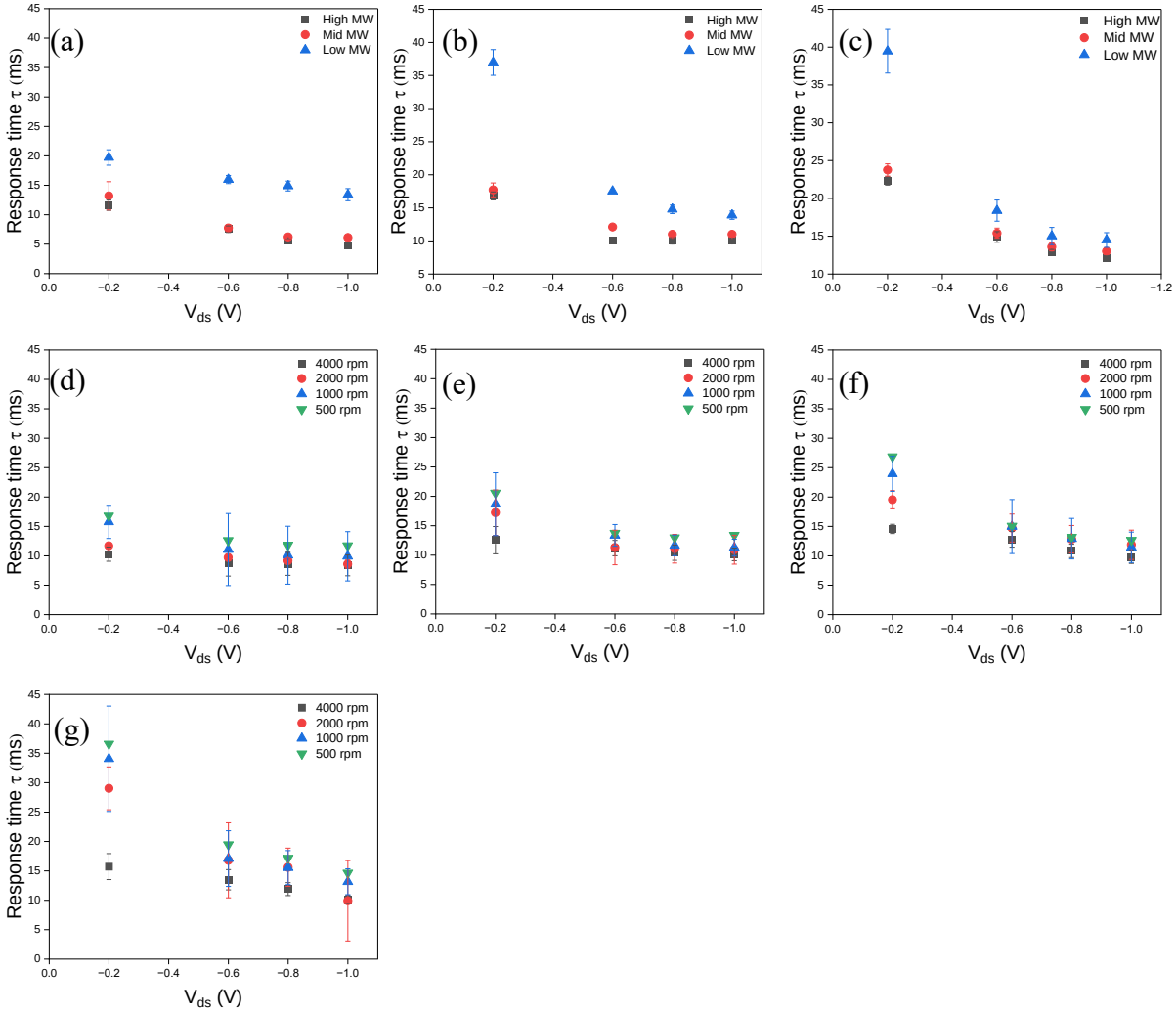


Figure B.5 Transient response of an [EMIM] [TFSI]-gated P3HT transistor with high, intermediate, and low MW for $V_{gs}$ = a) -0.5 V, b) -0.8 V, and c) -1 V at different $V_{ds}$. The duration time of the $V_{gs}$ bias is 200 ms. Transient response of [EMIM][TFSI]-gated P3HT transistors prepared with spin coating rate 500, 1000, 2000, *and* 4000 rpm, on 30 seconds with intermediate MW with $V_{gs}$ = d) -0.5 V, e) -0.8 V, f) -1 V, and g) -1.2 V at different $V_{ds}$. The duration of the $V_{gs}$ bias is 200 ms.